THE UNIVERSITY OF CHICAGO

A SEARCH FOR TRANSIENT SOURCES IN THE FIRST 100 DEG^2 OF SPTPOL DATA

A DISSERTATION SUBMITTED TO
THE FACULTY OF THE DIVISION OF THE PHYSICAL SCIENCES
IN CANDIDACY FOR THE DEGREE OF
DOCTOR OF PHILOSOPHY

DEPARTMENT OF PHYSICS

BY
TYLER NATOLI

CHICAGO, ILLINOIS
DECEMBER 2015

The important thing is to not stop questioning.

- Albert Einstein

TABLE OF CONTENTS

LIST OF FIGURES

LIST OF TABLES

ACKNOWLEDGMENTS

I would like to thank my advisor John Carlstrom for creating an incredible environment to learn about the workings of the universe. John allowed me to focus on what I deemed the most interesting projects and always encouraged me to ask questions. The South Pole Telescope collaboration can clearly be seen as an extension of the same research principles John creates at Chicago, and was truly a great group to work in.

During my first few years of studies, Brad Benson and Clarence Chang transferred a great deal of knowledge to me and I am thankful to them for showing me such great patience. I thank Nathan Whitehorn and Jason Gallicchio who both worked with me on my final analysis project and took extra time and effort to help me fully comprehend topics new to me. I would like to give a special thanks to Abby Crites and Kyle Story. Abby taught me cryogenics during our years hunched over cryostats and never grew annoyed with my constant hyperbole or unparalleled estimation abilities. Throughout graduate school Kyle and I have worked closely together, he has given me so much assistance and direction during this time that I am unsure I would have graduated without his company.

Lastly, I would like to thank my mother and father, Jean and Chuck Natoli for their boundless support. They deserve much more credit than I like to admit for creating my inquisitive personality and shaping the person I have become.

ABSTRACT

We will present the results from a systematic transient source search over a 100 $\deg^2$ field of millimeter wavelength data taken with the SPTpol camera on the South Pole Telescope (SPT). The SPTpol instrument was installed on the SPT in the Austral summer of 2011/2012 and features 1,536 polarization sensitive detectors and observes at 150 GHz with an angular resolution of 1.1 arcminutes. The transient data set presented here includes 9 months of SPTpol observations over the same 100 $\deg^2$ patch of sky that we break down into 36 hour observing blocks, each obtaining an average depth of 7.4 mJy at 150 GHz. The technology developed for SPTpol detectors is described here along with the associated technology necessary to operate the detectors. We present the specifics of producing millimeter wavelength maps from raw detector timestreams.We describe the specific analysis and results of searching for transient sources with timescales of days to weeks in the first 100 $\deg^2$ of data taken by the SPTpol camera. Using the search results we place upper limits on the number of millimeter transient sources as a function of the transient duration above a flux of 20 mJy.

CHAPTER 1

INTRODUCTION

In this thesis, we describe a transient analysis of 100 deg^2 of SPTpol data, the first transient analysis performed on data taken with the SPT. The SPTpol[1]camera was designed to make observation of the cosmic microwave background (CMB) with the goal of informing and constraining cosmological parameters. Millimeter wavelength polarization data from the SPTpol camera has already been used for several CMB publications [23][11][28]. In addition to CMB science the SPTpol data is capable of adding new observation bands to time-domain astronomy. By exploring a new parameter space of time-domain astronomy the SPTpol camera will search for new populations of transient sources and contribute to the understanding of current transient sources.

The remaining sections of this chapter describe the role of time-domain astronomy and the details of one potential millimetter wavelength transient population, gamma-ray bursts. In chapter 2, the SPTpol camera is described along with related technologies. In chapter 3, the process of creating map realizations from timestreams and quality assurance cuts are discussed. In chapter 4, we present the specific map processing and transient search algorithm performed for this survey and give search results. In chapter 5 limits on transients within the 100 deg^2 field are discussed and the associated implications for gamma-ray burst afterglow emission in the millimeter band.

1.1 Time-Domain Astronomy and SPTpol

Time-domain astronomy is a rapidly growing field with large regions of untouched discovery space. The 2010 decadal survey in astronomy cited the potential of time-domain astronomy across the entire electromagnetic spectrum to "lead to significant scientific discoveries and

1. SPTpol is not officially an acronym, despite the combination of capital and lowercase letters.

new insights" [34]. Many of the transient sources currently studied represent the most distant and energetic populations in the universe. Studying these populations will push our understanding of physics to the limits of high energy and special relativity. By looking for transients in the millimeter sky the SPTpol camera can help constrain the most energetic events in the universe and hunt for new populations of transient phenomena.

As we will describe in Section 3.1, the SPTpol camera mapped the same 100 $\deg^2$ patch of sky once an hour during observing for the first year of operation. Continuous observations of a single patch of sky lead to a deep final map, but also produce a transient survey data set with a high cadence. The work presented here, using data from the first 100 $\deg^2$ of SPTpol data, is the transient search performed over data taken with the SPT.

The transient data set presented here includes 100 $\deg^2$ map coadds from every $\sim$36 hours with an average depth at 150 GHz of 7.4 mJy and a resolution of 1.1 arcminute. As we will discuss in Chapter 4, the transient search over the SPTpol 100 $\deg^2$ field focuses on identifying transients with timescales of days to weeks. Although any bright transients with the target timescales can be detected, the target transient population is gamma-ray burst afterglows.

1.2 Gamma-Ray Bursts

Gamma-ray bursts (GRBs) are the brightest, and amongst the most energetic, events in the universe. The first GRB discovery was published in 1973 using gamma-ray data taken by United States satellites intended for nuclear bomb detection [29]. GRBs have been an active area of research since their discovery and, with the *Swift* and *Fermi* satellites, are the focus of dedicated satellite missions [15] [32].

The exact progenitor of GRBs are still unknown, but there are developed models to explain the phenomena. The only known way to produce an event as energetic as a GRB is through gravitational collapse. Driven by observations, GRBs are divided into two separate

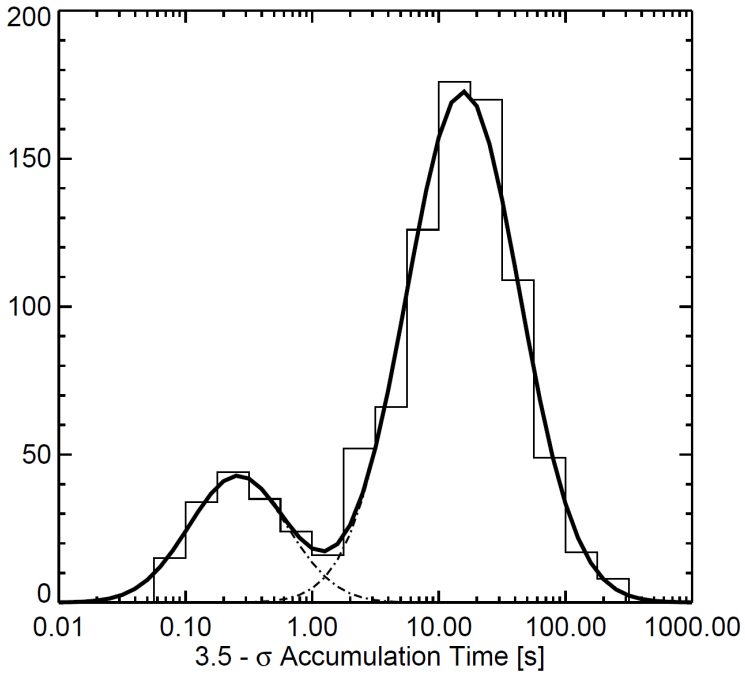

Figure 1.1: From [21]. Gamma-ray burst duration times as measured by the Gamma-ray Burst Monitor (GBM) on the *Fermi* space satellite for events with signal-to-noise above 3.5. A distinction between short-GRBs and long-GRBs is shown with a dividing time of 1.27 seconds.

populations, short and long duration GRBs, with separate proposed progenitors for each population (see Figure 1.1 for the population time distributions). The observed association between long duration GRBs, supernova, and galaxies with a high rate of star formation has lead to the theory that long duration GRBs are preceded by the death of massive stars [26]. Neutron star mergers with a black hole or another neutron star are the preferred progenitors to explain the timescales down to milliseconds observed with short duration GRBs [3]. The gravitational collapse leading to both long and short duration GRBs suggest the final state of a GRB is a stellar mass black hole or possibly a magnetar.

GRBs are named for the intense flash of light, peaked in the gamma-ray band, they emit on timescales of 0.1 to 1,000 seconds. The bright flash, or "burst", releases $\sim 10^{51}$ ergs of energy to create a signal that is a million times more luminous than supernovae[2][16]. The extreme luminosity of this event allow GRBs to be seen at redshifts greater than 8 and to be counted as the most distant objects observed in the universe, Figure 1.2 [47].

The GRB flash emission is a highly beamed relativistic jet with an opening angle of $\sim$5 degrees [24]. According to proposed models, the jet is fuelled by matter falling into the black hole left over from the merger or collapse that gets ejected along the rotation axes of the black hole. The infalling material is likely to create strong magnetic fields that can pump rotational energy from the black hole to the jet [15].

After the initial burst of gamma-rays a longer lasting "afterglow" signal is observed at optical, radio, and X-ray frequencies as the jet angle widens and creates shock waves as it interacts with the surrounding material. The first GRB afterglow was not detected until 1997 when the pointing of gamma-ray telescopes became good enough to localize GRBs for follow up observations in other bands [10]. The X-ray component of an afterglow occurs only hours after the gamma-ray emission and is observed for most GRBs. Optical and infrared afterglows have been seen for $\sim$50% of GRBs with good pointing. GRBs without optical/infrared

2. Supernovae also release $\sim 10^{51}$ ergs of energy, but do so isotropically. GRBs release energy in a focused jet making them much more luminous along the jet than supernovae.

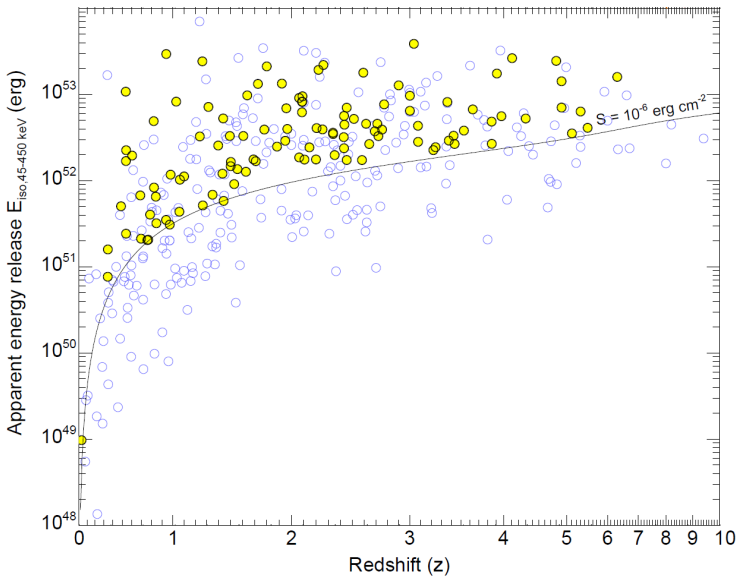

Figure 1.2: From [38]. The apparent isotropic energy ($E_{\rm iso}$) released by GRBs detected by the Burst Alert Telescope (BAT) on *Swift* versus redshift. Beam opening angle uncertainties prevent accurate calculations of the energy released by a GRB so the apparent isotropic energy is reported instead. By multiplying the apparent isotropic energy by the beam area fraction the actual energy released by the GRB can be calculated. Yellow points are part of a particular GRB followup survey (*Swift* SHOALS) but are not intrinsically different than the open blue points. GRBs are amongst the most energetic and distant objects observed in the universe.

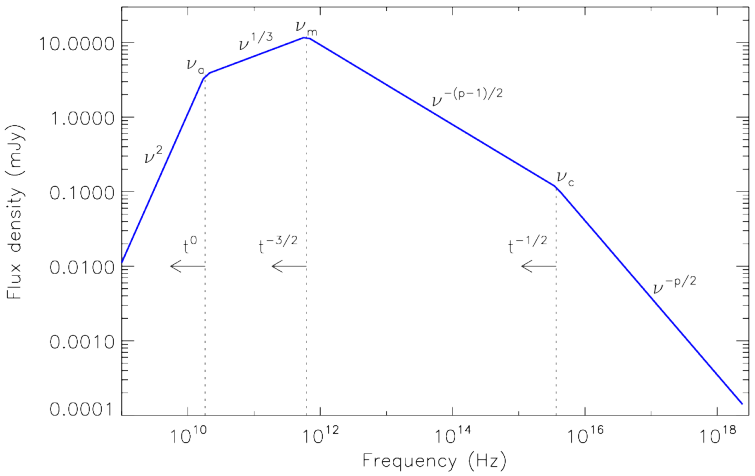

Figure 1.3: From [12]. Expected synchrotron spectrum from a GRB afterglow using the fireball model in the slow-cooling regime. The three break frequencies from low to high correspond to the synchrotron self-absorption frequency, the characteristic synchrotron frequency (the max of the spectrum), and the cooling frequency. The evolution of the spectrum is also indicated with time dependences at the break frequencies.

afterglows are referred to as "dark" GRBs and may represent a new population of GRBs with an inherently fainter (2-3 magnitudes) afterglow luminosity [37] or may be explained by dusty molecular clouds along the line of sight absorbing the optical afterglow light [41]. Radio observations could help differentiate between the two dark GRB models since radio waves are not absorbed by dust the way optical light is. When observed, optical afterglows are typically visible for weeks after a GRB event, but the optical emission from the first X-ray afterglow detected was observed for over 6 months [14]. Radio afterglows have been observed in ∼50% of well-localized GRBs and generally become visible a full day after the gamma-ray emission [39].

Figure 1.3 shows a prediction of synchrotron emission from the relativistic fireball GRB model in the slow-cooling regime. The spectrum is peaked near the SPTpol observation frequencies of 90 and 150 GHz.

Because afterglows are formed as the GRB jet interacts with surrounding material and slows down (less beaming), the viewing angle of an afterglow is larger than the viewing angle

of the prompt gamma-ray emission. The larger viewing angle of GRB afterglows should lead to more afterglows being detected than gamma-ray triggered GRBs. Observed afterglows with no detection of gamma-ray emission are referred to as "orphan afterglows" and can constrain the opening angle of the GRB jet [19]. No orphan afterglow has been observed to date.

Observations of GRB afterglows in the millimeter band can also help differentiate GRB models by measuring the reverse shock. In the relativistic fireball model for GRB there are two shocks that transfer considerable energy to the interstellar medium; a forward shock that propagates into the interstellar medium and a reverse shock that propagates into the GRB shell. Observations of the reverse shock have been made in the optical but if the reverse shock can be observed in the millimeter it can provide a cleaner measurement since the millimeter does not suffer from scintillation and extinction. Below GHz frequencies the reverse shock is thought to be fainter than the forward shock, but at millimeter frequencies the reverse shock can be substantially brighter than the forward shock [33].

The *Fermi* satellite Gamma-ray Burst Monitor (GBM) instrument detects ∼300 unique GRBs a year while surveying 50% of the sky at a time. If an afterglow opening angle at 150 GHz is assumed to be 2 times larger than a GRB opening angle (so a factor of 4 is opening area), there should be ∼6 GRB afterglows in 100 $\deg^2$ of sky every year. By achieving a 7.4 mJy map depth every 36 hours the SPTpol camera would only be able to see the brightest ∼5%-10% radio afterglows observed. Even with the the relatively low expectation of observing 0-1 GRB afterglows, performing a transient search in SPTpol data is an important first step to understanding the GRB afterglows and the transient sky at millimeter wavelengths.

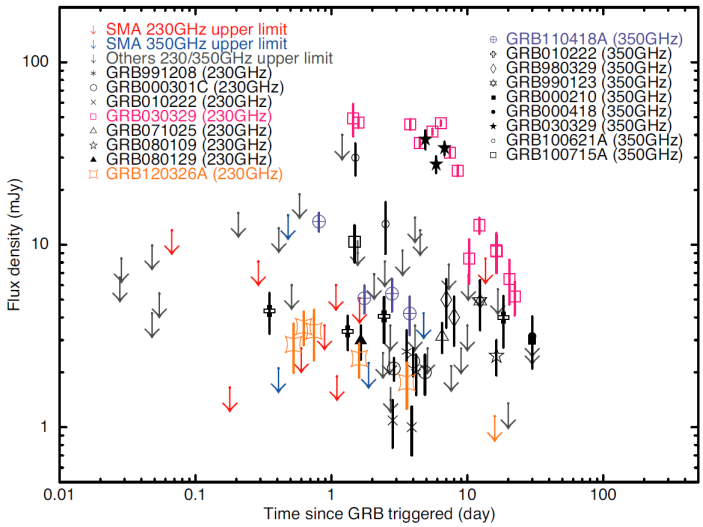

Figure 1.4: From [48]. A comprehensive summary of all detected sub-millimeter GRB afterglows as of March 2015. Downward facing arrows represent upper limits only and all other markers indicate measured flux at either 230 or 350 GHz. For reference the average noise level of a fridge cycle map bundle used in this analysis at 150 GHz is 7.4 mJy and includes maps from 28 hours of observations.

CHAPTER 2

THE INSTRUMENT

2.1 The South Pole Telescope

The South Pole Telescope (SPT, Figure 2.1) achieved first light in February of 2007, and is located at the Amundsen-Scott South Pole Station in Antarctica [8]. The SPT is an offset Gregorian telescope with a ten meter primary reflector and a 1.2 meter secondary reflector that is cooled to 10 K. The field of view of the SPT is one square degree and it achieves a resolution of $\sim$1 arcminute at 150 GHz, see Figure 2.2 and [36] for more information on the secondary optics. The original camera installed on the SPT was the SPT-SZ camera. The SPT-SZ camera has made several new discoveries, including the first discovery of galaxy clusters using the Sunyaev-Zeĺdovich Effect [46]. In 2012, the SPT-SZ camera was replaced by a polarization sensitive camera, SPTpol; we describe the SPTpol camera in Section 2.2.

The South Pole is the best developed site in the world for microwave astronomy, owing to the dry stable atmosphere and high elevation. The median precipitable water vapor in the winter at the South Pole is $\sim$ 0.25 mm [9]. The atmosphere during the six month long night at the South Pole is extremely stable since it does not suffer from daily solar heating [6]. The physical altitude at the South Pole is 2800 meters, but the average pressure altitude in winter is 3300 meters [8]. The unique advantage of being at the geographical South Pole is that the same patch of sky can be observed 24 hours a day for 365 days a year. The remainder of this Chapter discusses the technology of the SPTpol camera as it was used for the measurements presented in this thesis.

2.2 The SPTpol Camera

SPTpol is the second generation camera, and the first polarization sensitive camera to be installed on the SPT. The camera was installed during the Austral summer of 2012 and be-

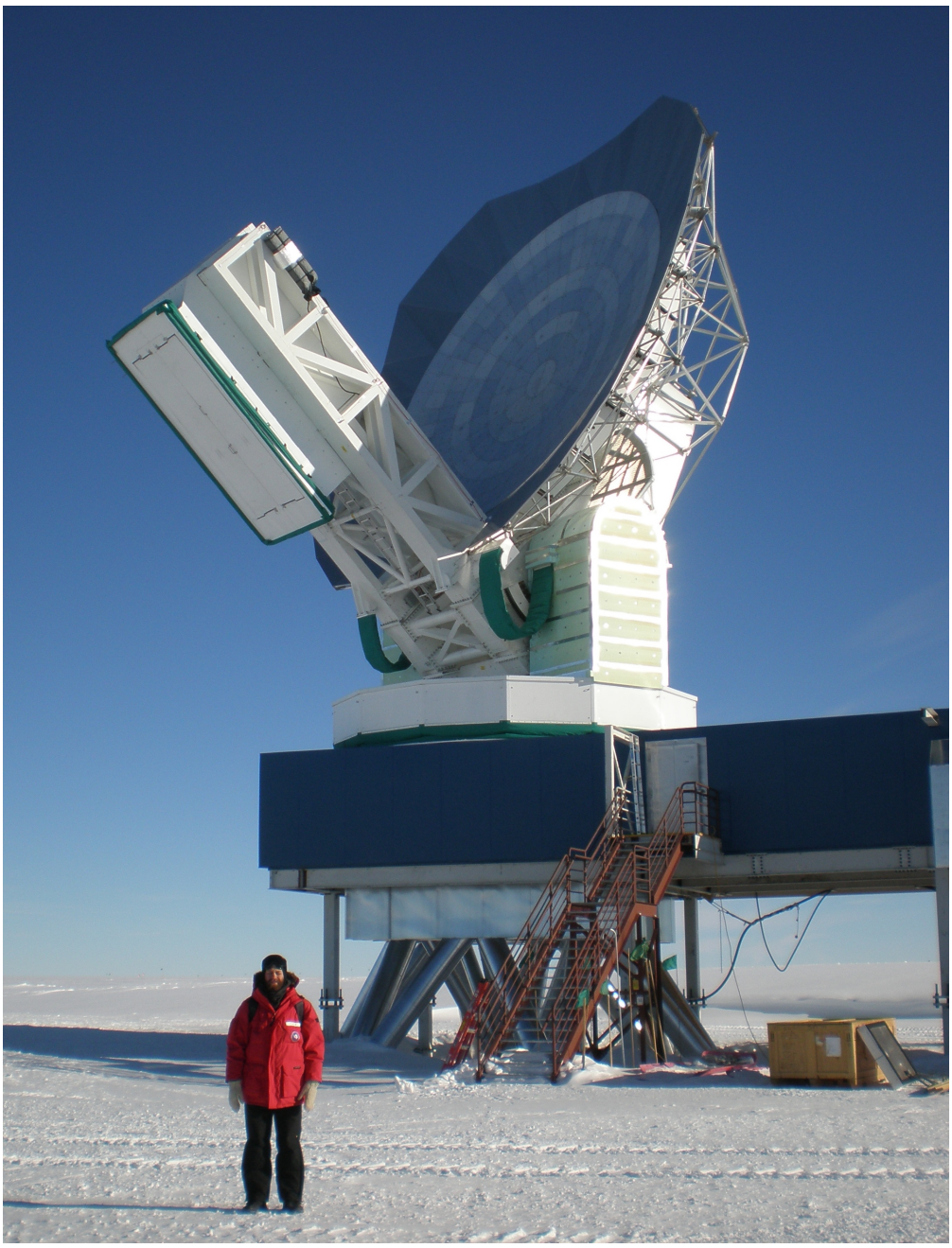

Figure 2.1: The South Pole Telescope in its natural habitat with a graduate student for scale. The primary reflector of the telescope is 10 meters in diameter. The blue building below the telescope is the telescope control room and has a retractable roof on the right. On the underside of the telescope boom two large trap doors can be seen which mate to the control room roof. This mating allows the telescope camera and electronics housed in the boom to be checked and repaired inside without removal. Notice the lack of any features on the horizon around the telescope. The SPT sits on top of the Antarctic Plateau that is made of ice nearly two miles thick.

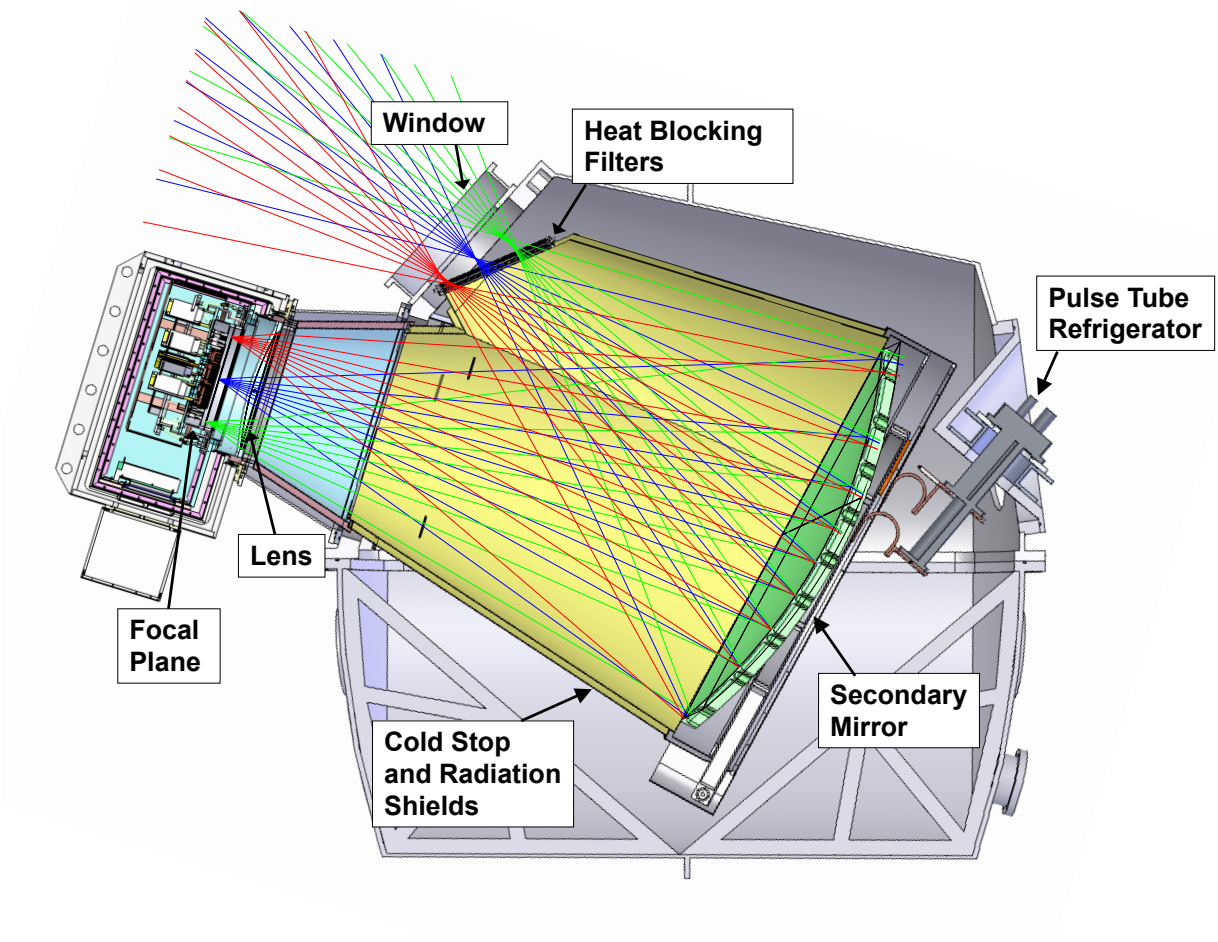

Figure 2.2: From [17]. The South Pole Telescope secondary and receiver cryostats are shown along with a ray tracing of light coming from the primary reflector. The secondary mirror is cooled to 10 K and is surrounded by black millimeter wavelength absorbing foam to act as a stop for the optics.

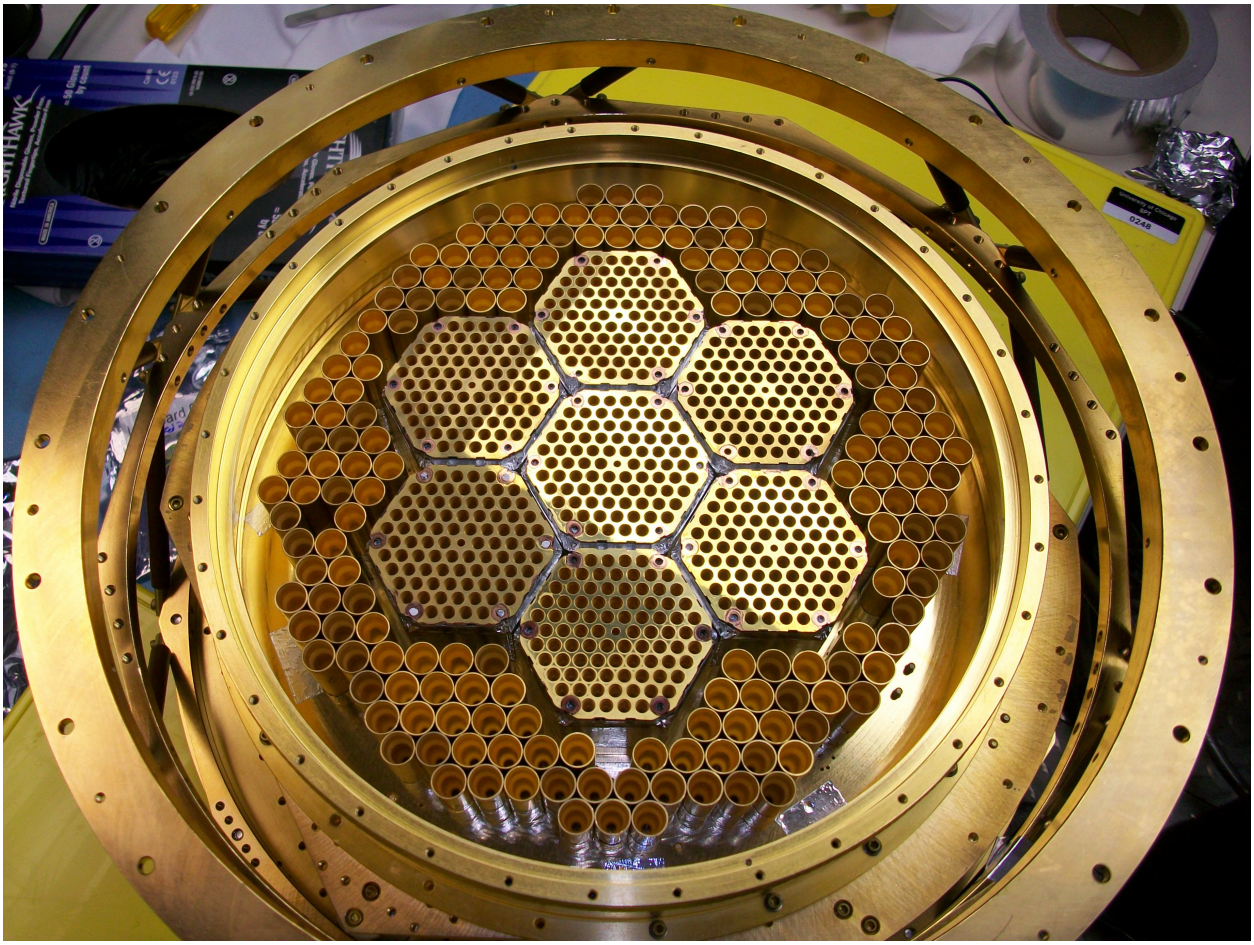

Figure 2.3: The fully assembled SPTpol focal plane just before being installed in the receiver crysotat. The 150 GHz hexagonal modules are in the center of the focal plane and the individually assembled 90 GHz feedhorns around the outside.

gan taking science quality data immediately after installation. The SPTpol camera consists 360 detectors at 90 GHz and 1,176 detectors at 150 GHz for a total of 1536 transition edge sensor bolometers. The detectors are operated at a base temperature of 250 mK and are read out with a digital frequency multiplexed system using Superconducting QUantum Interference Devices (SQUIDs). Details of the bolometer and readout technologies of SPTpol are discussed in the remaining parts of this section.

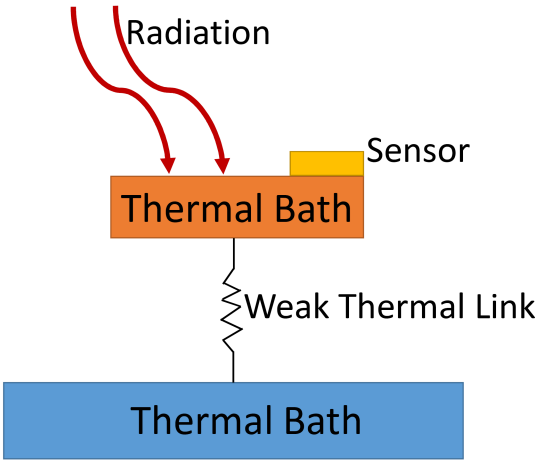

Figure 2.4: A simple cartoon of a bolometer is shown. Radiation incident on the absorber will cause the absorber temperature to increase in the absence of a TES. When a TES is operated in the strong negative electro-thermal regime slight fluctuations in absorber temperature are countered with changes in the current going through the TES. This current change causes the heating power of the TES to compensate for the change in absorber temperature, thus maintaining a constant island temperature.

2.2.1 Transition Edge Sensor Bolometers

A bolometer consists of a radiation absorber that is weakly thermally connected to a heat bath, Figure 2.4. Incident radiation causes the absorber temperature to increase which is detected by a thermal sensor [31]. For SPTpol we use transition edge sensor (TES) bolometers, a TES operates in the transition region between a normal electrical resistance and a superconducting resistance of zero. Figure 2.5 shows the superconducting-normal transition curve for a TES detector. When operating a TES in the transition region small temperature fluctuations in the absorber cause large resistance changes in the sensor. The shape and width of the transition region can be engineered by adjusting the TES geometry and adding superconducting features on top of the TES [18]. If a constant voltage is maintained across a TES (voltage biased) a strong negative electro-thermal feedback (ETF) is exhibited in the transition region [30]. ETF allows the TES to self regulate its location within the superconducting transition and maintain linearity over a wider range of temperature

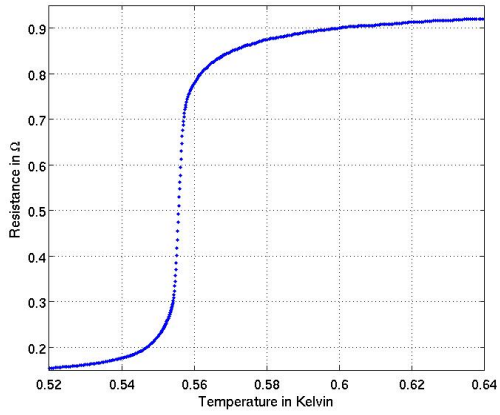

Figure 2.5: A sample resistance versus temperature plot of an SPTpol 90 GHz transition edge sensor bolometer. Note that a small change in TES temperature corresponds to a large change in resistance.

fluctuations.

The first background limited detectors were produced for the Arcminute Cosmology Bolometer Array Receiver (ACBAR) [42]. Detectors are background limited when the noise of the measurement is dominated by the photon noise instead of intrinsic detector noise. After achieving background limited detectors the sensitivity of an instrument can no longer be improved by creating more sensitive detectors. The only way to increase the sensitivity of an instrument equipped with background limited detectors is to add more detectors. TES can be fabricated simultaneously with relative ease as part of detector arrays (see Section 2.2.3). TES array production has allowed the number of detectors in a camera to rise significantly, resulting in a dramatic rise in camera sensitivity.

2.2.2 90 GHz *Detectors*

The SPTpol focal plane contains of 360 individual polarization sensitive 90 GHz detectors. The 90 GHz detectors were fabricated by Argonne National Laboratory and were the first CMB detectors to emerge from the facility. They were fabricated in banks of 20 from a two inch silicon wafer (Figure 2.6) and were diced into individual detectors after fabrication

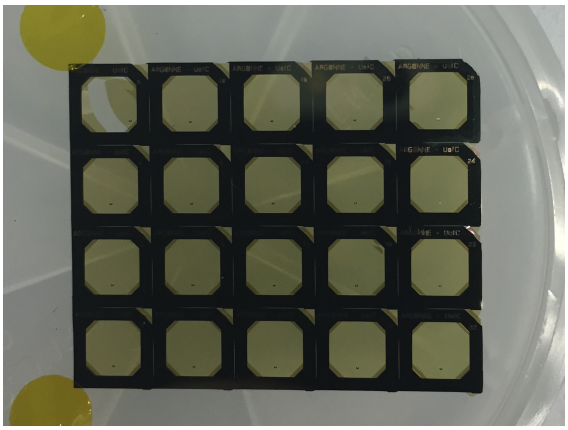

Figure 2.6: A partially completed group of 20 SPTpol 90 GHz detectors. This photo shows the state of the detectors as they emerge from the fabrication prior to splitting the wafer into individual detectors. The fabrication of these detectors was halted before completion so they lack most of the small scale detector features.

completed (Figure 2.7).

Each detector features a silicon nitride island in the center which houses both the absorber and the transition edge sensor (TES). This island thermally isolates the molybdenum/gold bilayer TES from the frame of the detector with 10 μm wide silicon-nitride legs (see Figure 2.8). The TES have micron scale superconducting niobium dots patterned on them and are coupled to an extra thermal mass of palladium-gold commonly referred to as "bling". Both of these features are used to shape the superconducting transition while the bling also acts to slow the TES response to better match the bandwidth of the readout system [18]. The absorber on the island is a gold/palladium bar which absorbs polarized 90 GHz light oriented parallel to the bar. The 90 GHz detectors are completely incoherent since the incoming photons are transferred directly into heat energy on the absorber.

To observe 90 GHz light in both linear polarization orientations two separate 90 GHz detectors are stacked (or "crossed") on top of each other with their polarization axes rotated 90 degrees with respect to each others (see the right side of Figure 2.8). When crossed the detectors are separated by a 25 μm wide piece of wirebond that is bonded to the frame of one of the detectors and flattened. This pair of stacked detectors is installed in a holder that

Figure 2.7: Fully fabricated SPTpol 90 GHz detectors are shown after being split into individual detectors.

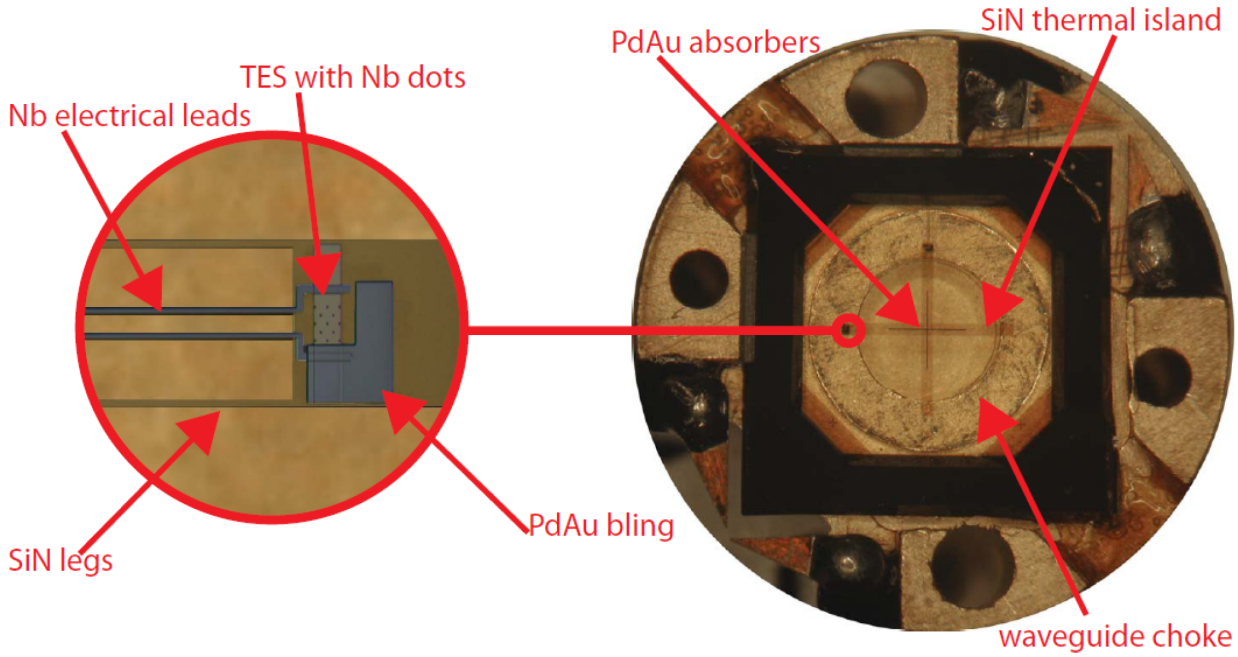

Figure 2.8: A close up view of a crossed pair of SPTpol 90 GHz detectors. The detectors are crossed to create a pixel that is sensitive to both linear polarizations. Image reproduced from [43].

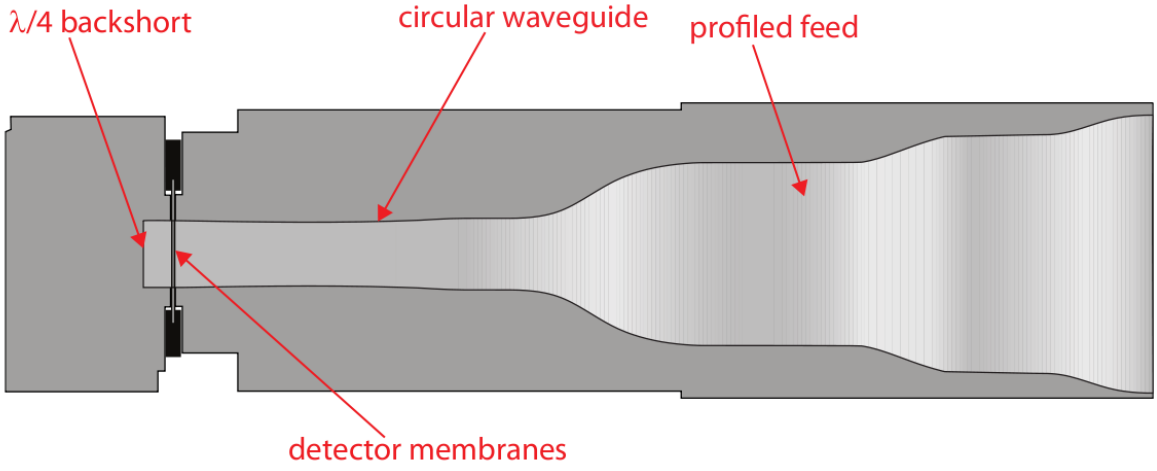

Figure 2.9: A computer generated cutaway drawing of a 90 GHz pixel full assembly, including the smooth contoured feedhorn and back short. Image reproduced from [43].

includes a quarter wavelength back short to match the absorber impedance to waveguide. The stacked detectors share a common monotonicly-widening contoured feedhorn which is single moded for each polarization and acts as the low pass filter for light incident on the detectors [20][50]. The entire feedhorn, back short, and crossed detector package is referred to as a "pixel" (Figure 2.9). The 90 GHz pixels were assembled by a team of graduate students and postdocs at the University of Chicago in Fall 2011.

As shown in Figure 2.3, the 90 GHz detectors are arranged in an annulus around the perimeter of the 150 GHz detectors in the SPTpol focal plane. Though not not visible in Figure 2.3 the 90 GHz detectors are split into four "modules" by four separate circuit boards. The entire array of 90 GHz detectors are behind a common band defining metal mesh low pass filter (filter not shown in Figure 2.3) [1]. The array average bandpass for the 90 GHz detectors as measured with a polarized Fourier transform spectrometer (FTS) at the South Pole is shown in Figure 2.10. Between the 2012 and 2013 observing seasons, the band defining metal mesh filter in front of the 90 GHz detectors was exchanged. The new metal mesh filter raised the upper edge of the bandpass by 4.5 GHz to increase sensitivity to sky signals without encroaching on the 118 GHz atmospheric oxygen line (see Table 4.1 for exact numerics).

See [43] for a more detailed discussion of the 90 GHz detectors produced for SPTpol.

2.2.3 150 GHz *Detectors*

The 150 GHz detectors for SPTpol were fabricated by the National Institute of Standards and Technology (NIST) in Boulder, Colorado. There are 1,176 polarization sensitive 150 GHz detectors located in the center of the SPTpol focal plane (Figure 2.3). The 150 GHz detectors are grouped into seven separate hexagonal "modules". The technology of the 150 GHz SPTpol detectors is briefly discussed here, for more detailed information see [25].

All of the 150 GHz detectors in a module are fabricated together from a single four inch

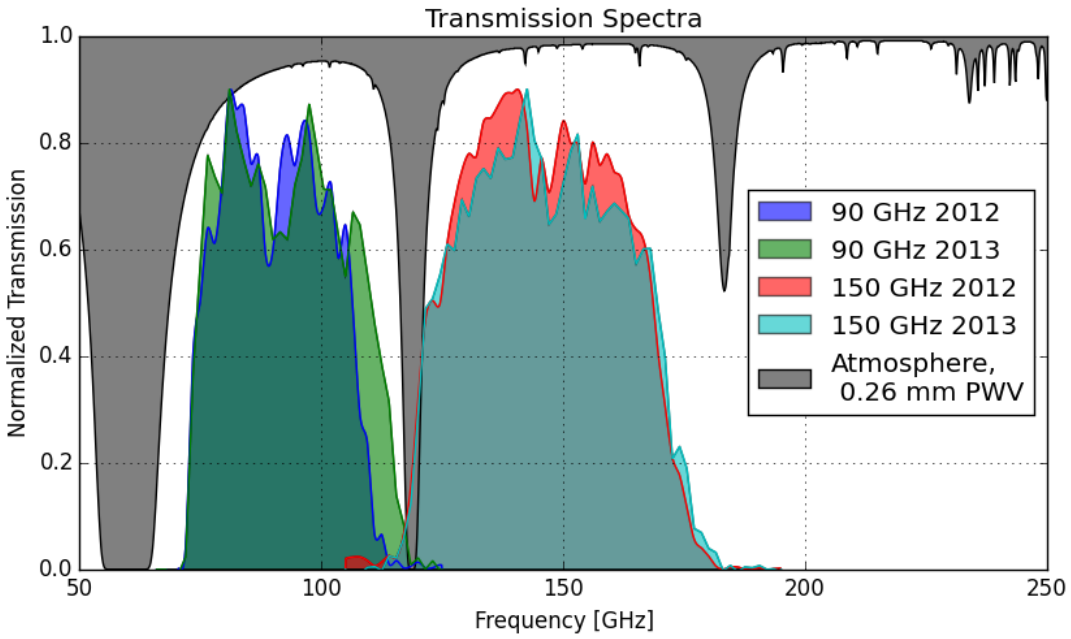

Figure 2.10: SPTpol array averaged transmission spectra (bandpasses) for 90 and 150 GHz detectors are shown. Note the small shift between 2012 and 2013, particularly on the high frequency side of the 90 GHz detectors. The measurements include the etendue (product of the solid angle and area illuminated) of the combined detector and feedhorn system. In grey area indicates the atmospheric transmission at zenith for 0.26 mm of precipital water vapor (PWV) at the South Pole. The bands are specifically tuned to avoid the atmospheric oxygen lines at 60 GHz and 118 GHz and the water line at 182 GHz. *Note:* The normalization of the SPTpol bandpowers are arbitrary. They are meant to show the avoidance of the atmospheric transmission.

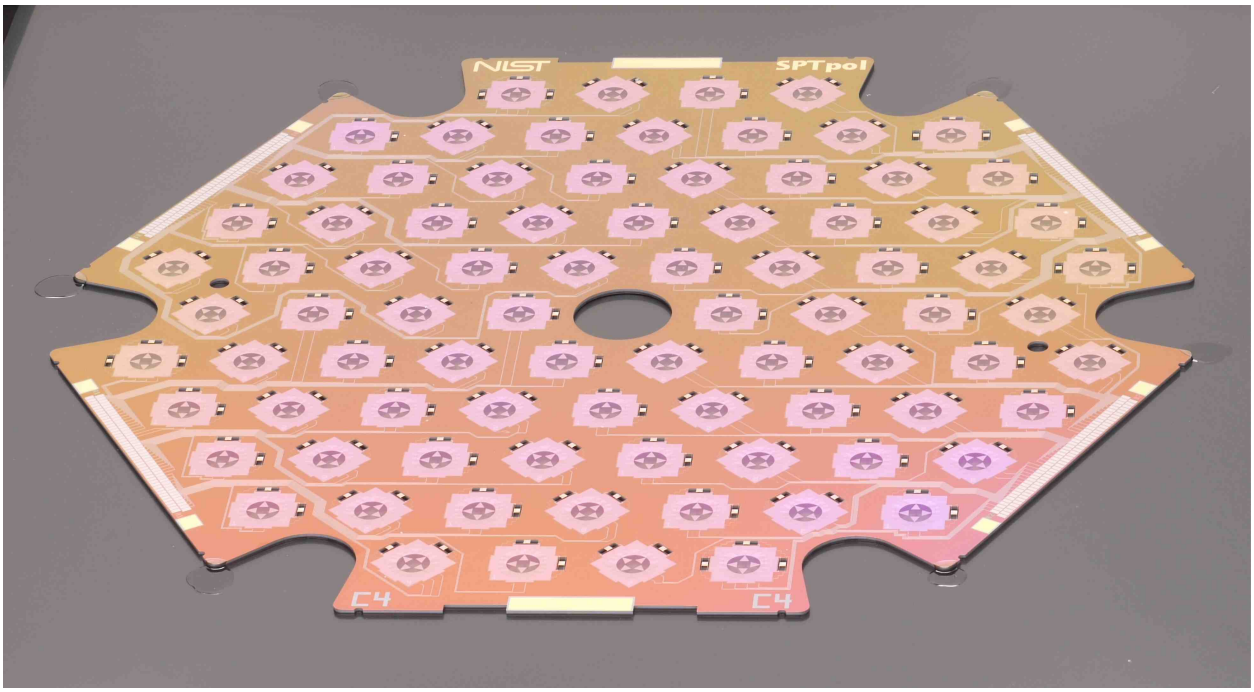

Figure 2.11: A 150 GHz detector wafer fabricated by NIST at Boulder, Colorado is shown. A total of 168 detectors (84 pixels) are fabricated together on a single 4 inch silicon wafer [25].

silicon wafer (Figure 2.12). Unlike the 90 GHz detectors, the fabricated 150 GHz detectors are not split into individual detectors. The polarization sensitivity of the 150 GHz detectors is provided by an orthomode transducers (OMT) that splits the incident light into two linear polarizations (Figure 2.12). Each linear polarizations is then coherently sent through coplanar waveguide to a niobium microstrip that terminates on a lossy gold resistor. The lossy gold resistor is responsible for converting the radiation from the microstrip to thermal energy and is located on an island that is thermally isolated by narrow silicon legs from the rest of the wafer. An aluminum/manganese alloy TES located on the island is sensitive to the energy deposited by the gold meander through a measured temperature rise [1].

All detectors within a module share a monolithic corrugated feedhorn array which was fabricated by NIST in Boulder, Colorado. The feedhorn array has 84 separate corrugated feedhorns (one per pixel) and is made of a stack of 33 silicon wafers each 500 μm thick [27]. Prior to being stacked each silicon wafer was precision etched to create two different diameter circular holes which share a cylindrical axis. When wafers are stacked these circular holes will become the corrugations of the feedhorns. Each wafer is individually plated with titanium-copper before being stacked into the full array, which is then gold plated. The gold plating helps keep the stack of wafers isothermal and reflective to incident radiation. Excess radiation absorbed by the feedhorn array will heat up the cold stage in the cryostat and raise the detector base temperature.

2.3 Digital Frequency Multiplexing Readout

The thermal budget required to keep the SPTpol bolometers below 550 mK necessitates a multiplexed readout system. In the muliplexed readout system many detectors share a common electrical connection. For SPTpol, this means many bias lines (which are the same

1. The tempature of the island does not actually rise. As the temperature begins to rise the electro-thermal feedback of the TES compensates and changes the current running through the voltage-biased detector, keeping the island the same temperature.

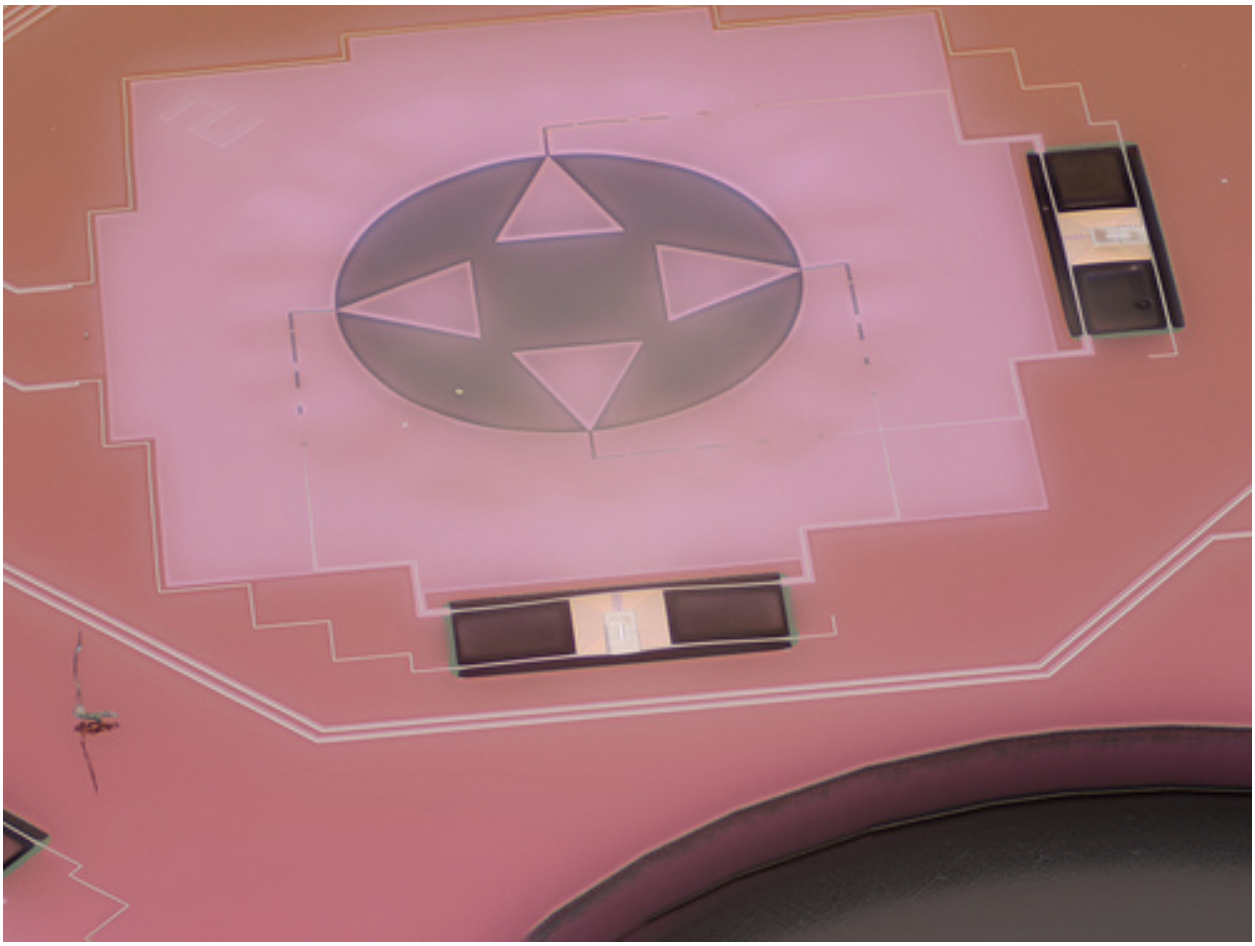

Figure 2.12: A detailed view of a pair of 150 GHz detectors are shown. The center circle the orthomode transducer (OMT) fins can be seen as triangles. Each pair of fins couples to a single linear polarization and is responsible for coupling 150 GHz radiation to the patterned microstrip. The radiation travels down the microstrip until it is terminated on a lossy gold resistor in the center of the suspended silicon nitride island.

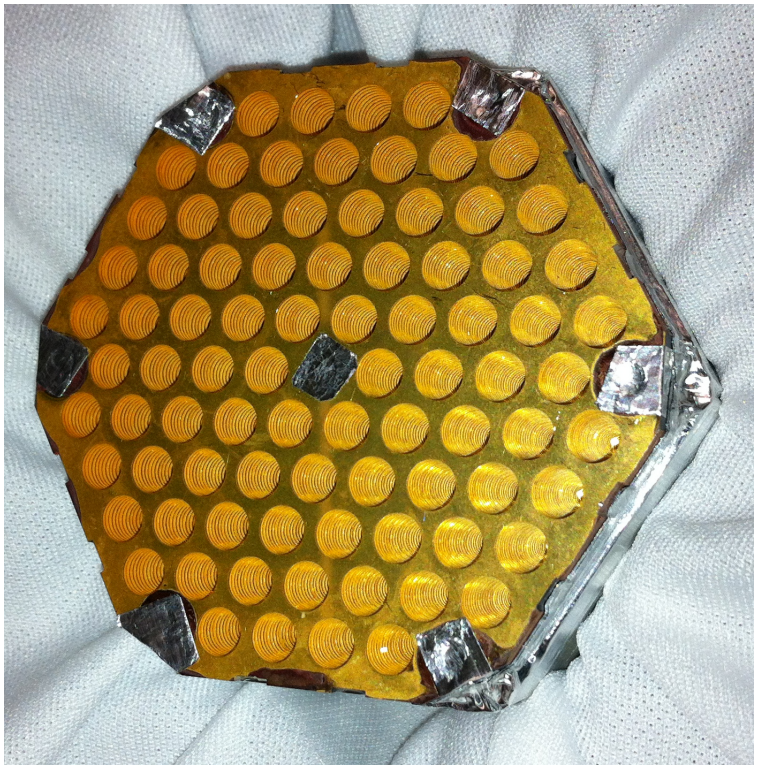

Figure 2.13: A 150 GHz feedhorn array for SPTpol is shown. Each feedhorn array is made of 33 separate precision etched silicon wafers. The silver Aluminum tape on the top of the array indicates areas that do not have active detectors underneath, the tape was removed for deployment.

as readout lines here) share a single cable. Multiplexing keeps the thermal load down by minimizing the thermal connections to the detector stage from hotter temperatures. For SPTpol, 12 detectors share a common bias/readout line from 4 K to 250 mK with each detector bias being applied at a different frequency [13]. At the 250 mK stage each detector is connected to its own inductor-capacitor (LC) filter, including the detector a resistor-inductor-capacitor (RLC) filter is created. All RLC filters share the same inductor, but the capacitor of each RLC filter on a common line is unique so that each detector is sensitive to only one bias frequency on the multiplexed line. An example network analysis of a readout line showing the RLC resonances corresponding to 12 TES detectors can be seen in in Figure 2.14.

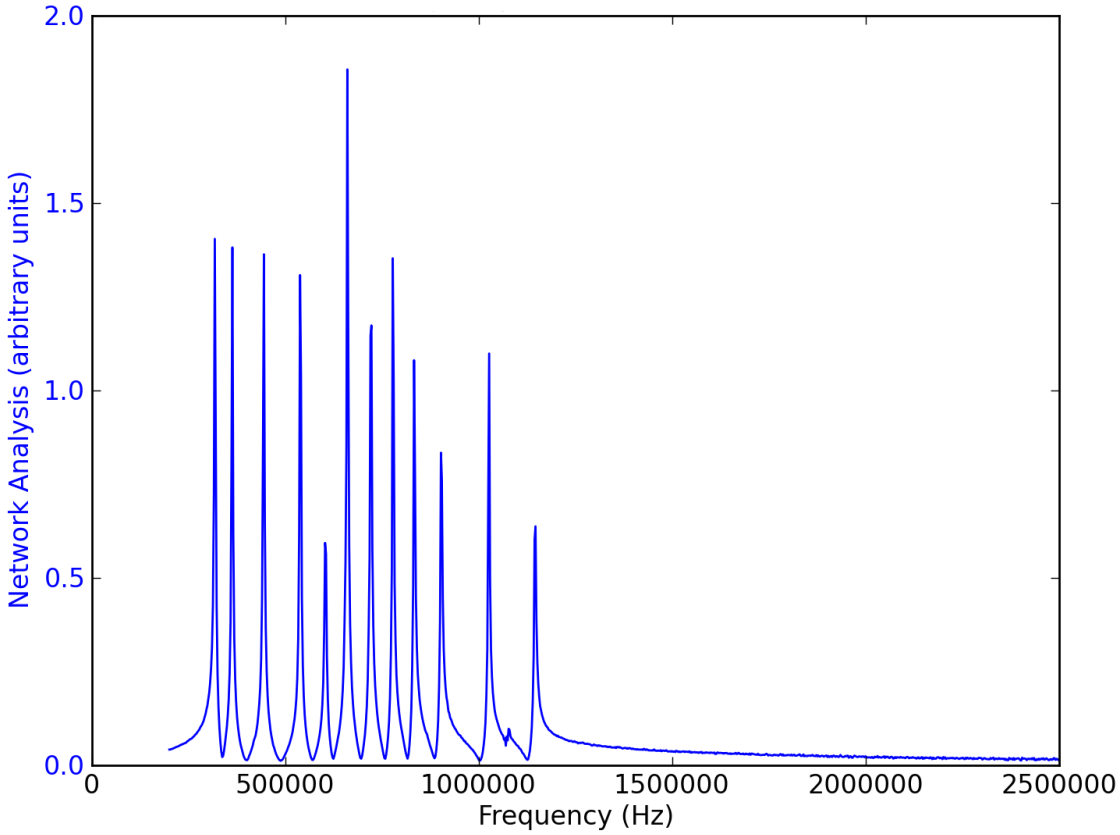

Figure 2.14: The frequency response of a bank of 12 LCs which split the 12 bias frequencies on a multiplexed line for into individual lines for each detector.

CHAPTER 3

DATA PRODUCTS

3.1 Observation Strategy

The field observed by SPTpolin the first year of observations was chosen to optimize observations of gravitationally lensed cosmic microwave background B modes ([28]).

The observing strategy employed, namely repeated observations of the same patch of sky with a high cadence, also produces a rich data set for a transient analysis. Below we discuss the specifics of the observing strategy and low level processing of the data.

Observations of a roughly ten degree by ten degree (100 $\deg^2$ total) patch of sky centered at right ascension (RA) 23 hours 30 minutes and declination -55 degrees (referred to as the 100 $\deg^2$ field from now on, Figure 3.1) were taken with the SPTpol instrument from April of 2012 to April 2013. There was an observation gap of approximately 4 months (December 2012 to late March 2013) when the Sun was contaminating the field and no observations of the 100 $\deg^2$ field were made.

Observations were performed in a scan strategy known as "lead-trail". This scan strategy splits the 100 $\deg^2$ field vertically into two equal sized fields. The lead half of the field (the left half) is observed first by scanning the telescope at fixed elevation 7.5 degrees in RA left and right, then stepping in elevation and repeating the process. This scanning is repeated until the scan elevation reaches the top of the lead field. The elevation step size is chosen such that the observation of the lead field takes 30 minutes, the amount of time it takes for the lead field to move exactly 7.5 degrees in RA across the sky. At the conclusion of the lead field observation the trail field (the right half of the original 100 $\deg^2$ field) is at the same ground coordinates as the lead field was when it was observed. The basic concept of the lead-trail observing strategy is to observe both the lead and trail fields over the same ground position. This allows for the lead and trail fields to be differenced and then analyzed

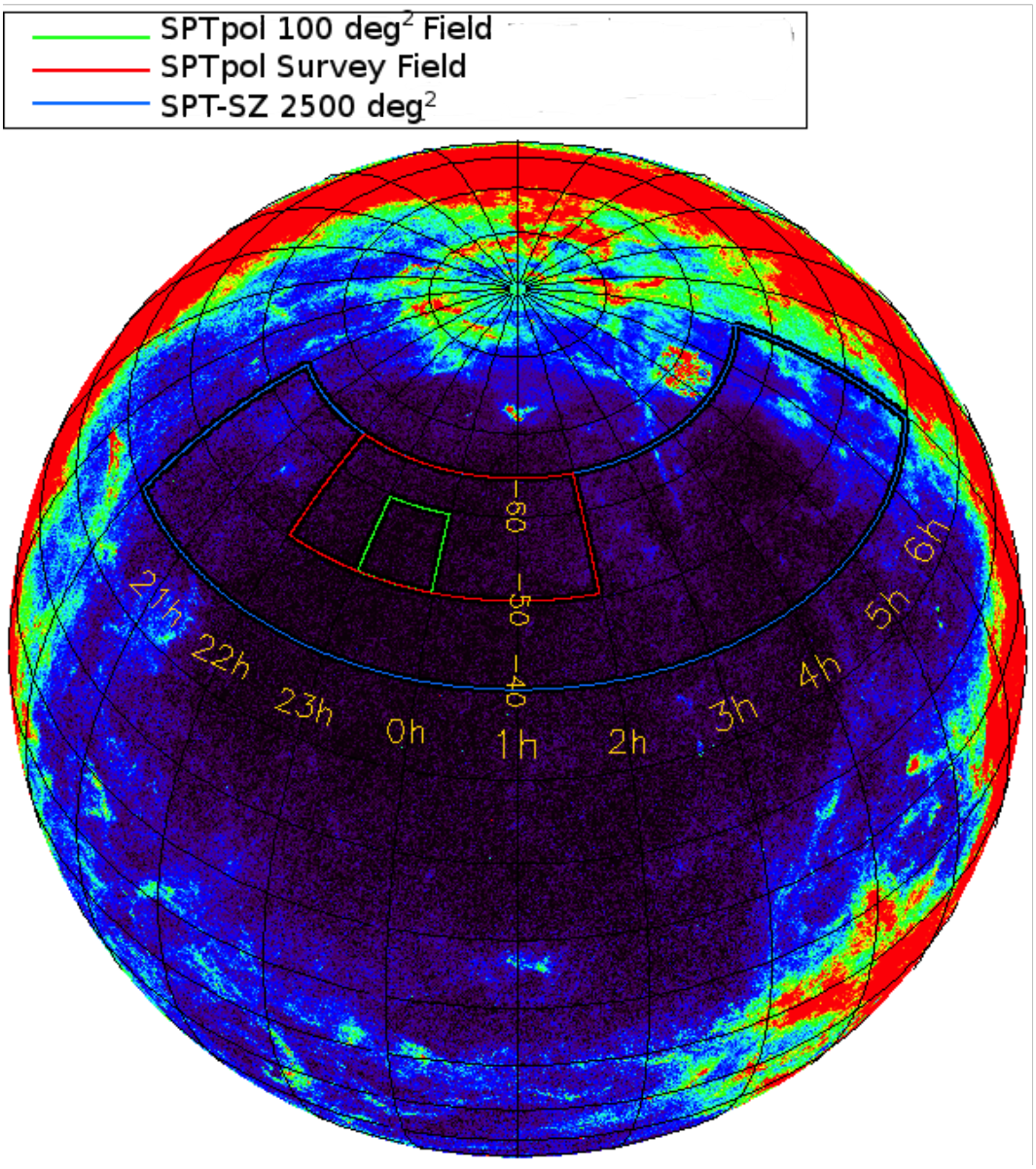

Figure 3.1: The SPT-SZ and SPTpol survey regions are outlined on a dust intensity map from *Planck*[1]in celestial coordinates. The bright colors in the background *Planck* map represent more dust (with red indicating the most dust) while the darker blue colors represent less dust. The SPT-SZ and SPTpol fields are in a less dusty part of the southern sky, this area is referred to as the "southern hole". At SPTpol observation frequencies galactic dust is a foreground and overpowers photons from the cosmic microwave background or extragalactic sources. The image is orientated such that the pole observed is the South celestial pole.

to eliminate effects due to ground pickup [40]. It was demonstrated in [11] using jackknife null tests of the 100 deg^2 field that there was no sign of significant ground pickup. For this analysis, we will not difference the lead and trail fields and instead will simply add the lead and trail fields together to create a map of the entire 100 deg^2 field.

In this document each left or right pass of the telescope will be referred to as a "scan" and each lead or trail field data set will be referred to as an "observation".

3.2 Data Cuts

The data written to disk from the telescope is in the form of timestreams of individual detectors (seen in Figure 3.2) and information related to where the telescope is pointing. The detector timestreams are recorded at 190.92 samples/second and are kept at this sample rate for the analysis presented here. After filtering (Section 3.3.3), the timestream data go through a series of quality assurance cuts at the level of individual scans of a bolometer and entire bolometer timestreams for an observation. The timestreams are then combined with pointing information to create maps.

3.2.1 Scan Cuts

Individual scans (left and right scans independently) for a bolometer can be cut for a few different reasons. Before any of the scan cut criteria are enforced each scan is filtered as discussed in Section 3.3.3. A bolometer scan is cut if it contains a single sample that is 4.5 times the root-mean-squared (RMS) away from the median value of the scan. A single high value in a scan is either caused by a cosmic ray hit or a readout glitch. Occasionally scans also experience discrete DC jumps in their values, this is most likely caused by the superconducting quantum integrating devices (SQUIDs) in the readout chain experiencing a jump up or down in bias location (also known as a "flux jump") [49]. Bolometer scans are also cut if the RMS of that scan is 3.5 times greater or 0.25 smaller than the average RMS

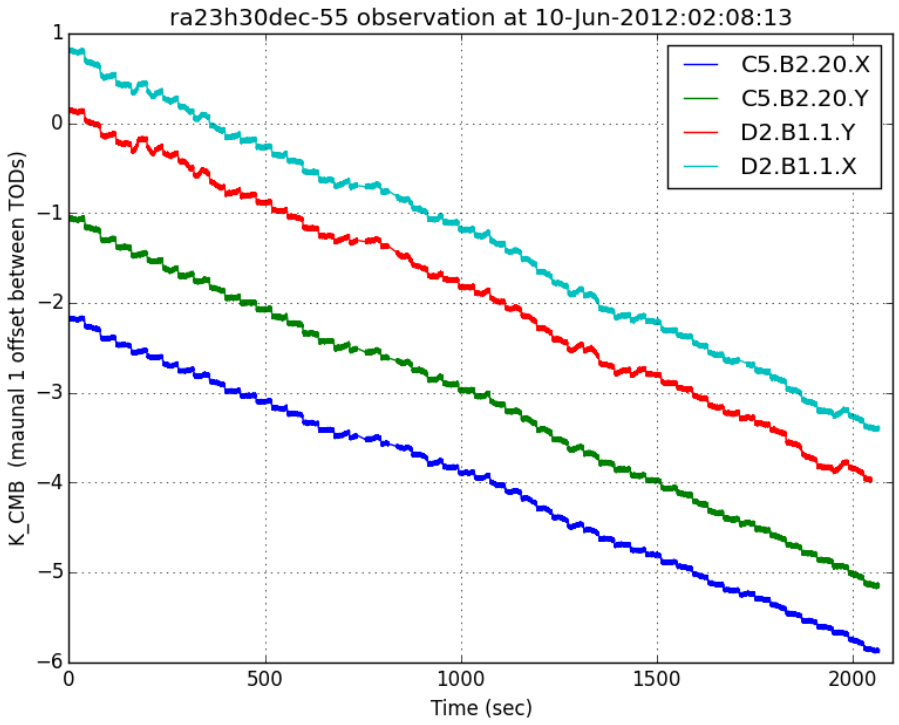

Figure 3.2: Sample timestreams from two 150 GHz SPTpol pixels (a total of four bolometers) are shown for an entire observation. Each color shows a timestream from a different detector and there has been an artificial DC offset put in place for ease of viewing. The airmass contribution can be easily seen as steps in the timestreams. The non-smooth features of the atmosphere (clumps, turbulance) can also be seen as correlations between X and Y detectors of the same pixel.

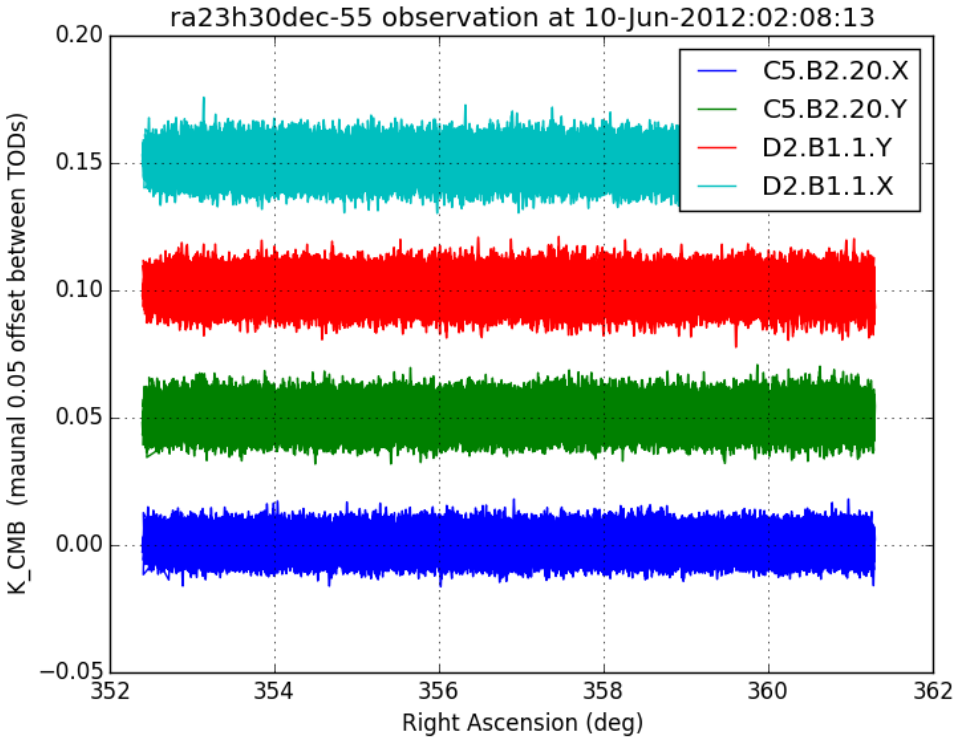

Figure 3.3: Sample timestreams from two 150 GHz SPTpol pixels (a total of four detectors) are shown for an entire observation. Each color shows a timestream from a different detector and there has been an artificial DC offset put in place for ease of viewing. The timestreams shown are the same as in Figure 3.2 except now they have been scan filtered (see Section 3.3.3). You can clearly see the airmass contribution has been removed. These timestreams, along with the rest of the observations timestreams, are included in the map in Figure 3.7.

for other bolometer scans within the same module.

3.2.2 Bolometer Cuts

Entire bolometers are cut from being used in maps based on a number of performance diagnostics and calibration values. Any bolometer that does not have a value for the polarization angle or pointing is eliminated from being in any maps. In 2012, the 150 GHz module C4 had anomalously high noise compared to the other modules and was not included in any 2012 maps. The C4 module was replaced in 2013, this change makes the 2013 150 GHz observations about 15% more sensitive than the 2012 observations. All scans for a bolometer are excluded from a map if five or more scans were cut for that bolometer in an observation (see Section 3.2.1). Bolometers are cut if they exhibit a signal-to-noise response less than ten to an internal chopped thermal source or RCW38 (a galactic HII region), or a signal-to-noise response less than 100 for two degree elevation dips (elnods) which modulate the loading due to a shift in atmospheric line of sight thickness (airmass). The final bolometer wide exclusion is for bolometers whose pixel partner is cut for any reason. This "full pixel" cut guarantees roughly even polarization coverage across the observation field.

3.3 Map Making

Map making refers to the process of making images of the sky from individual detector timestreams. Before this process can start some processing must be performed on the timestream data, this includes pointing, notch filtering, and relative timestream calibration.

3.3.1 Data Processing

Using a combination of short observations of known sources and sensors on the telescope that record physical parameters like tilt and temperature, the telescope's sky pointing during an

observation can be fully reconstructed. This is an offline correction, meaning it happens after observations have been taken, and typically corrects the telescope pointing by five arcminutes.

The optics and receiver pulse tube coolers switch between high and low pressure, this switching causes some narrow frequency spikes in the detector timestreams. This pickup is at the pulse frequencies of the coolers and can be seen as narrow lines at 1.54 Hz and 1.58 Hz in Figure 3.4. These two frequencies are "notched" out of the timestreams along with harmonics up to the third harmonic of each.

Gain factors (multiplicative amplitude factors) of detectors will vary between detectors based on the shape of their superconducting transition and thermal link. The gain factor of even a single bolometer will vary depending on its bias location within the superconducting transition. To account for both gain variations in time and between detectors, relative gain corrections are created for each bolometer for each observation. Each correction is computed using a combination of frequent stares at an internal chopped thermal source and less frequent dedicated observations of RCW38. The relative correction also uses module averaged responses to these sources to account for intensity variations in the thermal source or changes in atmospheric opacity. The relative correction factor ultimately converts timestream data from watts to CMB equivalent temperature variations, K_{CMB}.

3.3.2 Map Projection

Maps for this analysis were made in the Sanson-Flamsteed flat sky projection [7]. This projection turns constant elevation scans into rows of the produced map. The y axis of the map is the cosine of declination multiplied by right ascension, Figure 3.5 shows a full coadd of the 100 deg^2 field in this projection. This projection allows scan filtering to act solely on map rows, which makes it more straight forward to to understand filtering effects. Figures 4.4 and 4.6 show how easy it is to identify the effects of the scan filtering in Fourier-space of

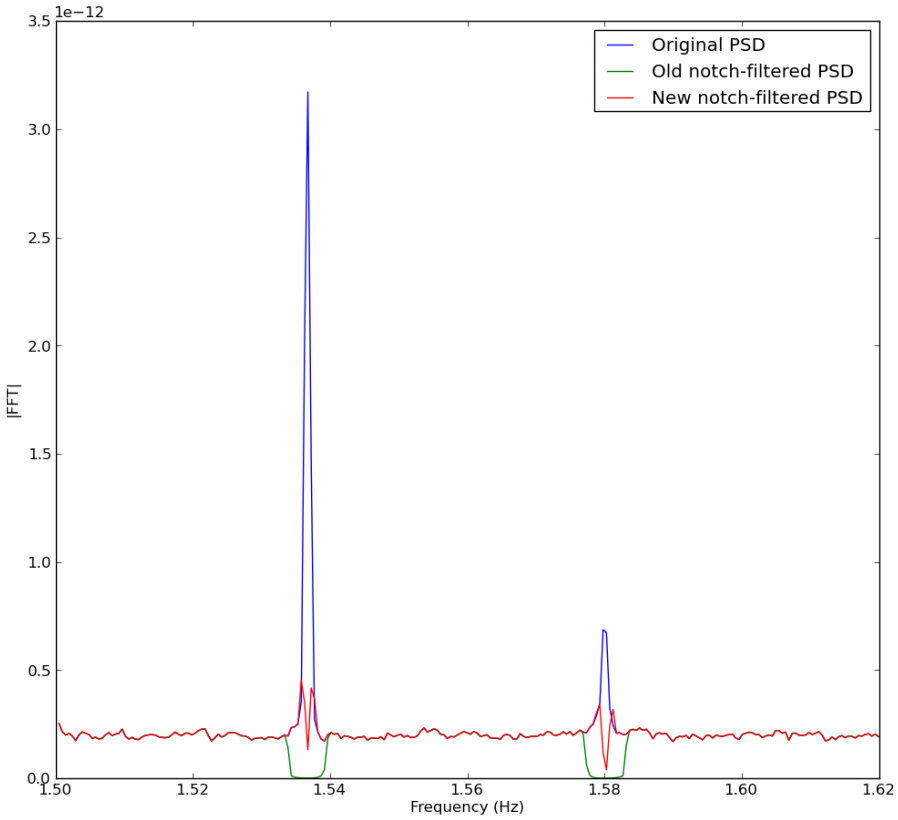

Figure 3.4: Pulse tube frequencies seen in a timestream FFT. Also shown are a few earlier iterations of possible line notching techniques.

a Samson-Flamsteed projection, particularly the high and low pass filtering.

3.3.3 Scan Filtering

Any single raw observation made with SPTpol will be dominated on large scales by the gradient of the atmosphere. The atmospheric gradient caused by the atmospheric line of sight thickness (airmass) changing from the bottom to the top of a 10 degree tall field can be seen in Figure 3.6. The change in the atmospheric line of sight thickness (airmass) from the bottom to the top of a 10 degree tall field is large enough to be the dominant feature observed in a raw map, see Figure 3.6. This gradient airmass contribution can be removed by subtracting a mean from every scan, since all scans are constant in elevation. After the mean scan subtraction the dominant structures observed are large clumps from the turbulence of the atmosphere (patches of different atmospheric thickness) and degree scale features from the CMB. These modes are much larger in spatial scale than transient sources and are removed from the maps by applying 3 different filtering techniques: a module by module common mode is subtracted, polynomials up to order 7 are fit to and subtracted from every scan independently (where the area around known bright point sources are omitted from the fit), and a high pass filter corresponding to an ℓ_x of 400 is applied to the scans. Scans also have a low pass filter at an effective ℓ_x of 20,000 applied to them to prevent aliasing. A scan filtered version of the map shown in Figure 3.6 can be seen in Figure 3.7. All of this filtering is done in the scan direction (except the common mode), which is in the azimuthal direction for SPT observations. The effects of this scan filtering can easily be seen in Figures 4.4 and 4.6.

The pixel size for maps in this analysis were chosen to be 0.25 arcmin to achieve a resolution better than the nyquist frequency for the 150 GHz beam of just over one arcmin.

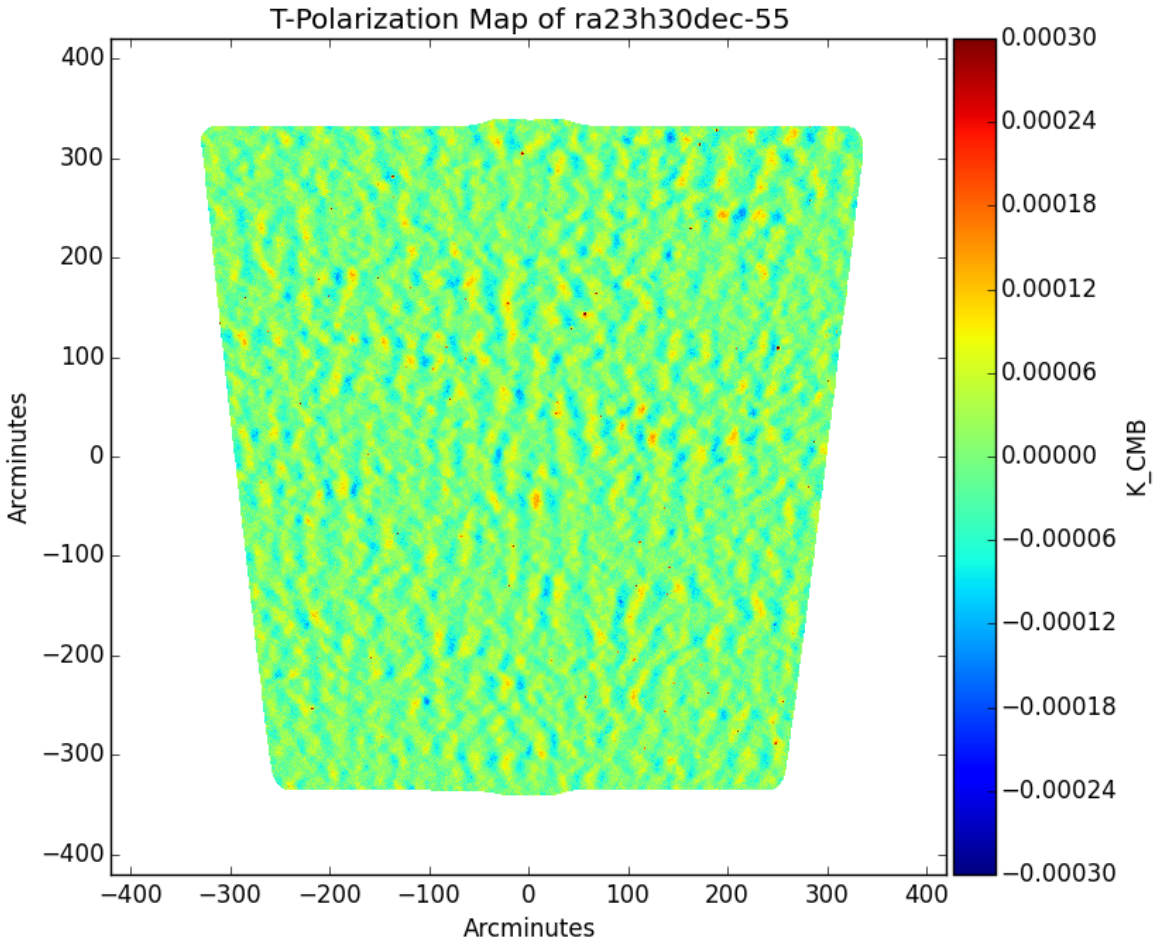

Figure 3.5: A coadd of all maps created for this analysis that pass cuts. The map is created in Sanson-Flamsteed flat sky projection which turns scans of constant elevation into rows of map pixels. The color scale of the map saturates the brightest point sources.

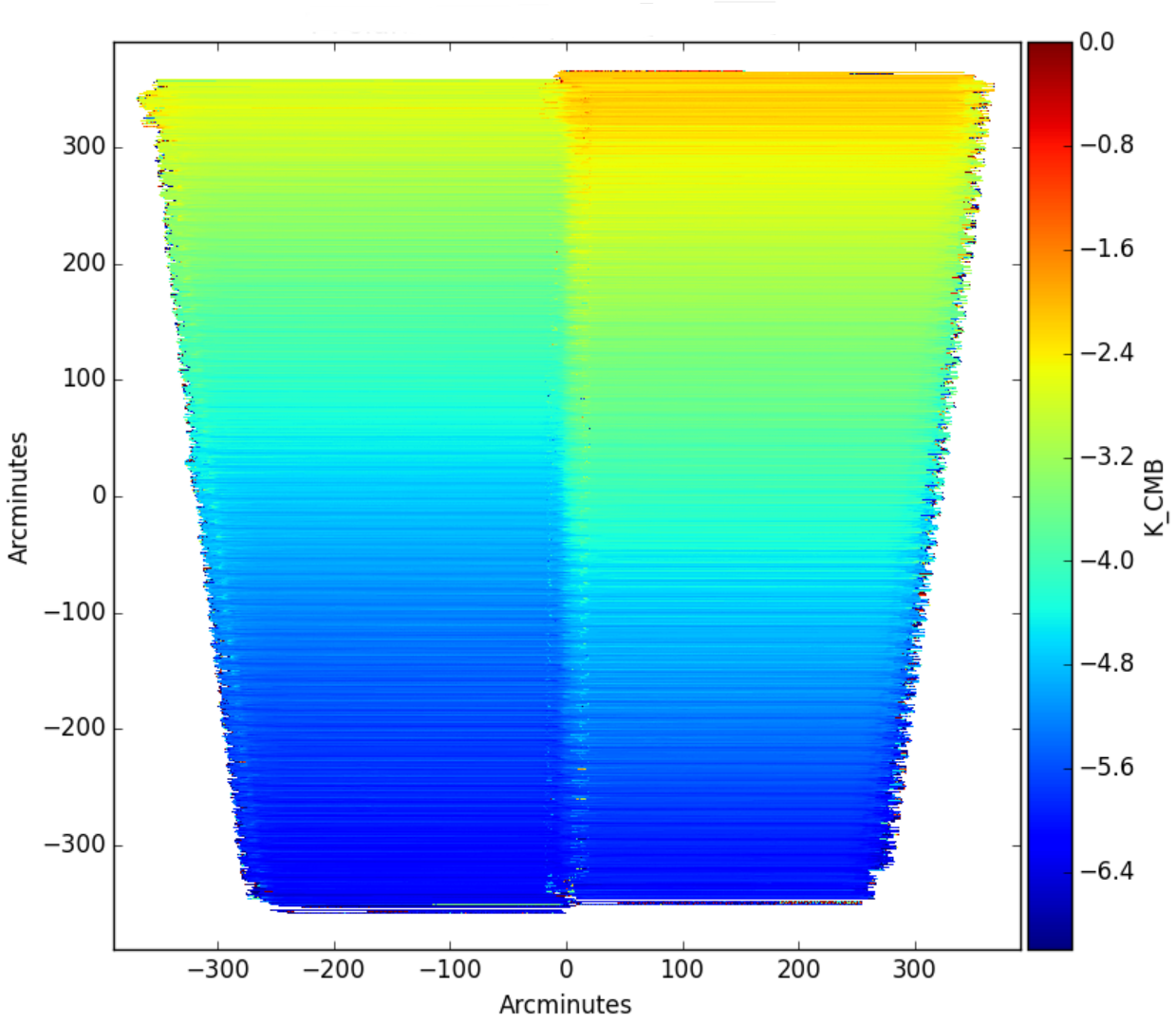

Figure 3.6: A sample 150 GHz coadd of lead and trial observations is shown without any scan filtering. The airmass contribution manifests itself as a slope across the field from top to bottom and can easily be seen as the most striking feature of the raw map. The boundary between lead and trail fields can also be seen in this figure as a seam down the center of the 100d field. The shown map has one arcmin pixels, is the Sanson-Flamsteed projection, and has undergone minimal bolometer cuts.

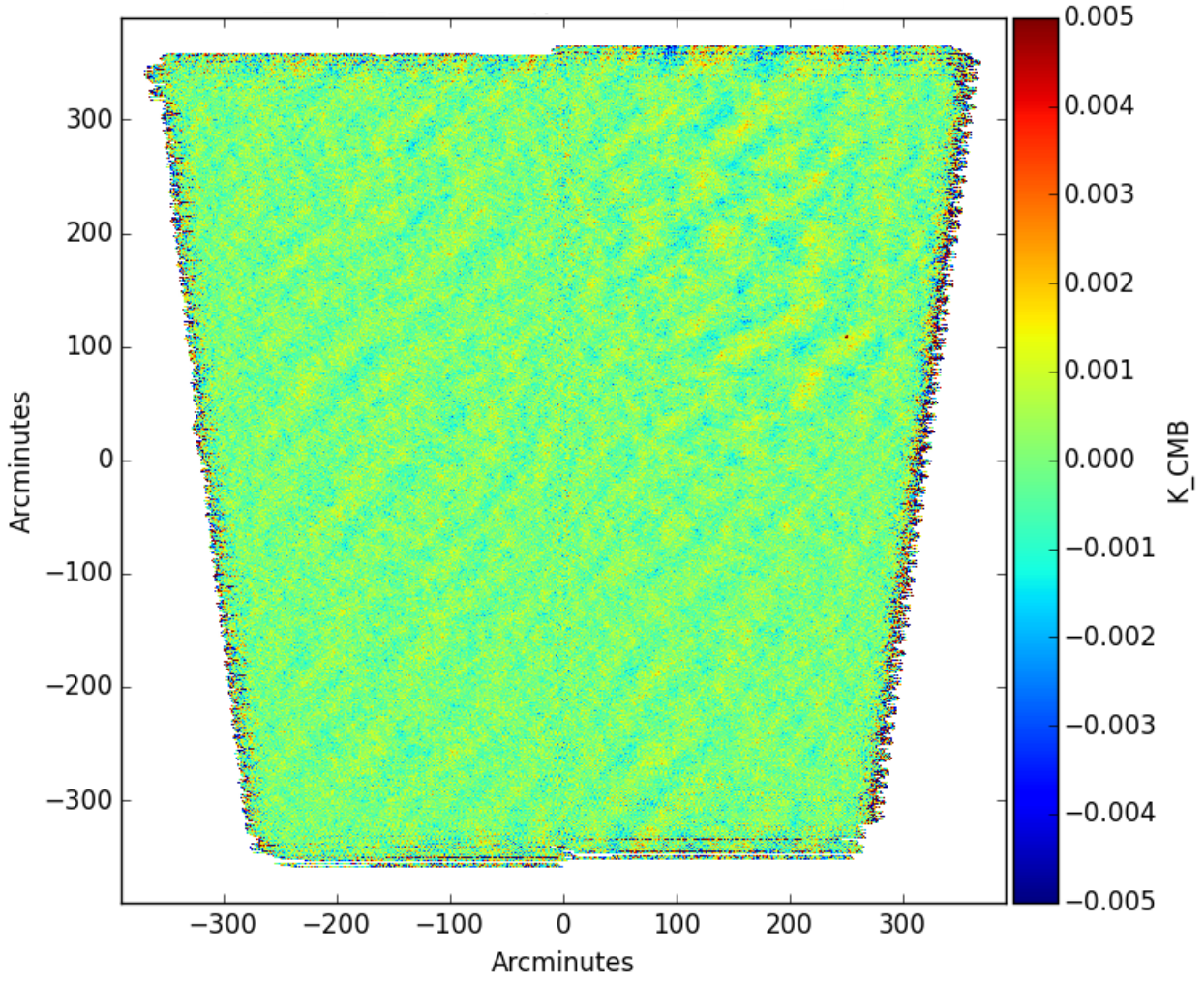

Figure 3.7: A sample 150 GHz coadd of one lead and one trial observation is shown with filtering used for this analysis (see Table 3.3.2). In comparison to Figure 3.6 you can see the airmass contribution has been completely eliminated. Also note the scale difference between these two sets of maps. The boundary between lead and trail fields can be vaguely seen in this figure as a seam down the center of the 100d field. The shown map has one arcmin pixels, is the Sanson-Flamsteed projection, and has undergone minimal bolometer cuts.

3.3.4 Map Weights

Each pixel within a map is assigned a weight based on the inverse of the PSD (power spectral density) of detectors passing through that pixel. The PSD is calculated individually for each detector between 0.8 Hz and 3 Hz of left minus right scans. Left minus right scans are used to calculate the PSD because left minus right scans will subtract out the CMB and sky sources so only noise will be left. The pixel weights indicate how much each pixel value resembles the true sky signal compared to other pixel values. Pixels with larger weights will be more accurate measurements of the actual sky value than pixels with lower weight. Over most of the observation field the weight will be roughly constant, but along the edges of the field and other locations with incomplete coverage the weights play a larger role. The weights are used for map cuts (Section 3.3.5), border apodization mask creation (Section 3.3.7), and for adding observations together during bundling (Section 3.3.6).

3.3.5 Map Cuts

Since maps are assigned a weight based on the inverse of their variance it is tempting to not remove any maps from the analysis and simply let the weighting do the work of down-weighting nosier maps out of relevance. This works great for maps that have the appropriate correlation between the calculated variance and the sky signal in the map, which is the case for most of the maps, but not all. Maps targeted for being cut from the analysis are maps which exhibit strange systematics which are not captured by calculating the map variance.

The map cuts for this transient analysis are based off of the map cuts for the 100 $\deg^2$ BB analysis, see [28] for more specific information. The main difference between map cuts for this transient analysis and the BB analysis is this analysis does not demand the map cuts be the same for 90 and 150 GHz. There are also an additional roughly 70 maps cut at 90 and 150 GHz for this analysis, which were identified as suffering from a readout conversion issue. Table 3.1 shows the numbers of maps cut for this analysis.

Cut	90 GHz	150 GHz
median weight	281	495
total weight	422	478
RMS*weight	211	430
RMS	193	420
number of bolos in map	170	448
bad tilt info	99	99
Sun contaminated	643	643
readout error	71	51
too few maps in bundle	61	74
Remaining maps / total maps	5110/6464	5056/6464

Table 3.1

Map cuts for 90 and 150 GHz maps for this analysis are listed. Many of the cut maps are cut by more than one criteria.

3.3.6 Map Bundling

Due to coverage issues from using small pixels, maps of single observations will not have values in every pixel. This makes additional map filtering in Fourier space difficult since the maps will have discontinuities around pixels with no values. To create maps with full coverage many maps are added together to create a map "bundle" using the map pixel weights (see Section 3.3.4). Since transient analysis is a time domain analysis maps must be summed into bundles in a chronological manner. The boundary for map bundles was chosen to be when the cryogenic fridge recycles. Every 36 hours the fridge that keeps the bolometers at 250 mK runs out of cooling power (specifically the helium 3 is all boiled away) and must be recycled, which takes roughly 8 hours. This means there is a roughly 8 hour observation collection break after every 28 hours of observing. We use this observation break as the boundary for bundles to match the natural observation cadence of the telescope.

If during a fridge cycle there are less than 10 observations remaining after map cuts the bundle will have poor coverage and that bundle and its observations are cut, see the "too few

maps in bundle" cut in Table 3.1. There are an average of ∼maps in a bundle. For 90 GHz this cuts 61 observations and for 150 GHz this removes 74 observations from the analysis.

For more information on the specific bundle set used for this transient analysis see Section 4.2.

3.3.7 Apodization Masks

As shown in Figure 3.6, the edges of individual maps have ragged edges and areas of poor coverage. Bundles have more uniform coverage around the edges but the weight of the bundle still falls sharply at the edges. Sharp features (discontinuities) in the bundles will cause issues when transforming between real-space and Fourier-space (and back again). To soften these sharp map edges we use a border apodization mask, sometimes referred to as a "sky window function". For this analysis, we have created a border apodization mask that removes the sharp border features for every bundle in the 100 $\deg^2$ data set. To create this shared border apodization mask we apply a threshold to every bundle at 30% of the average weight of the bundle map. We then multiply all of these thresholded maps together, and apply a 20 arcmin cosine around its perimeter to get the border apodization mask. This ensures that the border apodization mask has soft edges and works for every bundle in this bundle data set. The border apodization mask used for this analysis can be seen in Figure 3.8.

A point source apodization mask is also created that we apply to every bundle. Point sources detected at 150 GHz with a 50 sigma significance or above are masked with a 5 arcmin radius circle.The edges of the masking circle are smoothed with a cosine like the border apodization mask to smooth sharp features. The point source apodization mask combined with the border apodization mask can be seen in Figure 3.9.

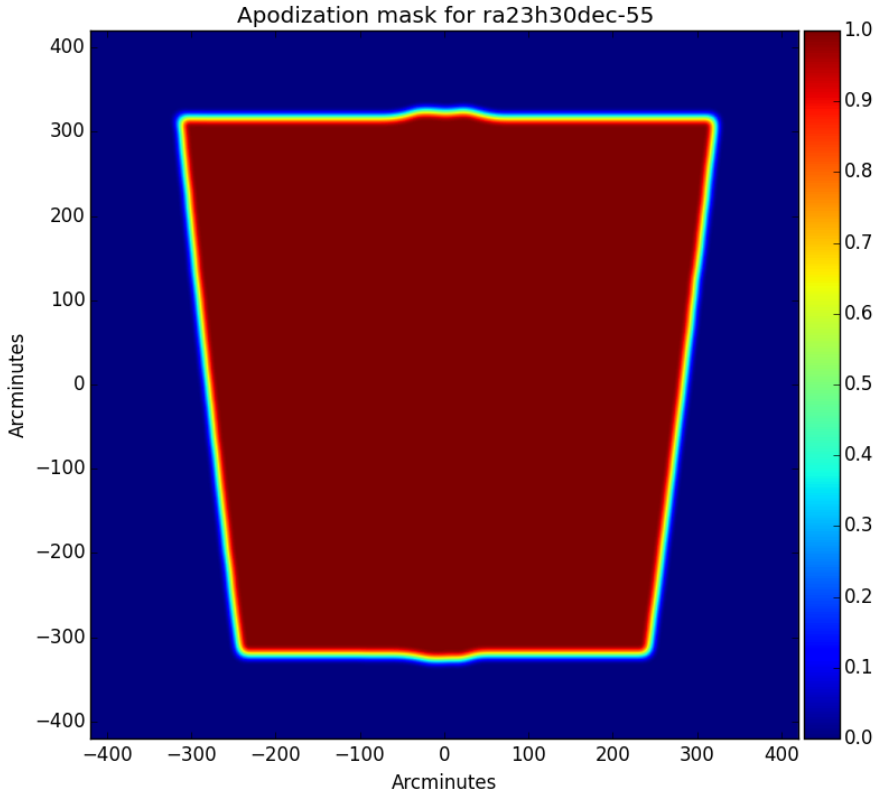

Figure 3.8: The border apodization used for this analysis is shown. This apodization mask will work for every bundle in this data set. The edges of the mask have a cosine profile to eliminate sharp features which cause issues when performing Fourier transforms.

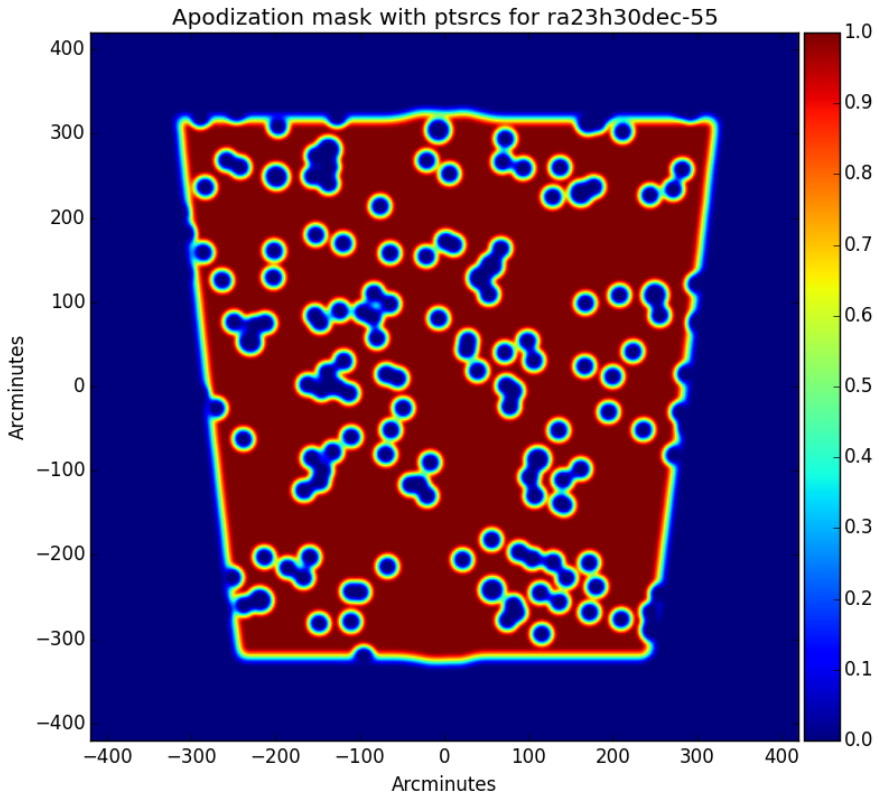

Figure 3.9: The combination point source mask and border apodization mask are shown. All sharp edges have been smoothed to create an apodization mask that makes bundle maps transform to Fourier-space nicely. This analysis took a conservative approach of masking known point sources well below the noise level of individual map bundles.

CHAPTER 4

TRANSIENT ANALYSIS

This is the first time a transient source analysis has been performed on SPT data and as such a new analysis technique had to be developed. All Chapters preceding this describe data preparation techniques that are general to a few types of SPTpol analyses. Discussions within this Chapter concern data manipulation and analysis methods performed on SPTpol data for the first time. Sections leading up to Section 4.3 discuss the specific map bundle processing and map bundle data products used for this transient analysis. Section 4.3 describes a new analysis technique for SPT data that adds time information to source identification.

4.1 Bundle Processing

The process of combining individual observation maps into bundles was described in Section 3.3.6. Bundling serves to alleviate coverage issues while minimizing the dilution of transient sources by creating map coadds with chronologically grouped observations. Each map bundle contains observations from a single fridge cycle, or roughly a 28 hour window. This timescale is well matched to the expected length of GRB afterglows of days to weeks [33].

Even though the map bundles are well matched in time to transient sources and have undergone scan filtering, more filtering can be done to better spatially match transient sources. This spatial processing is described in Section 4.1.2 and makes use of an optimal filtering routine while section 4.1.3 outlines a conversion to a more appropriate unit for astronomical sources.

4.1.1 Bundle Calibration

We can check the relative calibration across map bundles by creating light curves for known sources in the 100 $\deg^2$ field. Figure 4.1 shows light curves at 150 GHz for the five brightest

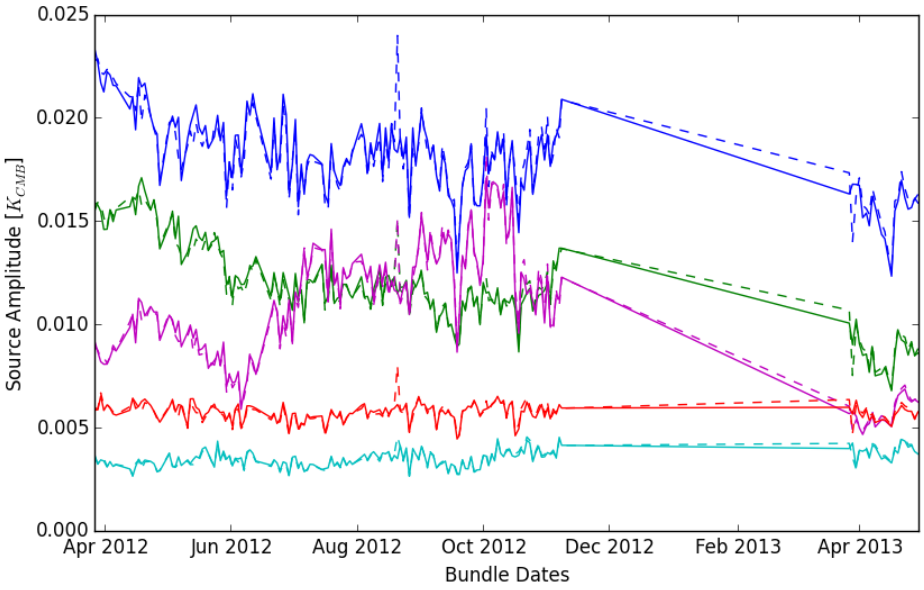

Figure 4.1: The brightest five sources in the 100 deg^2 field are shown as a function of time. Each color denotes a different source with the solid lines representing the corrected versions of the dashed lines. The correction is the CMB based amplitude correction discussed in Section 4.1.1. The brightest sources show large variability with coherent trends over the entire time range shown.

sources in the 100 deg^2 field. A few of the sources shown exhibit large variability with amplitude trends that span the entire year of data. There are sizeable single bundle outliers in the light-curves of the bright sources with outliers being correlated between all sources shown. The outlier bundles are consistent with a systematic shift in the amplitude of a few bundles and cannot be the result of any physical process. To correct the outlier 150 GHz bundles a CMB based amplitude correction was implemented, described in detail below.

Prior to any spatial filtering (discussed in section 4.1.2) the map bundles are dominated by CMB power fluctuations. The CMB fluctuations in a coadd of all bundles can be used as a reference measurement to relatively calibrate the bundles. The normalized one dimensional (azimuthally averaged) cross spectra of bundle i, b_i, with a coadd of all bundles other than

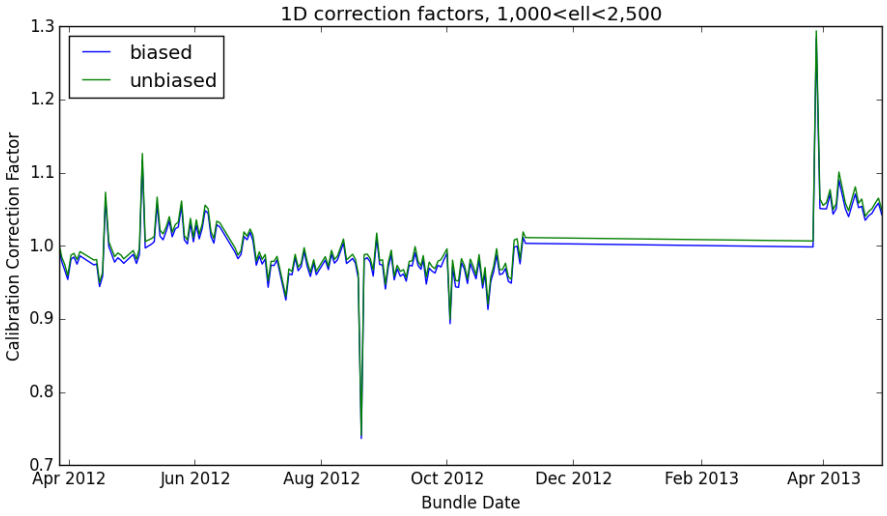

Figure 4.2: The correction factors for the 150 GHz bundles using the primary CMB anisotropies as the calibration source. The effect of crossing a bundle i against the coadd of every bundle (biased) and the coadd of every bundle except bundle i (unbiased) are shown.

bundle i, C_{tot-i}, can be computed,

$$\frac{b_i * C_{tot-i}}{C_A * C_B}. \tag{4.1}$$

Where C_A and C_B are each coadds of a randomized half of the bundles and are used to normalize the cross spectra. We use C_{tot-i} to cross each bundle against instead of a coadd of every bundle to avoid the noise bias introduced when crossing a bundle with itself, Figure 4.2 shows the effect of the noise bias that would be incurred and the correction factor. By averaging the one dimensional cross spectra between multipoles where the CMB dominates, here we used $1,000 < l < 2,500$, a single correction factor for each bundle is computed. Computed correction factors are shown in Figure 4.2 and the effect of the corrections factors on known sources is shown in Figure 4.1.

Correction factors were only computed for the 150 GHz bundles as the 90 GHz bundles did not exhibit any amplitude outliers.

4.1.2 Point Source Filtering

During map creation a number of filtering choices were made to reduce large scale power in the scan direction of the maps (see Section 3.3 for more details on this scan filtering). While this scan filtering removes a lot of the large scale atmospheric contributions to the maps, there are still a lot of CMB fluctuations and noise in the maps that are spatially larger than potential transient sources. To get the highest signal-to-noise on transient sources we can spatially filter the map bundles with an optimal filter that is specific to the points sources we are looking for.

The equation for constructing an optimal filter for two dimensions in Fourier-space is described in [22], [44] and is reproduced below,

$$\psi(k_x, k_y) \equiv \frac{\tau(k_x, k_y) N^{-1}(k_x, k_y)}{\int \tau^2(k_x, k_y) N^{-1}(k_x, k_y) \mathrm{d}k_x \mathrm{d}k_y}. \tag{4.2}$$

Where $N(k_x, k_y)$ is map noise in Fourier-Space and $\tau(k_x, k_y)$ is the Fourier-space representation of the desired source profile $S(k_x, k_y)$, convolved with the instrument beam $B(k_x, k_y)$, and scan filtering transfer function $F(k_x, k_y)$.

$$\tau(k_x, k_y) = S(k_x, k_y) * B(k_x, k_y) * F(k_x, k_y) \tag{4.3}$$

For this analysis the desired sources are point sources (two dimensional delta functions), once convolved by the beam, point sources will look like the beam.

$$\tau_{ps}(k_x, k_y) = B(k_x, k_y) * F(k_x, k_y) \tag{4.4}$$

For this analysis we assume the beams are Gaussian with full widths at half max (FWHM) of 1.8 arcmin at 90 GHz and 1.1 armcin at 150 GHz. For the production of the optimal filter the differences between the actual beams and Gaussian beams makes little difference. The

N in equation 4.2 is the Fourier-space noise covariance. The noise covariance will include pixel noise in the map, N_{pix}, and power from any unwanted sky signal, $P_{unwanted}$, convolved with the beam and scan filtering. The CMB is considered unwanted sky signal for transient analyses.

$$N = \sqrt{P_{unwanted} * (F(k_x, k_y) * B(k_x, k_y))^2 + N_{pix}^2} \tag{4.5}$$

The optimal filter knows the shape of the source of interest and will down weight features of the map which are larger or smaller than the given source profile. The optimal filter also down weights modes which are noisier or suppressed by the beam and scan directional filtering.

Independently for 90 and 150 GHz, the average two dimensional fast Fourier transform (FFT) of the bundles was calculated and slightly smoothed with a Gaussian before being used as the Fourier-space pixel noise estimation (N_{pix}) for the optimal filter. Before taking a Fourier transform each bundle is multiplied by the combined border and point source apodization mask (see Section 3.3.7). By applying the apodization mask, we remove the potential of the spatial filtering to cause ringing around bright sources or artifacts around the rough edges of the bundles. A one dimensional version of the average bundle FFT at 90 and 150 GHz can be seen in Figures 4.3 and 4.4 and was produced for debugging purposes only. The actual smoothed two dimensional FFT averages used for the pixel noise in the optimal filter can be seen in Figures 4.5 and 4.6.

The full two dimensional optimal filter for 90 and 150 GHz can be seen in Figure 4.8 and Figure 4.9. Azimuthally averaged versions of both optimal filters are overplotted in Figure 4.7. The effects of the different sized beams at 90 and 150 GHz can clearly be seen as moving the peak in the filter out to higher multipoles for 150 GHz.

The optimal filter is multiplied by the bundle maps in Fourier-space and then the filtered bundles are transformed back into real space. Each pixel value of the filtered bundles in real space represents the amplitude of fitting the source profile centered on that pixel.

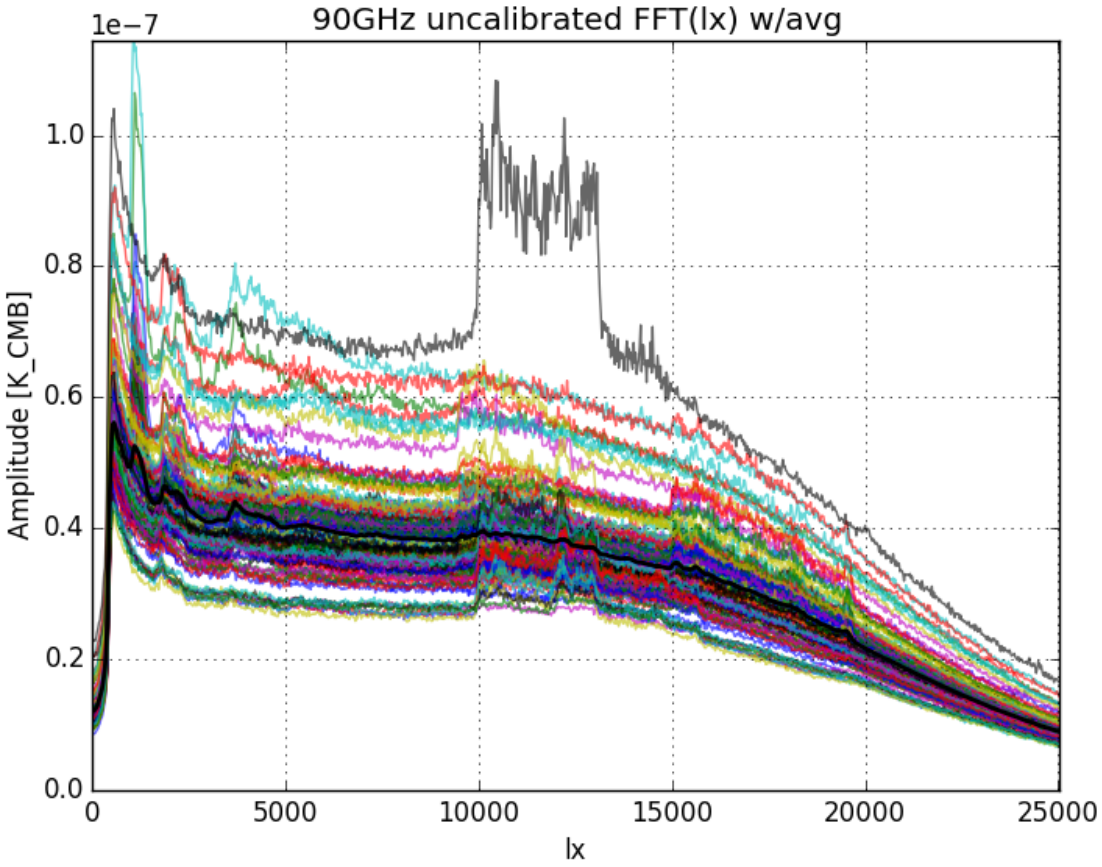

Figure 4.3: The FFTs of every 90 GHz bundle averaged in k_y are over-plotted with thin lines. The thick black line is the average FFT for all the bundles, a two dimensional version of this trace is used as the noise source for the optimal filter. The effects of the low pass filter in the scan direction (k_x) at 20,000 can easily be seen in this plot. There are noticeable outliers in this plot that exhibit non-standard FFT features. Since the 90 GHz data is only used to confirm sources seen in the 150 GHz bundles the outliers at 90 GHz do not create a bias or trigger false detections.

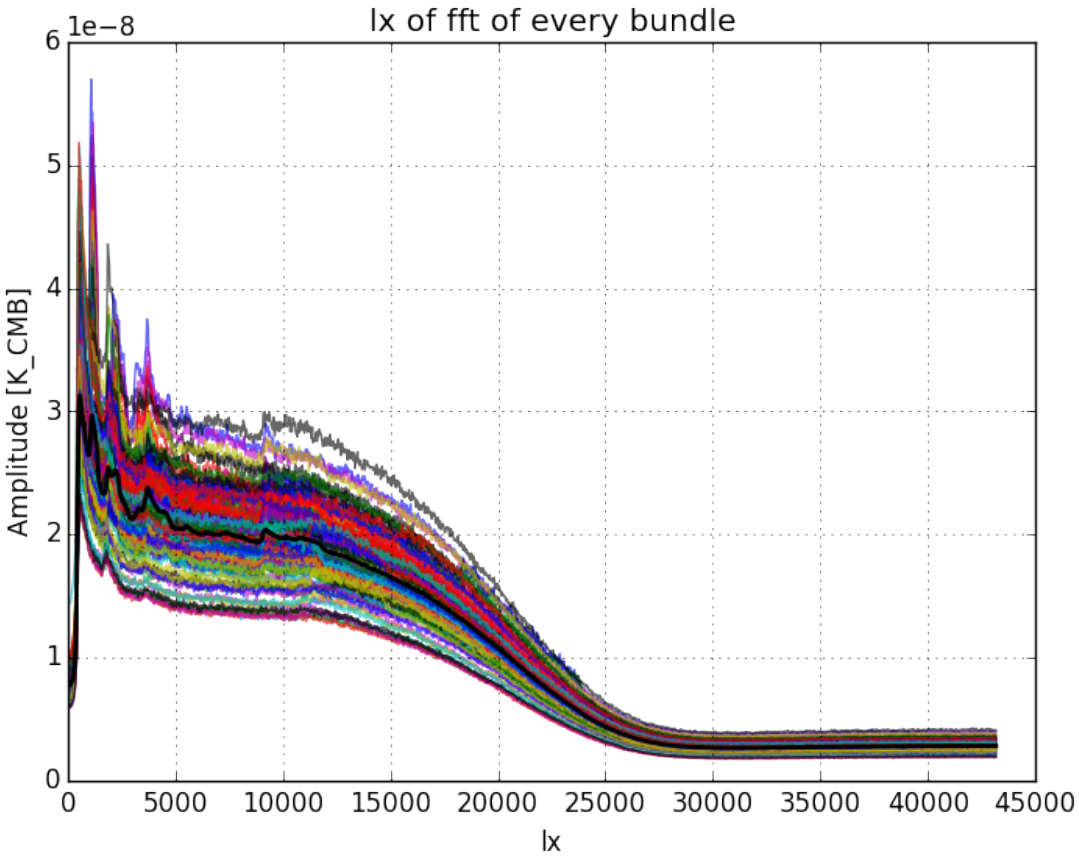

Figure 4.4: The FFTs of every 150 GHz bundle averaged in k_y are overplotted with thin lines. The thick black line is the average FFT for all the bundles, a two dimensional version of this trace is used as the noise source for the optimal filter. The effects of the low pass filter in the scan direction (k_x) at 20,000 can easily be seen in this plot.

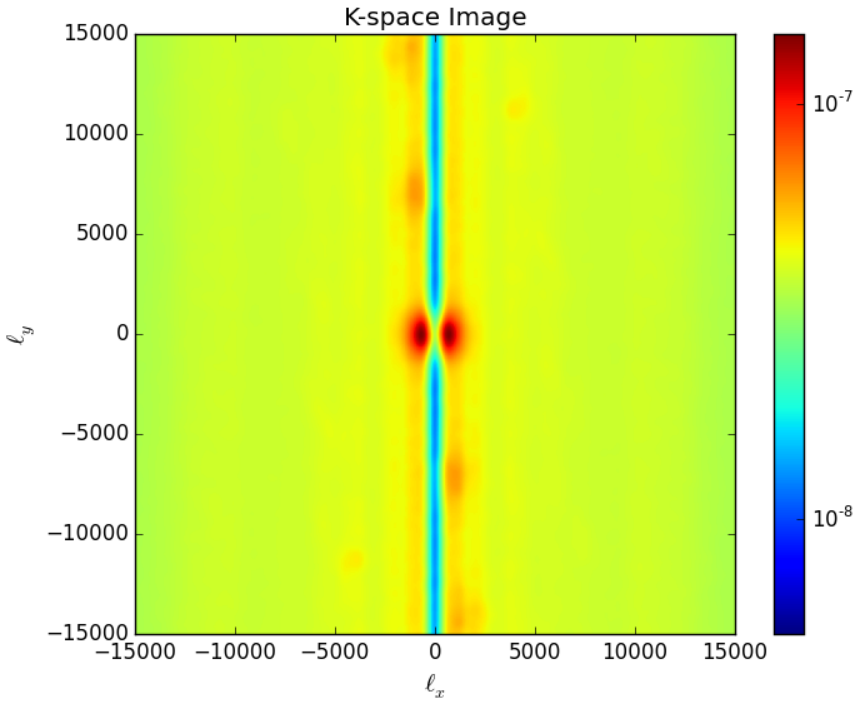

Figure 4.5: A slightly smoothed version of the average FFT for the 90 GHz bundles is shown in two dimensions. This is the noise estimation used to construct the optimal filter at 90 GHz. The color scale shown is in log.

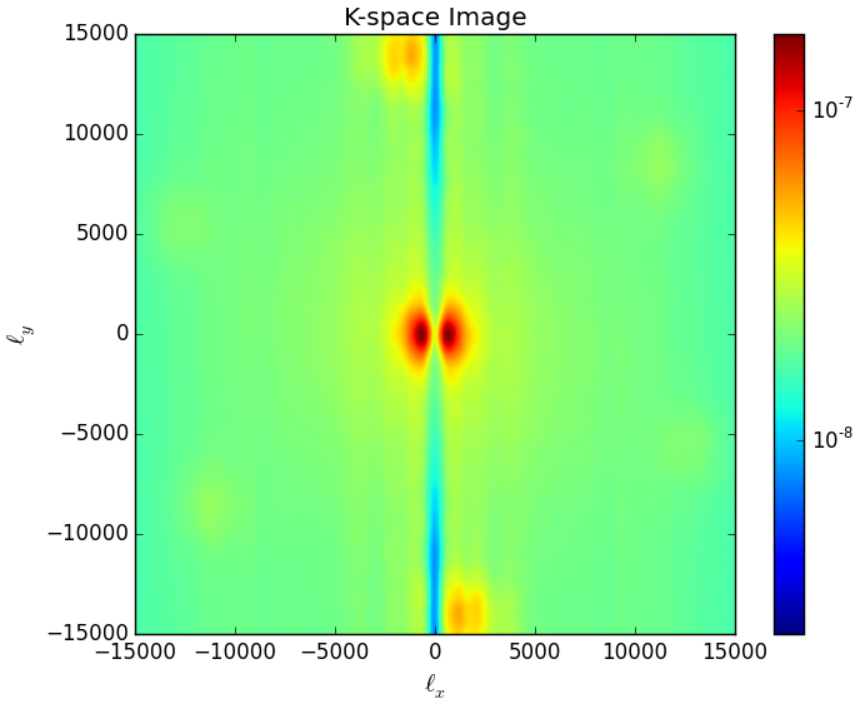

Figure 4.6: The average FFT for the 150 GHz bundles is shown in two dimensions. This was the noise estimation used to construct the optimal filter at 150 GHz. The color scale shown is in log.

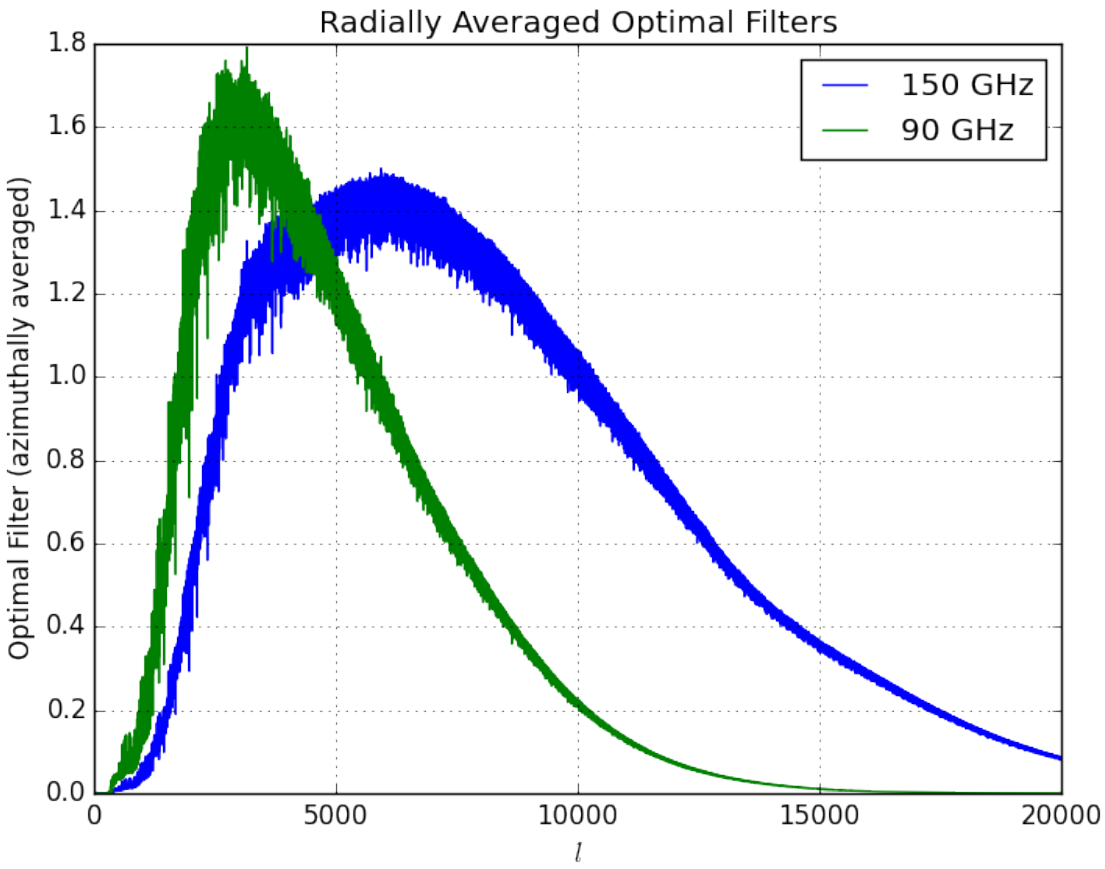

Figure 4.7: Azimuthally averaged one dimensional optimal filters for 90 and 150 GHz. The effect due to the different sized beams (FWHM of 1.8 armcin at 90 GHz and 1.1 arcmin at 150 GHz) can clearly be seen as moving the peak in the filter out to higher multipoles for 150 GHz.

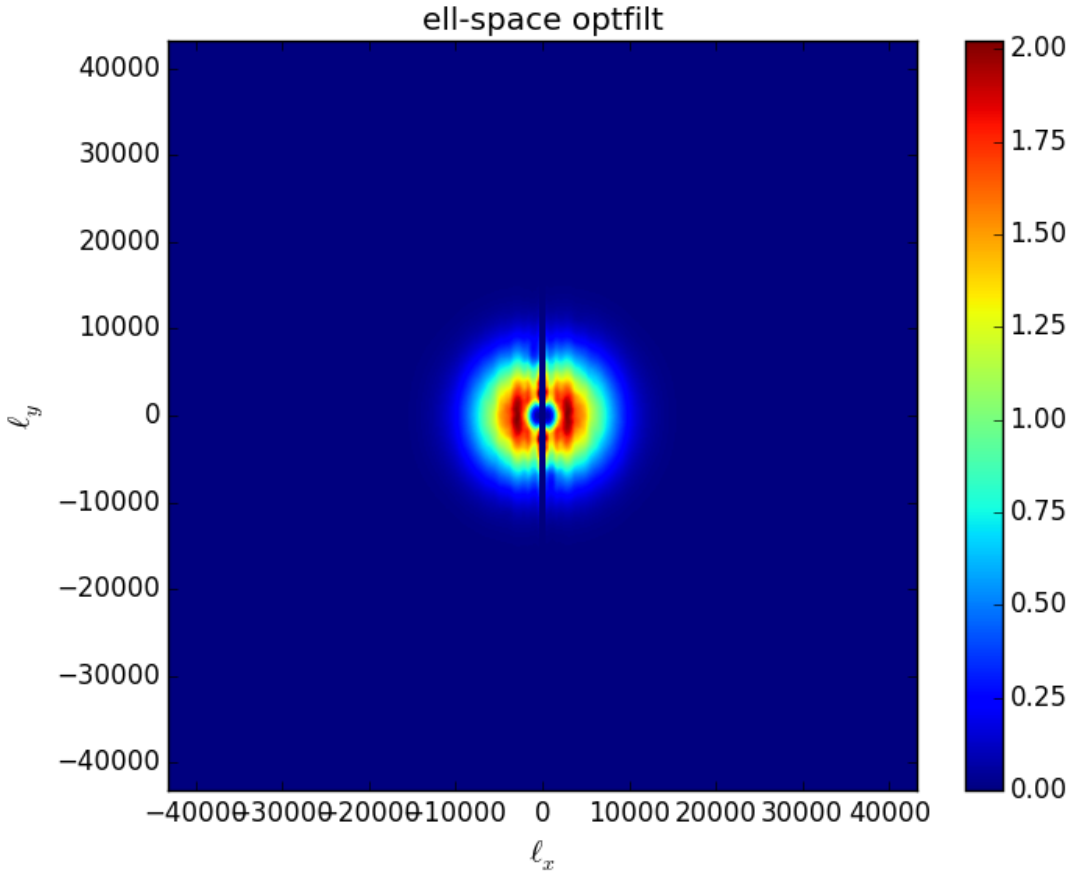

Figure 4.8: The two dimensional optimal filter at 90 GHz used for this transient source analysis.

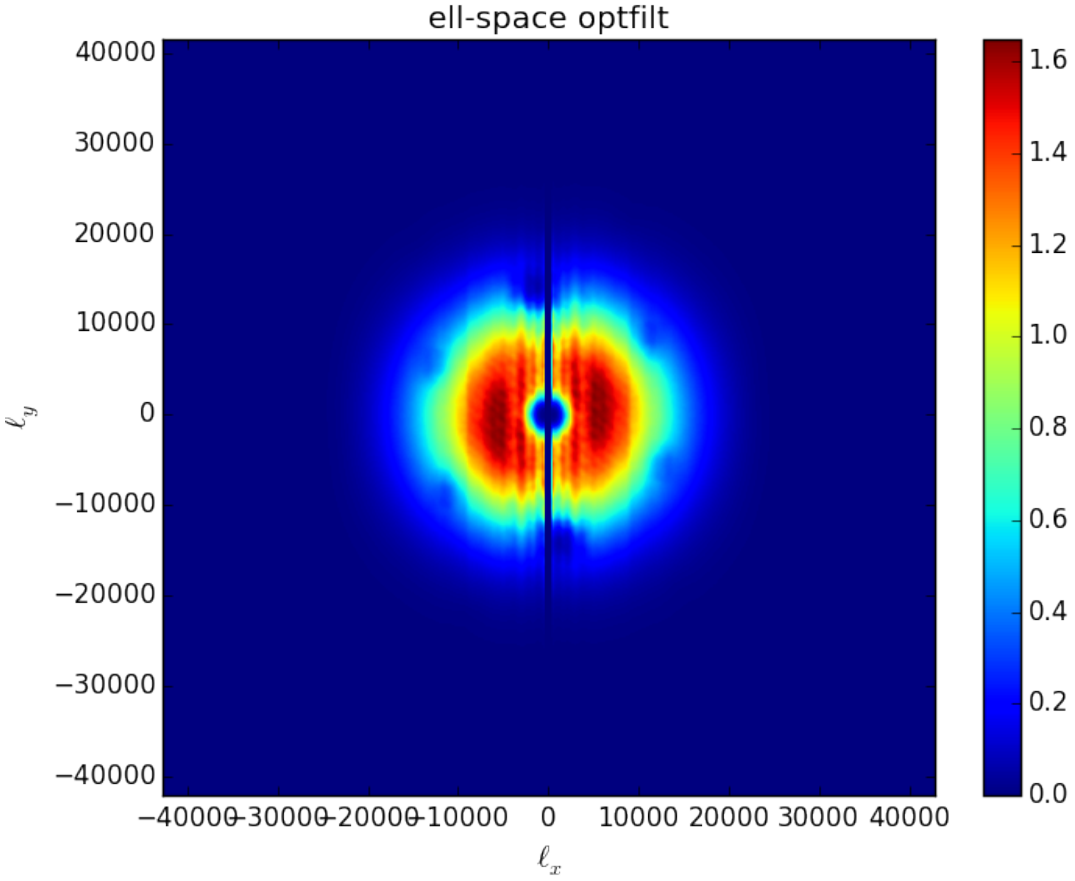

Figure 4.9: The two dimensional optimal filter at 90 GHz used for this analysis.

4.1.3 Conversion to mJy

Standard SPTpol CMB maps are made in units of equivalent fluctuations of the CMB, K_{CMB}, see Section 3.3.1 for information on this. A more useful unit of measure for sky sources is a Jansky, or milli-Jansky (mJy), which is a measure of flux with units of $\mathrm{W/m^2srHz}$. The conversion from K_{CMB} to mJy for SPTpol is given in [44], but is also outlined here.

Different astronomical populations follow a variety of power law trends in frequency, so the spectral bandpass for 90 and 150 GHz detectors must be included in the conversion calculation. The bandpasses for 90 and 150 GHz are shown in Figure 2.10, note there was a small shift in bandpasses between 2012 and 2013 for both the 90 and 150 GHz detectors.

Using the bandpasses, we can calculate a band center for each detector band, ν_o, with

$$\nu_o = \frac{\int \nu f(\nu) d\nu}{\int f(\nu) d\nu} \tag{4.6}$$

where $f(\nu)$ is the transmission spectra shown in Figure 2.10 and the denominator is the effective bandwidth which is shown in Table 4.1. The transmission spectra shown include the etendue of the telescope, this will become useful in Equation 4.9.

SPTpol Average Band Properties

Band	Year	Bandcenter ν_o, [GHz]	Bandwidth $\Delta\nu$ [GHz]
90 GHz	2012	90.9	28.9
	2013	93.0	32.4
150 GHz	2012	145.8	44.4
	2013	146.4	42.5

Table 4.1: SPTpol Average Band Properties
The array averaged band centers and bandwidths for 90 and 150 GHz are shown. The data used for these calculations are the FTS data shown in Figure 2.10. The metal mesh low pass filters for both 90 and 150 GHz were replaced between the 2012 and 2013 observing seasons.

The conversion between K_{CMB} and mJy is a conversion between a blackbody spectrum (the CMB) and a power law spectrum (astronomical source) integrated over the detector

bandpass. A power law spectrum is defined as $S(\nu)$ and expressed as a power law with an exponential of α,

$$S(\nu) = S_o \left(\frac{\nu}{\nu_o} \right)^{\alpha}. \tag{4.7}$$

The blackbody spectrum is the partial derivative of the Planck function with respect to temperature,

$$\frac{dB}{dT} = \frac{d}{dT} \left[\frac{2h\nu^3}{c^2} \frac{1}{e^{\frac{h\nu}{kT}} - 1} \right] = \frac{2h^2\nu^4}{kT^2c^2} \frac{e^{\frac{h\nu}{kT}}}{(e^{\frac{h\nu}{kT}} - 1)^2}. \tag{4.8}$$

The blackbody and source spectra equations are plugged into the numerator and denominator of the conversion equation below,

$$C_{\mathrm{KtoJy}} = \frac{\int A\Omega(\nu) \frac{dB}{dT} f(\nu) d\nu}{\int A\Omega(\nu) (\frac{\nu}{\nu_o}) f(\nu) d\nu} \tag{4.9}$$

where $A\Omega(\nu)$ is the etendue (telescope throughput) and becomes ν^2/c^2 for beam filling sources and single moded detectors (as the SPTpol detectors are). The etendue factor is already included in the transmission spectra used here, so it is absorbed into the $f(\nu)$ term. The resulting conversion equation is just the partial derivative of the blackbody over the source spectra, both being integrated over the detector bandpass.

$$C_{\mathrm{KtoJy}} = \frac{\int \frac{dB}{dT} f(\nu) d\nu}{\int \frac{\nu}{\nu_o} f(\nu) d\nu} \tag{4.10}$$

Since the conversion equation (Eq. 4.10) depends on the source spectrum, the exact conversion depends on the type of source. Table 4.2 shows spectral indices for common categories of sources and the associated SPTpol conversion factors associated with them.

For this transient source analysis there is a reasonable expectation of radio sources, so all noise and detection numbers will be given assuming a radio spectral index of $\alpha = -0.5$.

Since the target sources for this analysis are point sources and not extended sources, the conversion factors shown in Table 4.2 must be multiplied by the effective solid angle, Ω_b. In

SPTpol Conversion Factors

	Conversion Factor $[MJy/sr/K_{\rm CMB}]$			
	90 GHz		150 GHz	
Source Type	2012	2013	2012	2013
Radio, $\alpha = -0.5$	195.9	200.1	382.3	384.0
Rayleigh-Jeans, $\alpha = 2$	203.1	210.6	379.9	381.5
Dusty, $\alpha = 3.5$	195.9	200.1	367.3	368.5

Table 4.2: SPTpol Conversion factors for point sources
The mJy/K conversion factors for 90 and 150 GHz are shown for both 2012 and 2013 for a variety of astronomical sources.

this case the bundle maps have also been optimally filtered, so the effective solid angle is the area under the optimally filtered source profile,

$$\Omega_b = \left[\int \psi(k_x, k_y) \tau k_x, k_y dk_x dk_y \right]^{-1}. \tag{4.11}$$

Where ψ is the optimal filter and τ is the target source profile as discussed in Section 4.1.2. For this analysis and the optimal filters presented in Section 4.1.2 the Ω_b at 90 GHz is 3.383x10^{-7} steradians and at 150 GHzis 1.251x10^{-7} steradians. The final conversion numbers used for the transient analysis presented here are, for 2012 and 2013, 66.3 Jy/K and 67.7 Jy/K for 90 GHz and 47.8 Jy/K and 48.0 Jy/K for 150 GHz.

4.2 Transient Data Set

The data included in this analysis were taken with the SPTpol camera between March of 2012 and April of 2013. All included data are from the same 100 deg^2 field discussed in section 3.1 and shown in Figure 3.1. No observations of the 100 deg^2 field were taken between November 2012 and March 2013 because the field was contaminated by the Sun and the SPTpol camera was being upgraded and calibrated.

An average of 32 individual observations are added together to form a map bundle, the exact distribution of observations per map bundle are shown in Figure 4.10. The number

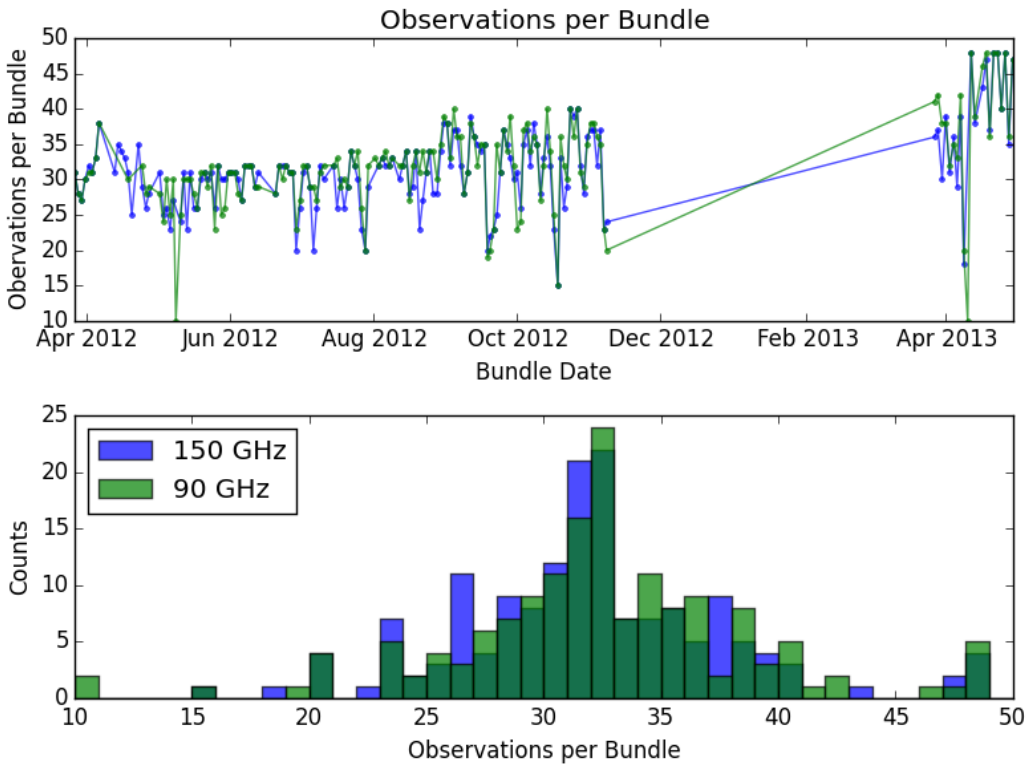

Figure 4.10: The number of observation in each bundle are plotted against the bundle date for 90 and 150 GHz bundles. Each lead or trail observation are counted individually and bundles with less than 10 observations were eliminated from this analysis. The average number of observations per bundle at 90 GHz is 32 and at 150 GHz is 31.5.

of observations per map bundle is not constant because the bundle boundaries are decided by cryostat fridge recycling points (see Section 4.1 for bundling specifics). The number of observations in a bundle is highly correlated with the noise level of that bundle, Figure 4.12. There are 161 total 150 GHz map bundles with 141 bundles comprised of observations from 2012 and 20 bundles containing observations from 2013. At 90 GHz there are 157 total map bundles with 137 bundles made from observations in 2012 and 20 bundles containing observations from 2013. The average RMS of a bundle at 150 GHz is 7.4 mJy and at 90 GHz is 12.8 mJy.

For the specifics of map making and low level data processing refer to Sections 3.3.

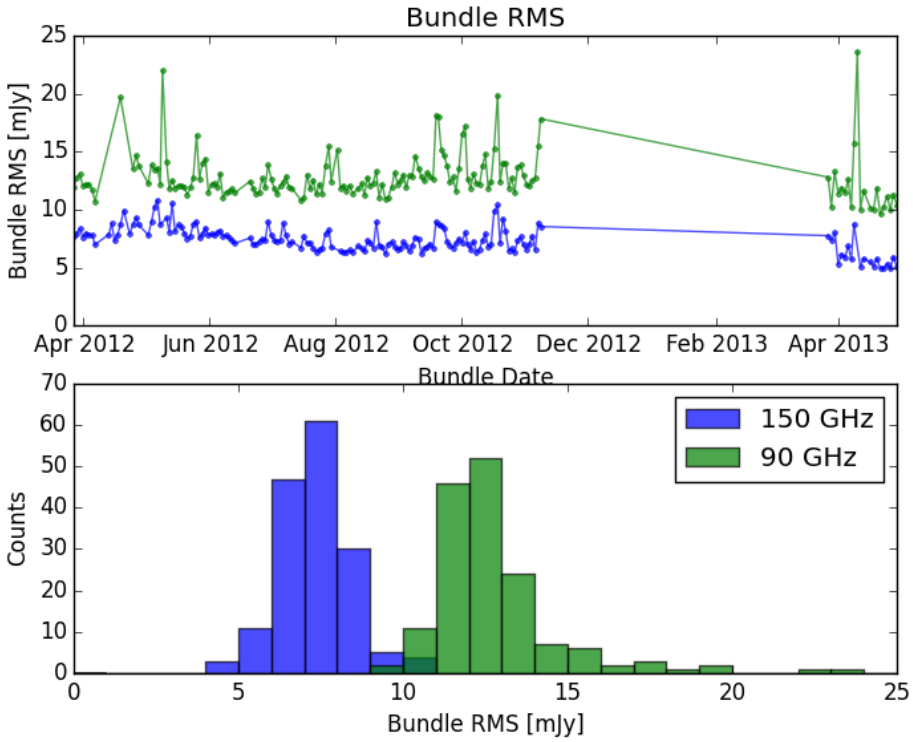

Figure 4.11: The bundle RMS is plotted against the bundle date for 90 and 150 GHz bundles. The average bundle RMS at 90 GHz is 12.8 mJy and at 150 GHz is 7.4 mJy. Bundle RMS is highly correlated with the number of observation in a bundle, as shown in Figure 4.12.

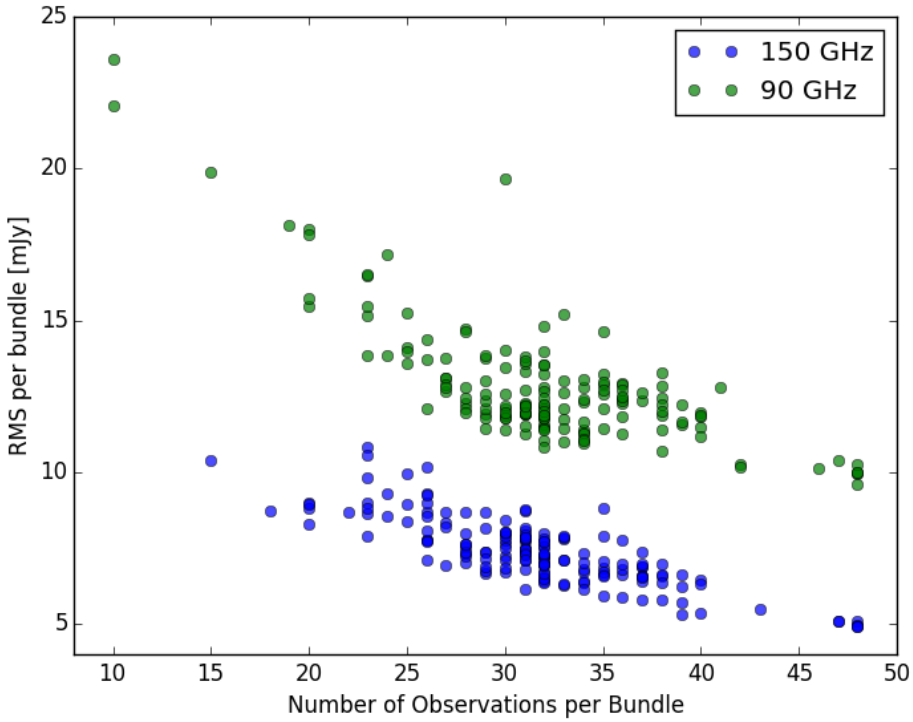

Figure 4.12: The bundle RMS is plotted against the number of observations in a bundle for both 90 and 150 GHz bundles. Each lead or trail field counts as a single observation. Bundles with less than 10 observations suffered from poor coverage and were cut from this analysis.

4.3 Time Profile Fitting

Since we are searching for transient sources we will look for sources in the time-domain instead of the spatial-domain as used for prior point source searches in SPT data. By fitting in the time-domain the total bright time of the transient source is used in the fit instead of just a snapshot of the transient bright time that is contained in an single map bundle. Choosing an appropriate time-profile for transient fitting in the time-domain can be complicated when many different source populations are involved.

Independent of transient population type, all transient sources have a rise and fall in brightness as a function of time. The amplitude of the brightness increase and the exact time profile will vary with transient population, but the general rise and fall of the profile will remain. For this analysis the time profile used to identify transient sources will be a Gaussian profile[1],

$$S_{gaus}(t, A, t_o, w) = \frac{A}{w\sqrt{2\pi}} \mathrm{e}^{\frac{-(t-t_o)^2}{2w^2}} \tag{4.12}$$

Where A is the amplitude, t is the bundle time with t_o as the time corresponding to the peak of the Gaussian, and w is the width of the Gaussian in time. Not all transient sources are well matched to a Gaussian profile, notably GRBs exhibit an asymmetric time profile in gamma-rays with short rise times and longer decays [35]. In Section 4.3.2 we discuss how the Gaussian time profile used here is able to recover more complex source profiles with only a marginal decrease in efficiency [5].

It is helpful to view the entire map bundle data set as a data cube with map bundles stacked chronologically along the z-axis, or time-axis. With the data cube in mind, if a

1. Because the pixel streams being fit are mean subtracted the Gaussian profile used should also be mean subtracted. However, using a mean subtracted Gaussian profile for the model creates sharp features in the parameter space resulting in poor minimizer behavior. Not using a mean subtracted Gaussian as the model will create less accurate fits as the width and amplitude of the Gaussian are increased. Because we are primarily looking for transient that from days to weeks the difference between using mean subtracted model and a non-mean subtracted model are small. In Section 4.3.1 the width penalty is calculated using a mean subtracted model and the effect of doing so is discussed.

single map pixel is traced through the time axis a timeline for that pixel, or sky position, is created. This timeline is the light-curve of that pixel and will be referred to as a "pixel stream".

Each pixel stream is mean subtracted and independently fit to the Gaussian time profile in Equation 4.12. The best Gaussian fit for a pixel stream can be computed by minimizing the χ^2 function

$$\chi^2_{pix}(A, t_o, w) = \sum_{i=0}^{N} \frac{(S_{pix}(t_i) - S_{gaus}(t_i, A, t_o, w))^2}{\sigma(t_i)^2}, \tag{4.13}$$

where $S_{pix}(t)$ is a specific pixel stream, $\sigma(t)$ is the error on the pixel stream values, and S_{gaus} is the Gaussian time profile (Equation 4.12). Minimizing χ^2_{pix} is an equivalent action to maximizing the likelihood L_{pix},

$$L_{pix}(A, t_o, w) = e^{\frac{-\chi^2_{pix}(A,t_o,w)}{2}}. \tag{4.14}$$

The maximization of L_{pix} will have a statistical preference for fits to short duration Gaussians (small w values) owing to the larger number of potential independent short duration Gaussians in a pixel stream compared to long duration Gaussians. The short width preference, and a method for correcting it, are discussed in Section 4.3.1. We will create a fit hypothesis, H_{fit}, by appending an exponential factor of $T(w)$ to L_{pix} as a width dependent penalty to correct for the preference for short widths [5].

$$H_{\text{fit}}(A, t_o, w) = L_{\text{pix}}(A, t_o, w) e^{\frac{-T(w)}{2}} = e^{\frac{-\chi^2_{\text{pix}}(A,t_o,w)}{2}} e^{\frac{-T_{\text{fit}}(w)}{2}} \tag{4.15}$$

The fit width penalty was introduced in an exponential form to simplify a rewritten version

of Equation 4.15 that will become useful later,

$$-2ln(H_{\rm fit}(A,t_o,w)) = \chi^2_{\rm pix}(A,t_o,w) + T_{\rm fit}(w). \tag{4.16}$$

By maximizing the fit hypothesis (Equation 4.15), we find the best fit Gaussian time profile for every pixel stream. To calculate the significance of the Gaussian fit, we compare the fit hypothesis to a null hypothesis, $H_{\rm null}$,

$$P = \frac{H_{\rm fit}(A,t_o,w)}{H_{\rm null}(A=0,t_o,w)} = \frac{e^{\frac{-\chi^2_{\rm pix}(A,t_o,w)}{2}} e^{\frac{T_{\rm fit}(w)}{2}}}{e^{\frac{-\chi^2_{\rm pix}(A=0,t_o,w)}{2}} e^{\frac{T_{\rm null}(w)}{2}}}. \tag{4.17}$$

The null hypothesis is the same as the fit hypothesis but with a Gaussian profile that has a fixed amplitude of exactly zero. Since the Gaussian of the fit hypothesis effectively has no width dependence, the null hypothesis penalty factor is free to choose the width that minimizes the penalty.

$$H_{\rm null} = L_{\rm pix}(A=0,t_o,w)e^{\frac{T_{\rm null}(w)}{2}} = e^{\frac{T_{\rm null}(w)}{2}} \sum_{i=0}^{N} \frac{(S_{pix}(t_i) - S_{gaus}(t_i, A=0, t_o, w))^2}{\sigma(t_i)^2} \tag{4.18}$$

$$H_{\rm null} = e^{\frac{T_{\rm null}(w)}{2}} \sum_{i=0}^{N} \frac{(S_{pix}(t_i))^2}{\sigma(t_i)^2}. \tag{4.19}$$

Equation 4.17 can get massaged into a more useful equation,

$$-2ln(P) = \chi^2_{\rm pix}(A,t_o,w) + T_{\rm fit}(w) - \chi^2_{\rm pix}(A=0,t_o,w) - T_{\rm null}(w). \tag{4.20}$$

Here $-2ln(P)$ is referred to as the "test statistic". Higher values of the test statistic correspond to Gaussian fits that are less likely to be explained by noise, or are more significant.

The test statistic maximization is applied to pixel streams from the 150 GHz map bundles and the results are discussed in Section 4.4. The maximization is not applied to the 90 GHz

pixel streams, the 90 GHz bundles are only used to confirm potential sources detected in the 150 GHz bundles.

4.3.1 Width Penalty

As mentioned in Section 4.3, the χ^2 minimization of Equation 4.13 has a statistical preference for short width Gaussian fits. We can compute the preference by replacing S_{pix} in Equation 4.13 by S_{noise}, a simulated pixel stream of only Gaussian noise, and calculating the test statistic for different fixed width values (4.13),

$$-2ln(P) = \chi^2_{\text{noise}}(A, t_o, w = w_{\text{fixed}}) - \chi^2_{\text{noise}}(A = 0, t_o, w). \tag{4.21}$$

The test statistic calculated here is free from a width penalty term since that is what we are currently calculating. The model profile used here to calculate the test statistic is not the S_{gauss} of Equation 4.12 but a mean subtracted version, S'_{gauss},

$$S'_{gaus}(t, A, t_o, w) = S_{gaus}(t, A, t_o, w) - \overline{S}_{gaus}(t, A, t_o, w). \tag{4.22}$$

As discussed earlier, the mean subtracted Gaussian model should be used for all fitting done in this analysis to match the data, but this creates issues with the minimization. To compute the width penalty we use a mean subtracted Gaussian model and show the effect of using this penalty with a fitter that has a non-mean subtracted model in Figure 4.17.

The histograms of test statistics in Figure 4.13 shift to higher significance values as the fixed widths become shorter. The shift is caused by the number of effective search space size increasing as the number of independent Gaussians that can fit within a pixel stream of fixed length increases[2]. The amount of shift a histogram experiences is quantified by the

2. The Gaussians mentioned are not truly independent due to the asymptotic tails of Gaussians, but are effectively independent once amplitude of the Gaussian tail drops well below the noise level.

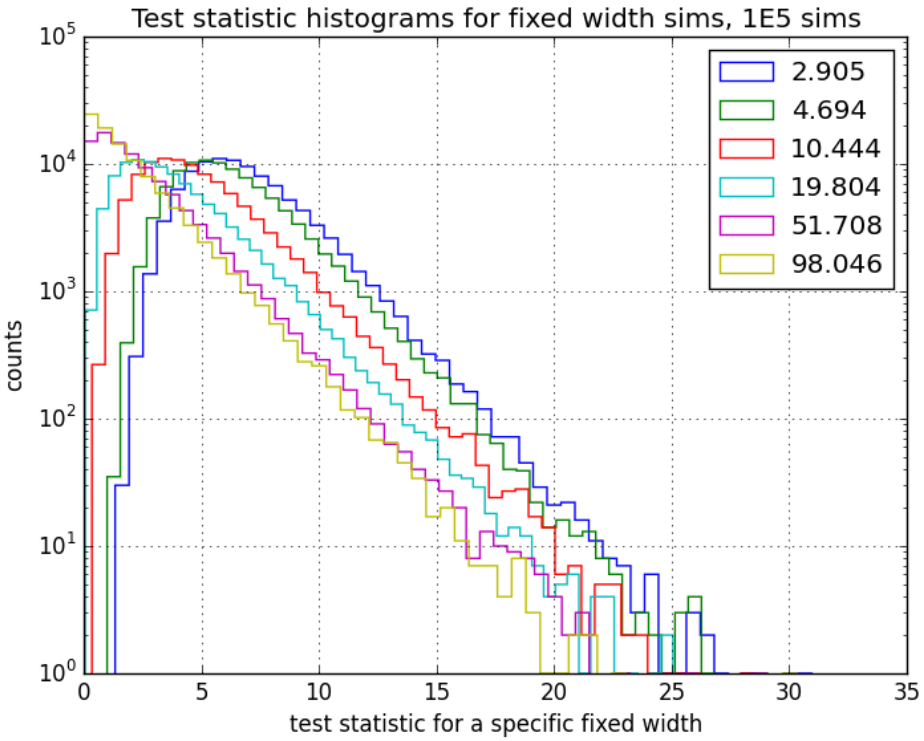

Figure 4.13: Unfilled histograms of calculated likelihoods for fits with fixed widths to simulated noise only pixel streams. The simulated pixel streams are Gaussian noise realizations that have the same length, errors, and time separations as the 150 GHz bundles. During the fitting process the Gaussian width was held fixed and the center time of the Gaussian and amplitude were allowed to vary. Each histogram shows results from fitting the same simulated noise pixel streams with a different fixed width. The shift in distributions show the effective number search space size for the fits get larger as the Gaussian width gets shorter. The test statistics shown here were calculated with the mean subtracted Gaussian profile of Equation 4.22.

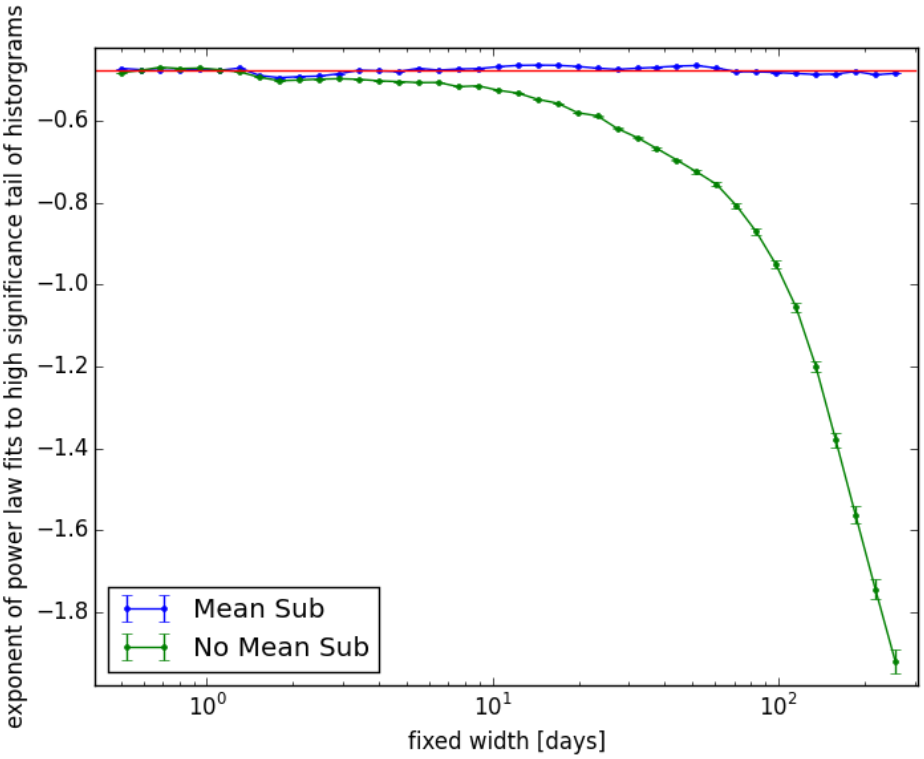

Figure 4.14: The fit exponents from power law fits to the high significance tails of the test statistic histograms of Figure 4.13 are in blue. The red line indicates the average fit exponent and has a value of 0.476. The green points are the same as the blue but are calculated for a Gaussian model without mean subtraction. The change in values of the green points indicate that changing the width of Gaussians in a non mean subtracted model adjusts the test statistic in a more complex than simply changing the effective degrees of freedom.

x-intercept of a power law fit to the the high significance tail of the histogram. The power of the fits to the most significant 10% of fixed width histograms are shown in Figure 4.14. Because the scatter on the fit powers is small the average value is computed and used to refit the high significance tails of the test statistic histograms, the x-intercept of the fixed power fits are shown in Figure 4.15. The x-intercepts of the power law fits are used as the width dependent penalty factor ($T(w)$) to correct for the short width preference (Equation 4.16). The width penalty factor shifts the histograms in Figure 4.13 such that all of the high significance tails lie on top of one another.

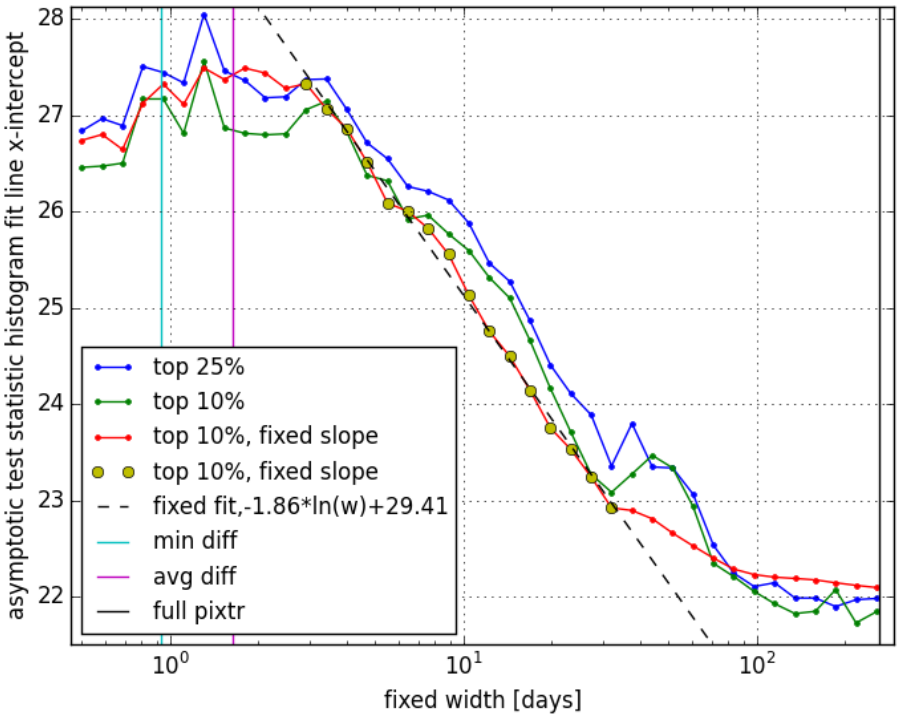

Figure 4.15: This plot will be remade with less lines for less confusion. The x-intercepts of power law fits to 4.13 using the average power from Figure 4.14. The blue points were calculated using the mean subtracted Gaussian profile of Equation 4.22.The larger yellow points show the log-normal region the width penalty was calculated over (2.9 days to 32 days). The dashed line shows the best fit width penalty calculated from the mean subtracted Gaussian profile points.

The width penalty factor is calculated between Gaussian widths of 2.9 to 32 days where the x-intercepts are well fit by a power law and is,

$$T_{\text{fit}}(w) - T_{\text{null}}(w) = -1.86 * ln(\frac{w}{\Delta t}). \tag{4.23}$$

Where Δt is the width value that minimizes the null width penalty and is the total time span between the first and last map bundles. This width penalty was calculated using the mean subtracted Gaussian profile of Equation 4.22. The analytic form for the width penalty is derived in [5] and is the same as Equation 4.23 but with a -2 pre-factor instead of -1.86.

Figure 4.17 shows the difference between applying the width penalty calculated above to a fitter that uses a mean subtracted Gaussian profile and a fitter that uses a non-mean subtracted Gaussian profile. Using the width penalty with a fitter profile that is not mean subtracted decreases the short width preference but does not eliminate it completely. This will make the resulting fits sub-optimal and cause the fitter to potentially miss short width Gaussians with low signal-to-noise. The sub-optimal event finding created by using a non-mean subtracted Gaussian model is less of a problem than the minimization issues introduced by using a mean subtracted Gaussian model.

4.3.2 Time Fitting Verification

To test the analysis code and method discussed in Section 4.3 simulated pixel streams with injected profiles of likely transient sources were created and then fit with the method described. Figure 4.18 shows how well the injected sources were recovered. Even though the Gaussian profile used for fitting is not a perfect match to the profile expected for a GRB radio afterglow, the Gaussian fitter is still able to recover gamma profiles with minimal loss in sensitivity.

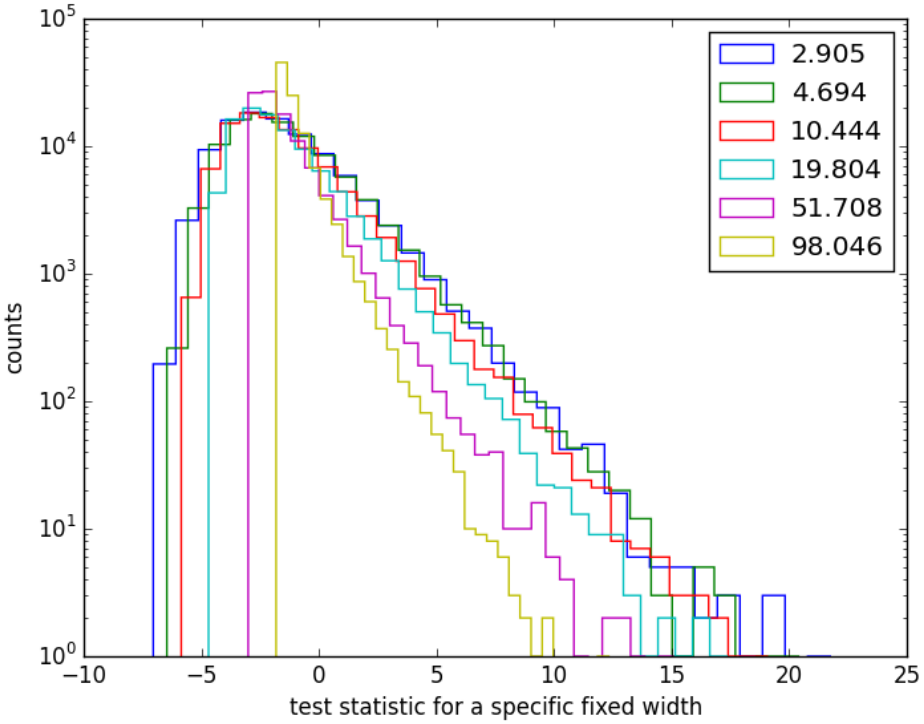

Figure 4.16: Test statistic histograms for simulated noise only pixel streams fits with the calculated penalty applied. The Gaussian model for the histograms shown was not mean subtracted. Most of the width preference for short widths has been eliminated, as shown by the significant regions of the histograms overlapping.

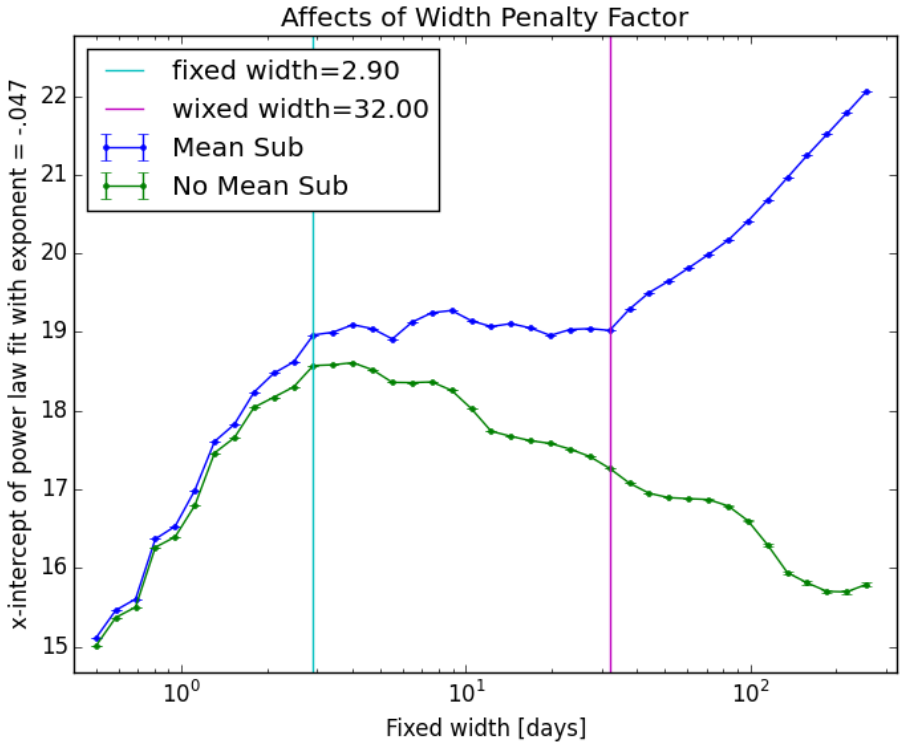

Figure 4.17: The x-intercepts of Figure 4.15 are recomputed after applying the penalty factor in Equation 4.23. The difference between applying the width penalty (that was calculated using a mean subtracted Gaussian profile) to a mean Gaussian subtracted profile fitter and a fitter that using a Gaussian profile without the mean subtracted are shown as the difference between blue and green, respectively. The green points are a super-set of the x-intercepts for the histograms shown in Figure 4.16.

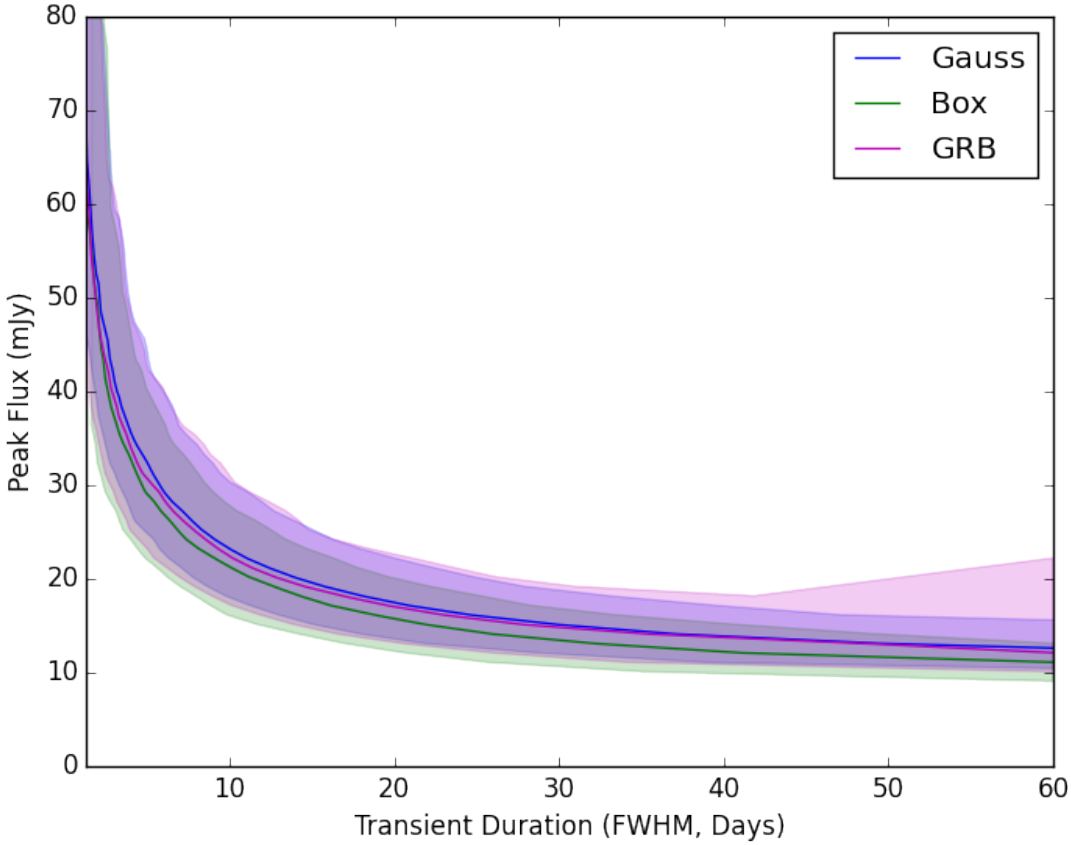

Figure 4.18: Simulated pixel streams were created with the same noise levels and time spacing as the 150 GHz pixel streams. A variety of time profiles were used to inject fake transient sources into the simulated pixel streams and the Gaussian profile fitting method described in Section 4.3 was used to attempt to recover the injected signals. The Gaussian profile was able to recover injected sources with a boxcar profile and with a scaled version of the observed profile of GRB030329A at 100 GHz ([45]) with only a small loss in sensitivity compared to injected Gaussian profiles. The solid line represents a 50% recovery, the shaded region represents signals recovered at the 10% level to the 90% level.

4.4 Transient Fit Results

The results from running the fitter from Section 4.3 over every fourth 150 GHz pixel stream are given in Figures 4.19, 4.20, and 4.21. Every fourth pixel stream (every other pixel stream in the x and y directions) was fit instead of all the pixel streams because the map pixels are only 0.25 arcmin and the beam at 150 GHz is 1.1 arcmin. Only pixels with apodization mask (see Section 3.3.7) values of 1 were used in this analysis. This was a conservative choice and makes the active sky area of the transient search 48.5 $\deg^2$. The results in Figure 4.19 are split into two groups, Gaussian best fits with positive amplitudes and Gaussian best fits with negative amplitudes. Figure 4.20 shows the fit values for the Gaussian widths, amplitudes, and central times.

Calculating the significance of high value test statistics cannot be done with the test statistic results alone since there are not sufficient number counts in this region to generate good estimates on event occurrences. Using a lower significance subset of the data that is not believed to contain real events can be used to calibrate a predictor for event occurrence in the high significance region. Because no known astrophysical process is capable of producing negative transients at 150 GHz the test statistics fit with negative amplitudes are used as a measure of noise triggered events. By fitting a χ^2 distribution to the noise triggered events a conversion between test statistic and significance can be made. The χ^2 fit is only performed on test statistics with values above 0.2 and negative Gaussian amplitudes.

Figure 4.22 shows a comparison between the survival fraction of the best fit χ^2 to the test statistics and the survival fraction of the actual test statistics. The relative agreement of the survival fractions indicates the χ^2 fit to the test statistics can be used to calculate significance in the low event region.

Two clear higher significance outliers can be seen in the test statistics of Figure 4.19, one with a positive amplitude and one with a negative amplitude. Using the χ^2 fit to the negative amplitude events as an estimator, the p-value for the two outliers are 0.080% and

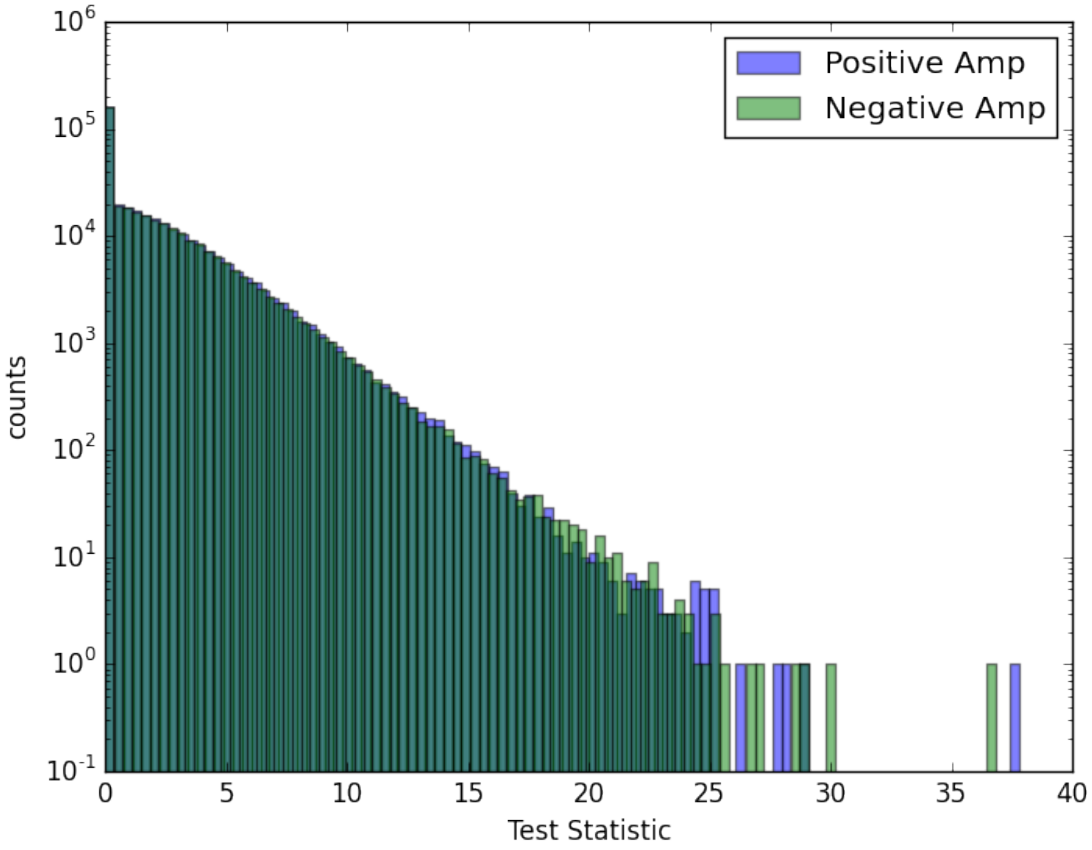

Figure 4.19: The result of fitting a Gaussian profile to every fourth 150 GHz pixel stream as discussed in Section 4.3. The pixel streams that resulted in a best fit Gaussian with a positive amplitude are part of the green histogram. Pixel streams with a negative amplitude best fit Gaussian are counted in the blue histogram and are used as a measure of noise since no decrement transients are thought to exist. The positive and negative amplitude test statistics matching throughout almost all of the distributions indicates that using the negative amplitude fits as a noise model is appropriate.

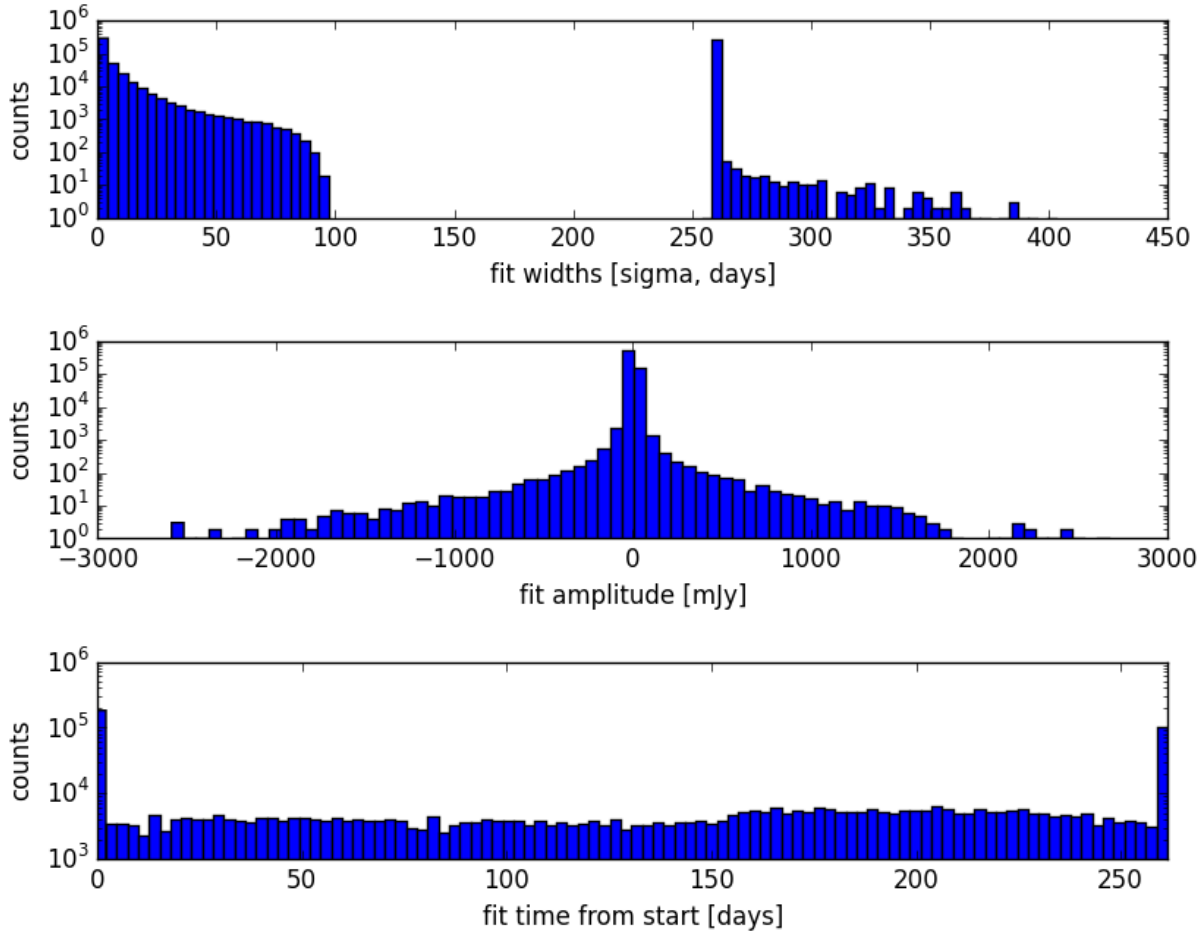

Figure 4.20: The Gaussian best fit parameters from fitting every fourth 150 GHz pixel stream as discussed in Section 4.3. The three panels show different parameters for the same fits. The fits that return widths above 260 days have small test statistic values of less than 0.2. The large width fits are the result of not fitting anything significant at small widths and being pushed by the penalty to large widths where the penalty becomes zero.

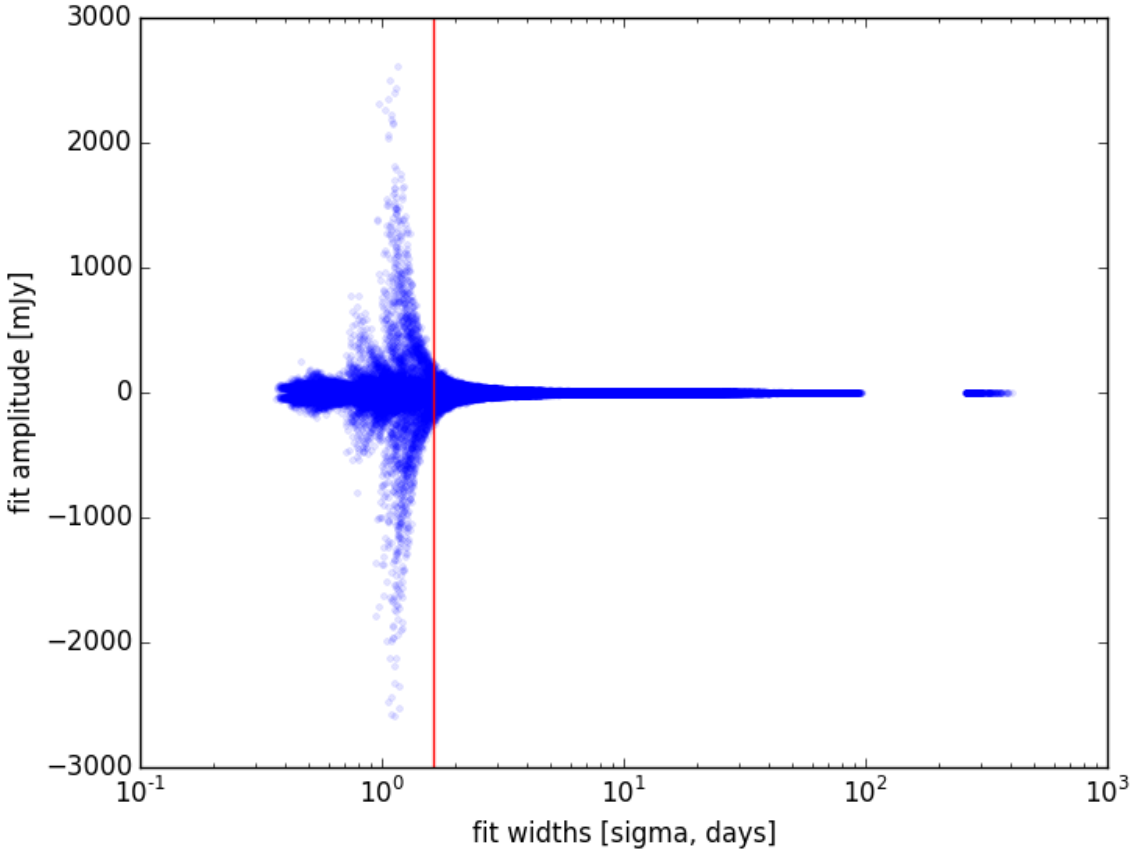

Figure 4.21: The best fit Gaussian amplitude plotted against the best fit Gaussian width. The red line represents the average time separation between map bundles. Large amplitudes fits exist only for fits with small widths.

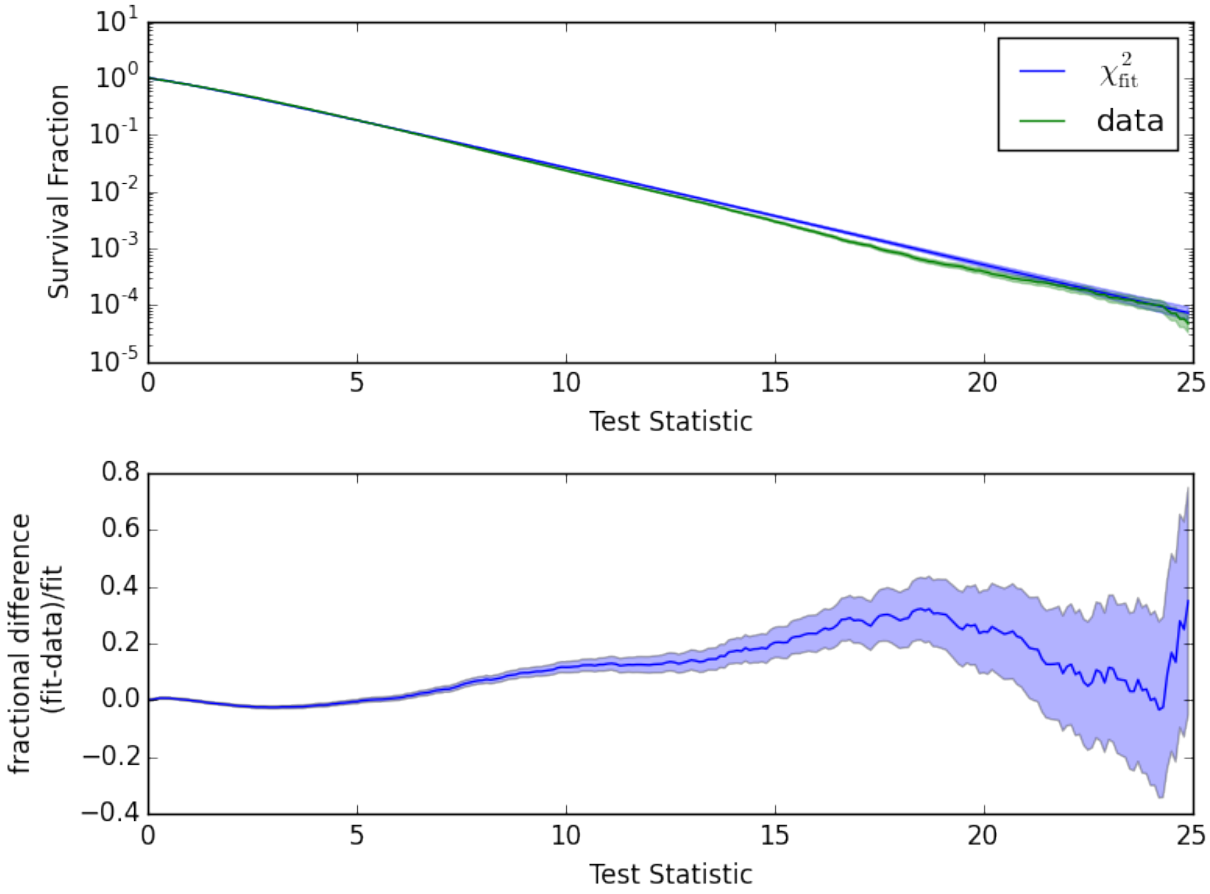

Figure 4.22: (top) In blue the survival fraction as a function of test statistic for the 150 GHz data from Figure 4.19 with test statistics above 0.2 and negative Gaussian fit amplitudes. In green the survival fraction for the best fit χ^2 to the negative amplitude test statistics with widths below 200. (bottom) The fractional difference between the survival fractions shown in the top panel. All shaded regions represent one sigma error bars.

0.097% respectively for the positive and negative amplitude events.

4.5 Highest Significance Sources

The two highest significance outliers seen in the 150 GHz pixel streams have test statistic values of 37.80 and 36.83 and p-values of 0.080% and 0.097%. This section takes a closer look at these two events. The entire pixel streams as well as the Gaussian fits for each of the events are shown in Figure 4.23 and close up views are in Figure 4.24.

The second most significant Gaussian fit has a negative amplitude and a higher p-value at 0.097% than expected for a noise fluctuation. This Gaussian fit has a FWHM of 2.63 days, an amplitude of -45.69 mJy, and is centered on June 3rd, 2012. No known physical process can create a negative amplitude transient as seen with this event. The bottom panel of Figure 4.24 shows a close up of the region of time around the center of the Gaussian fit and includes 90 GHz pixel stream data. The 90 GHz pixel stream data in this region show no sign of an abnormal event. According to the significance quoted here the probability of this even being consistent with a noise fluctuation is 1 in 1031. This means the experiment would have to be ran 1031 times to see a single noise fluctuation similar to the negative amplitude outlier.

The most significant Gaussian fit has a positive amplitude and is consistent with a transient source near the edge of SPTpol sensitivity. This Gaussian fit has a FWHM of 6.25 days, an amplitude of 26.56 mJy, and is centered on April 11th, 2012. A thumbnail image of the bundle closest to the peak of Gaussian peak is shown in Figure 4.25. An X-ray and optical thumbnail composite image taken before April 11th, 2012 is also shown in Figure 4.26. No known public survey has released observations of this region of sky taken after April 11th, 2012.

By only fitting the 150 GHz pixel streams the 90 GHz pixel streams were saved to create an independent confirmation of a potential transient source at a different frequency. For

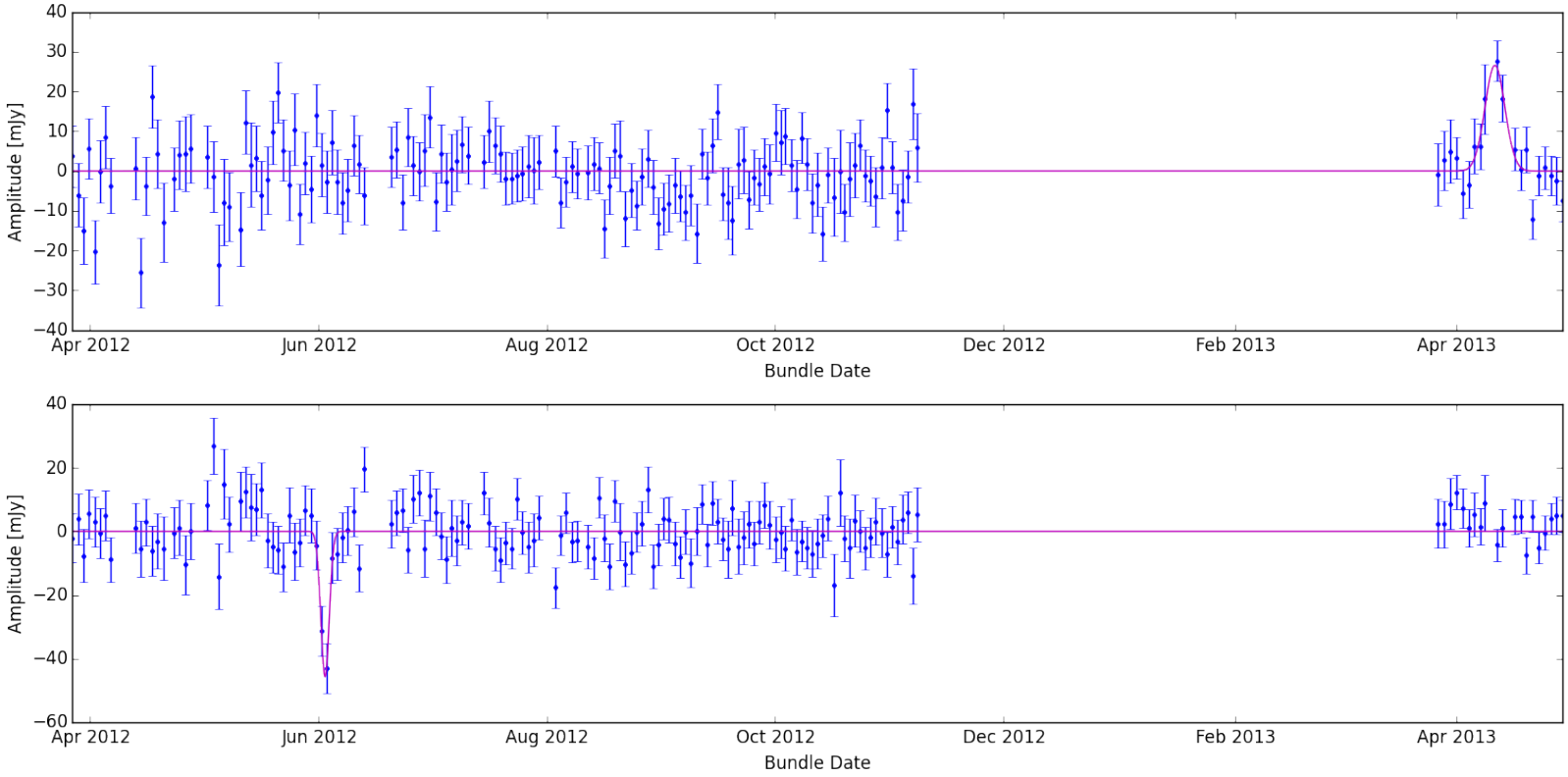

Figure 4.23: The entire pixel streams for the most significant (top) and second most significant (bottom) Gaussian fits. The 150 GHz pixel stream points with error bars are shown in blue and the best fit Gaussian is shown in magenta. The amplitude of the most significant Gaussian fit is 25.67 mJy and has a FWHM of 6.25 days. The amplitude of the second most significant Gaussian fit is -45.69 mJy and has a FWHM of 2.63 days. There is no known physical mechanism for a negative transient event at 150 GHz so the negative amplitude event is assumed to be noise triggered.

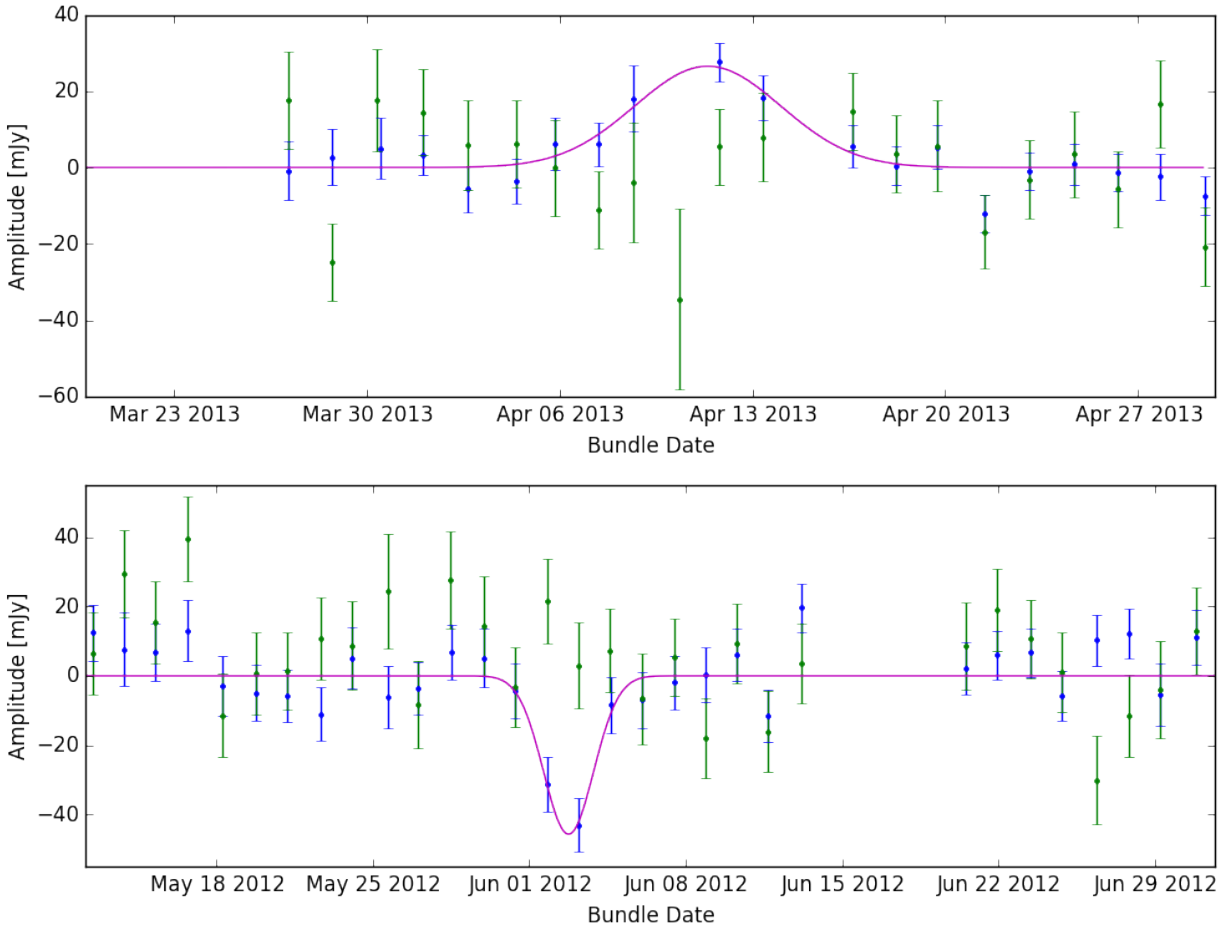

Figure 4.24: A closer look at the regions around the the most significant Gaussian fits. The 150 GHz pixel streams are in blue and the corresponding 90 GHz pixel stream are in green. The magenta line traces the best fit Gaussian to the 150 GHz pixel stream, only the 150 GHz pixel streams were fit. The top panel shows the most significant event and the bottom panel shows the second most significant event. The left portion of the top panel shows a time when no observations were taken due to sun contamination.

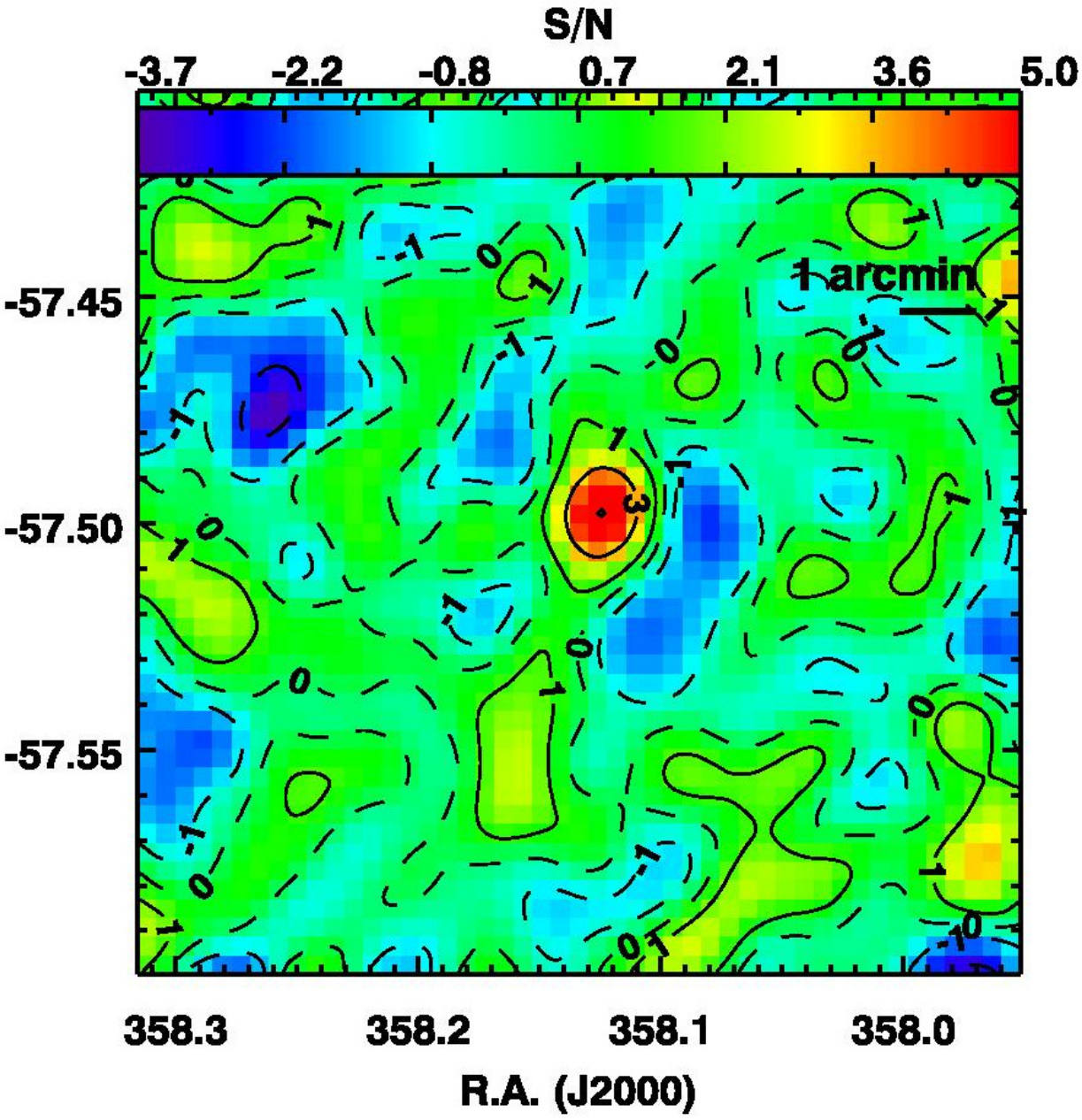

Figure 4.25: A thumbnail image of the 150 GHz SPTpol bundle with the most significant event in units of signal-to-noise. The bundle in the image is near the peak of the Gaussian fit to this event. The Y-axis is in units of declination and the signal-to-noise color scale is across the top of the thumbnail. The flux noise for this bundle is 5.1 mJy and the contours trace out 1, 3, and 5 sigma values. The 5 sigma point near the center of the thumbnail is the most significant transient event in the 150 GHz pixel streams.

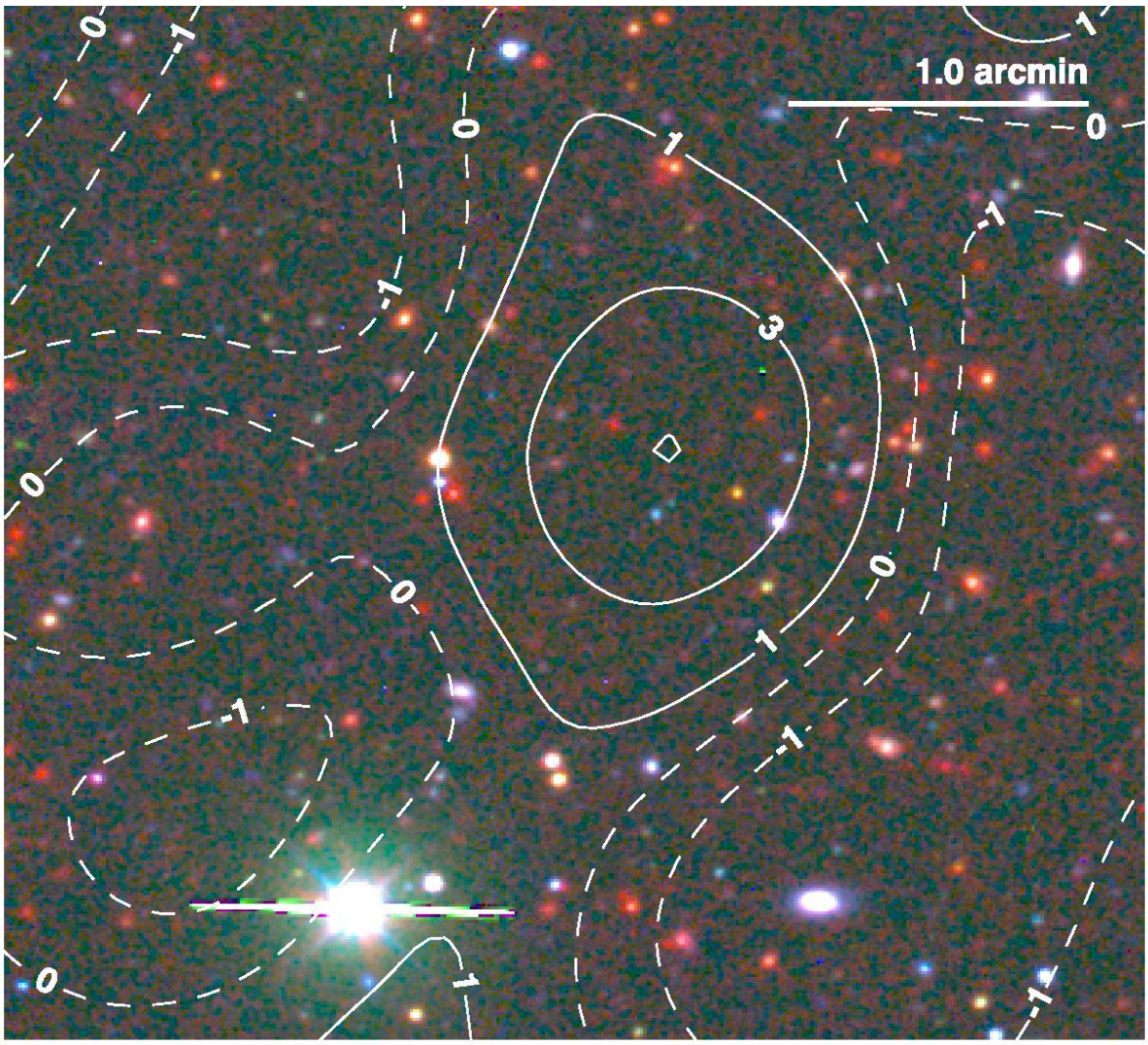

Figure 4.26: A composite infrared (IR) and optical image centered at the location of the most significant transient event. IR data at 3.6 μm are shown in red from the *Spitzer* space telescope and has depth of 7.0 μJy [2]. The *Spitzer* data shown was taken before the transient event observed in the SPTpol data. Blanco Cosmology Survey (BCS) data are shown in green for I band and blue for G band and have a depth of $\sim$0.3 μ [4]. The BCS data was taken on November 11 of 2008, also well before the transient even was observed in the SPTpol data. Contours are 1, 3, and 5 σ levels taken from the SPTpol bundle at the peak of the fit Gaussian (shown in 4.25).

the most significant event the associated 90 GHz pixel stream has no evidence of a positive event, top panel of Figure 4.24. When the 90 GHz is used to constrain the spectrum of the potential transient source a spectral index greater than 1.6 is found at a 90% confidence level. The expected spectral index for a self-absorbed synchrotron source (like a GRB) is between 2 and 2.5 depending on the source.

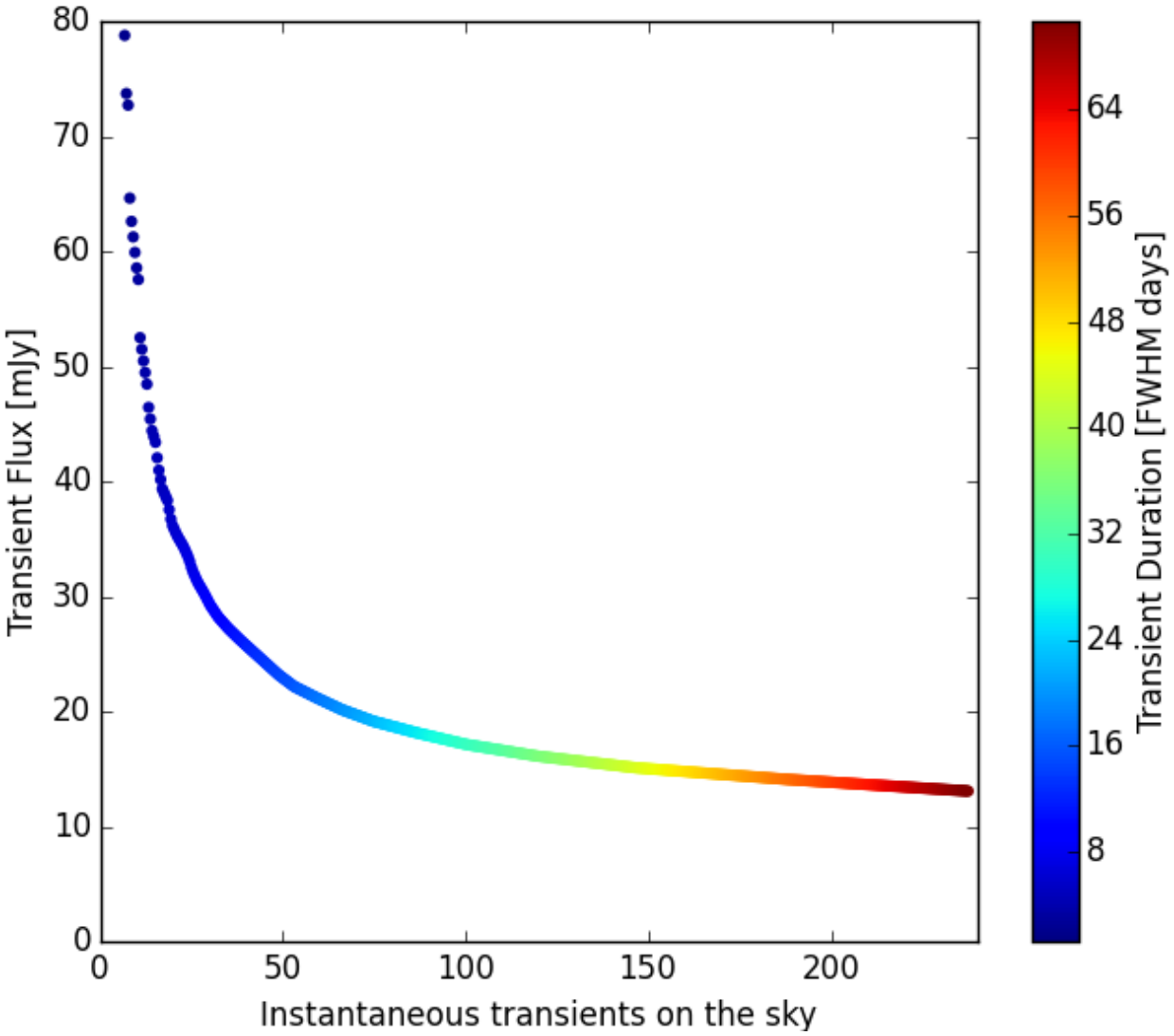

Figure 4.27: The 2 sigma upper limits for instantaneous all-sky number counts of transient sources from the survey conducted in this thesis. The range shown is for transient sources lasting between 2 and 70 days.

CHAPTER 5

CONCLUSION

In this thesis, we have described the SPTpol camera and the detector technology it employs. We have discussed the observation strategy, data reduction, and map making for SPTpol observations of the 100 $\deg^2$ field. We have presented an analysis method for, and the results from, using SPTpol 150 GHz data to produce the first transient search over data taken with the SPT. The transient search was performed over 48.5 $\deg^2$ of sky and included 253 days of live time. Two significant events were found during the transient search. The most significant event has a p-value of 0.080%, a positive amplitude, and is consistent an astrophysical transient event. The second most significant event has a p-vaue of 0.097%, a negative amplitude, and is in slight tension with a noise triggered event.

Using simulations and a realistic noise model an upper limit was placed on number of millimeter transient events on the sky (Figure 4.27). As the sensitivity of millimeter cameras continue to increase, the potential for discovering transients in new frequency bands grows. In early 2016 the next generation camera on the South Pole Telescope, referred to as SPT-3G, will be installed and will include ∼16,000 detectors spread over three frequency bands. This is an order of magnitude more detectors than the SPTpol camera, and the high fidelity coverage in multiple frequency bands could allow instant confirmation of transient sources.

The millimeter transient source limit presented here is an important step in exploring the transient sky in the millimeter band.

CHAPTER 6
REFERENCES

REFERENCES

[1] P. A. R. Ade, G. Pisano, C. Tucker, and S. Weaver. A review of metal mesh filters. In *Society of Photo-Optical Instrumentation Engineers (SPIE) Conference Series*, volume 6275 of *Society of Photo-Optical Instrumentation Engineers (SPIE) Conference Series*, July 2006.

[2] M. L. N. Ashby, S. A. Stanford, M. Brodwin, A. H. Gonzalez, J. Martinez-Manso, J. G. Bartlett, B. A. Benson, L. E. Bleem, T. M. Crawford, A. Dey, A. Dressler, P. R. M. Eisenhardt, A. Galametz, B. T. Jannuzi, D. P. Marrone, S. Mei, A. Muzzin, F. Pacaud, M. Pierre, D. Stern, and J. D. Vieira. The Spitzer South Pole Telescope Deep Field: Survey Design and Infrared Array Camera Catalogs. *ApJS*, 209:22, December 2013.

[3] Edo Berger. Short-Duration Gamma-Ray Bursts. *Annual Review of Astronomy and Astrophysics*, 52(1):43–105, August 2014.

[4] L. E. Bleem, B. Stalder, M. Brodwin, M. T. Busha, M. D. Gladders, F. W. High, A. Rest, and R. H. Wechsler. A New Reduction of the Blanco Cosmology Survey: An Optically Selected Galaxy Cluster Catalog and a Public Release of Optical Data Products. *ApJS*, 216:20, January 2015.

[5] J. Braun, M. Baker, J. Dumm, C. Finley, A. Karle, and T. Montaruli. Time-dependent point source search methods in high energy neutrino astronomy. *Astroparticle Physics*, 33:175–181, April 2010.

[6] R. S. Bussmann, W. L. Holzapfel, and C. L. Kuo. Millimeter Wavelength Brightness Fluctuations of the Atmosphere above the South Pole. *ApJ*, 622:1343–1355, April 2005.

[7] M. R. Calabretta and E. W. Greisen. Representations of celestial coordinates in FITS. *A&A*, 395:1077–1122, December 2002.

[8] J. E. Carlstrom, P. A. R. Ade, K. A. Aird, B. A. Benson, L. E. Bleem, S. Busetti, C. L. Chang, E. Chauvin, H.-M. Cho, T. M. Crawford, A. T. Crites, M. A. Dobbs, N. W. Halverson, S. Heimsath, W. L. Holzapfel, J. D. Hrubes, M. Joy, R. Keisler, T. M. Lanting, A. T. Lee, E. M. Leitch, J. Leong, W. Lu, M. Lueker, D. Luong-van, J. J. McMahon, J. Mehl, S. S. Meyer, J. J. Mohr, T. E. Montroy, S. Padin, T. Plagge, C. Pryke, J. E. Ruhl, K. K. Schaffer, D. Schwan, E. Shirokoff, H. G. Spieler, Z. Staniszewski, A. A. Stark, C. Tucker, K. Vanderlinde, J. D. Vieira, and R. Williamson. The 10 Meter South Pole Telescope. *PASP*, 123:568–581, May 2011.

[9] R. A. Chamberlin. South Pole submillimeter sky opacity and correlations with radiosonde observations. *J. Geophys. Res. Atmospheres*, 106 (D17):20101–20113, 2001.

[10] E. Costa, F. Frontera, J. Heise, M. Feroci, J. in't Zand, F. Fiore, M. N. Cinti, D. Dal Fiume, L. Nicastro, M. Orlandini, E. Palazzi, M. Rapisarda#, G. Zavattini, R. Jager, A. Parmar, A. Owens, S. Molendi, G. Cusumano, M. C. Maccarone, S. Giarrusso, A. Coletta, L. A. Antonelli, P. Giommi, J. M. Muller, L. Piro, and R. C. Butler.

Discovery of an X-ray afterglow associated with the γ-ray burst of 28 February 1997. *Nature*, 387:783–785, June 1997.

[11] A. T. Crites, J. W. Henning, P. A. R. Ade, K. A. Aird, J. E. Austermann, J. A. Beall, A. N. Bender, B. A. Benson, L. E. Bleem, J. E. Carstrom, C. L. Chang, H. C. Chiang, H. Cho, R. Citron, T. M. Crawford, T. De Haan, M. A. Dobbs, W. Everett, J Gallicchio, J. Gao, E. M. George, A. Gilbert, N. W. Halverson, D. Hanson, N. Harrington, G. C. Hilton, G. P. Holder, W. L. Holzapfel, S. Hoover, Z. Hou, J. D. Hrubes, N. Huang, J. Hubmayr, K. D. Irwin, R. Keisler, L. Knox, A. T. Lee, E. M. Leitch, D. Li, C. Liang, D. Luong-Van, J. J. McMahon, J. Mehl, S. S. Meyer, L. Mocanu, T. E. Montroy, T. Natoli, J. P. Nibarger, V. Novosad, S. Padin, C. Pryke, C. L. Reichardt, J. E. Ruhl, B. R. Saliwanchik, J. T. Sayre, K. K. Schaffer, G. Smecher, A. A. Stark, K. T. Story, C. Tucker, K. Vanderlinde, J. D. Vieira, G. Wang, N. Whitehorn, V. Yefremenko, and O. Zahn. Measurements of E-Mode Polarization and Temperature-E-Mode Correlation in the Cosmic Microwave Background from 100 Square Degrees of SPTpol Data. *ArXiv e-prints*, November 2014.

[12] A. de Ugarte Postigo, A. Lundgren, S. Martín, D. Garcia-Appadoo, I. de Gregorio Monsalvo, A. Peck, M. J. Michałowski, C. C. Thöne, S. Campana, J. Gorosabel, N. R. Tanvir, K. Wiersema, A. J. Castro-Tirado, S. Schulze, C. De Breuck, G. Petitpas, J. Hjorth, P. Jakobsson, S. Covino, J. P. U. Fynbo, J. M. Winters, M. Bremer, A. J. Levan, A. Llorente, R. Sánchez-Ramírez, J. C. Tello, and R. Salvaterra. Pre-ALMA observations of GRBs in the mm/submm range. *A&A*, 538:A44, February 2012.

[13] M. A. Dobbs, M. Lueker, K. A. Aird, A. N. Bender, B. A. Benson, L. E. Bleem, J. E. Carlstrom, C. L. Chang, H.-M. Cho, J. Clarke, T. M. Crawford, A. T. Crites, D. I. Flanigan, T. de Haan, E. M. George, N. W. Halverson, W. L. Holzapfel, J. D. Hrubes, B. R. Johnson, J. Joseph, R. Keisler, J. Kennedy, Z. Kermish, T. M. Lanting, A. T. Lee, E. M. Leitch, D. Luong-Van, J. J. McMahon, J. Mehl, S. S. Meyer, T. E. Montroy, S. Padin, T. Plagge, C. Pryke, P. L. Richards, J. E. Ruhl, K. K. Schaffer, D. Schwan, E. Shirokoff, H. G. Spieler, Z. Staniszewski, A. A. Stark, K. Vanderlinde, J. D. Vieira, C. Vu, B. Westbrook, and R. Williamson. Frequency Multiplexed SQUID Readout of Large Bolometer Arrays for Cosmic Microwave Background Measurements. *"Rev. Sci. Instrum.*, 83, July 2012.

[14] A. S. Fruchter, E. Pian, S. E. Thorsett, L. E. Bergeron, R. A. González, M. Metzger, P. Goudfrooij, K. C. Sahu, H. Ferguson, M. Livio, M. Mutchler, L. Petro, F. Frontera, T. Galama, P. Groot, R. Hook, C. Kouveliotou, D. Macchetto, J. van Paradijs, E. Palazzi, H. Pedersen, W. Sparks, and M. Tavani. The Fading Optical Counterpart of GRB 970228, 6 Months and 1 Year Later. *ApJ*, 516:683–692, May 1999.

[15] N. Gehrels, G. Chincarini, P. Giommi, K. O. Mason, J. A. Nousek, A. A. Wells, N. E. White, S. D. Barthelmy, D. N. Burrows, L. R. Cominsky, K. C. Hurley, F. E. Marshall, P. Mszros, P. W. A. Roming, L. Angelini, L. M. Barbier, T. Belloni, S. Campana, P. A. Caraveo, M. M. Chester, O. Citterio, T. L. Cline, M. S. Cropper, J. R. Cummings,

A. J. Dean, E. D. Feigelson, E. E. Fenimore, D. A. Frail, A. S. Fruchter, G. P. Garmire, K. Gendreau, G. Ghisellini, J. Greiner, J. E. Hill, S. D. Hunsberger, H. A. Krimm, S. R. Kulkarni, P. Kumar, F. Lebrun, N. M. Lloyd-Ronning, C. B. Markwardt, B. J. Mattson, R. F. Mushotzky, J. P. Norris, J. Osborne, B. Paczynski, D. M. Palmer, H.-S. Park, A. M. Parsons, J. Paul, M. J. Rees, C. S. Reynolds, J. E. Rhoads, T. P. Sasseen, B. E. Schaefer, A. T. Short, A. P. Smale, I. A. Smith, L. Stella, G. Tagliaferri, T. Takahashi, M. Tashiro, L. K. Townsley, J. Tueller, M. J. L. Turner, M. Vietri, W. Voges, M. J. Ward, R. Willingale, F. M. Zerbi, and W. W. Zhang. The swift gamma-ray burst mission. *The Astrophysical Journal*, 611(2):1005, 2004.

[16] Neil Gehrels and Pter Mszros. Gamma-ray bursts. *Science*, 337(6097):932–936, 2012.

[17] E. M. George, P. Ade, K. A. Aird, J. E. Austermann, J. A. Beall, D. Becker, A. Bender, B. A. Benson, L. E. Bleem, J. Britton, J. E. Carlstrom, C. L. Chang, H. C. Chiang, H.-M. Cho, T. M. Crawford, A. T. Crites, A. Datesman, T. de Haan, M. A. Dobbs, W. Everett, A. Ewall-Wice, N. W. Halverson, N. Harrington, J. W. Henning, G. C. Hilton, W. L. Holzapfel, S. Hoover, N. Huang, J. Hubmayr, K. D. Irwin, M. Karfunkle, R. Keisler, J. Kennedy, A. T. Lee, E. Leitch, D. Li, M. Lueker, D. P. Marrone, J. J. McMahon, J. Mehl, S. S. Meyer, J. Montgomery, T. E. Montroy, J. Nagy, T. Natoli, J. P. Nibarger, M. D. Niemack, V. Novosad, S. Padin, C. Pryke, C. L. Reichardt, J. E. Ruhl, B. R. Saliwanchik, J. T. Sayre, K. K. Schaffer, E. Shirokoff, K. Story, C. Tucker, K. Vanderlinde, J. D. Vieira, G. Wang, R. Williamson, V. Yefremenko, K. W. Yoon, and E. Young. Performance and on-sky optical characterization of the SPTpol instrument. In *Society of Photo-Optical Instrumentation Engineers (SPIE) Conference Series*, volume 8452, September 2012.

[18] E. M. George, J. E. Austermann, J. A. Beall, D. Becker, B. A. Benson, L. E. Bleem, J. E. Carlstrom, C. L. Chang, H.-M. Cho, A. T. Crites, M. A. Dobbs, W. Everett, N. W. Halverson, J. W. Henning, G. C. Hilton, W. L. Holzapfel, J. Hubmayr, K. D. Irwin, D. Li, M. Lueker, J. J. McMahon, J. Mehl, J. Montgomery, T. Natoli, J. P. Nibarger, M. D. Niemack, V. Novosad, J. E. Ruhl, J. T. Sayre, E. Shirokoff, K. T. Story, G. Wang, V. Yefremenko, K. W. Yoon, and E. Young. A Study of Al-Mn Transition Edge Sensor Engineering for Stability. *Journal of Low Temperature Physics*, 176:383–391, August 2014.

[19] G. Ghirlanda, R. Salvaterra, S. Campana, S. D. Vergani, J. Japelj, M. G. Bernardini, D. Burlon, P. D'Avanzo, A. Melandri, A. Gomboc, F. Nappo, R. Paladini, A. Pescalli, O. S. Salafia, and G. Tagliaferri. Unveiling the population of orphan γ-ray bursts. *A&A*, 578:A71, June 2015.

[20] C. Granet, G. L. James, R. Bolton, and G. Moorey. A Smooth-Walled Spline-Profile Horn as an Alternative to the Corrugated Horn for Wide Band Millimeter-Wave Applications. *IEEE Transactions on Antennas and Propagation*, 52:848–854, March 2004.

[21] D. Gruber, A. Goldstein, V. Weller von Ahlefeld, P. Narayana Bhat, E. Bissaldi, M. S. Briggs, D. Byrne, W. H. Cleveland, V. Connaughton, R. Diehl, G. J. Fishman, G. Fitz-

patrick, S. Foley, M. Gibby, M. M. Giles, J. Greiner, S. Guiriec, A. J. van der Horst, A. von Kienlin, C. Kouveliotou, E. Layden, L. Lin, C. A. Meegan, S. McGlynn, W. S. Paciesas, V. Pelassa, R. D. Preece, A. Rau, C. A. Wilson-Hodge, S. Xiong, G. Younes, and H.-F. Yu. The Fermi GBM Gamma-Ray Burst Spectral Catalog: Four Years of Data. *ApJS*, 211:12, March 2014.

[22] M. G. Haehnelt and M. Tegmark. Using the Kinematic Sunyaev-Zeldovich effect to determine the peculiar velocities of clusters of galaxies. *MNRAS*, 279:545+, March 1996.

[23] D. Hanson, S. Hoover, A. Crites, P. A. R. Ade, K. A. Aird, J. E. Austermann, J. A. Beall, A. N. Bender, B. A. Benson, L. E. Bleem, J. J. Bock, J. E. Carlstrom, C. L. Chang, H. C. Chiang, H.-M. Cho, A. Conley, T. M. Crawford, T. de Haan, M. A. Dobbs, W. Everett, J. Gallicchio, J. Gao, E. M. George, N. W. Halverson, N. Harrington, J. W. Henning, G. C. Hilton, G. P. Holder, W. L. Holzapfel, J. D. Hrubes, N. Huang, J. Hubmayr, K. D. Irwin, R. Keisler, L. Knox, A. T. Lee, E. Leitch, D. Li, C. Liang, D. Luong-Van, G. Marsden, J. J. McMahon, J. Mehl, S. S. Meyer, L. Mocanu, T. E. Montroy, T. Natoli, J. P. Nibarger, V. Novosad, S. Padin, C. Pryke, C. L. Reichardt, J. E. Ruhl, B. R. Saliwanchik, J. T. Sayre, K. K. Schaffer, B. Schulz, G. Smecher, A. A. Stark, K. T. Story, C. Tucker, K. Vanderlinde, J. D. Vieira, M. P. Viero, G. Wang, V. Yefremenko, O. Zahn, and M. Zemcov. Detection of B-Mode Polarization in the Cosmic Microwave Background with Data from the South Pole Telescope. *Physical Review Letters*, 111(14):141301, October 2013.

[24] F. A. Harrison, J. S. Bloom, D. A. Frail, R. Sari, S. R. Kulkarni, S. G. Djorgovski, T. Axelrod, J. Mould, B. P. Schmidt, M. H. Wieringa, R. M. Wark, R. Subrahmanyan, D. McConnell, P. J. McCarthy, B. E. Schaefer, R. G. McMahon, R. O. Markze, E. Firth, P. Soffitta, and L. Amati. Optical and radio observations of the afterglow from grb 990510: Evidence for a jet. *The Astrophysical Journal Letters*, 523(2):L121, 1999.

[25] J. W. Henning, P. Ade, K. A. Aird, J. E. Austermann, J. A. Beall, D. Becker, B. A. Benson, L. E. Bleem, J. Britton, J. E. Carlstrom, C. L. Chang, H.-M. Cho, T. M. Crawford, A. T. Crites, A. Datesman, T. de Haan, M. A. Dobbs, W. Everett, A. Ewall-Wice, E. M. George, N. W. Halverson, N. Harrington, G. C. Hilton, W. L. Holzapfel, J. Hubmayr, K. D. Irwin, M. Karfunkle, R. Keisler, J. Kennedy, A. T. Lee, E. Leitch, D. Li, M. Lueker, D. P. Marrone, J. J. McMahon, J. Mehl, S. S. Meyer, J. Montgomery, T. E. Montroy, J. Nagy, T. Natoli, J. P. Nibarger, M. D. Niemack, V. Novosad, S. Padin, C. Pryke, C. L. Reichardt, J. E. Ruhl, B. R. Saliwanchik, J. T. Sayre, K. K. Schaffer, E. Shirokoff, K. Story, C. Tucker, K. Vanderlinde, J. D. Vieira, G. Wang, R. Williamson, V. Yefremenko, K. W. Yoon, and E. Young. Feedhorn-coupled TES polarimeter camera modules at 150 GHz for CMB polarization measurements with SPTpol. In *Society of Photo-Optical Instrumentation Engineers (SPIE) Conference Series*, volume 8452, September 2012.

[26] J. Hjorth and J. S. Bloom. *The Gamma-Ray Burst - Supernova Connection*, pages 169–190. November 2012.

[27] J. Hubmayr, J. W. Appel, J. E. Austermann, J. A. Beall, D. Becker, B. A. Benson, L. E. Bleem, J. E. Carlstrom, C. L. Chang, H. M. Cho, A. T. Crites, T. Essinger-Hileman, A. Fox, E. M. George, N. W. Halverson, N. L. Harrington, J. W. Henning, G. C. Hilton, W. L. Holzapfel, K. D. Irwin, A. T. Lee, D. Li, J. McMahon, J. Mehl, T. Natoli, M. D. Niemack, L. B. Newburgh, J. P. Nibarger, L. P. Parker, B. L. Schmitt, S. T. Staggs, J. van Lanen, E. J. Wollack, and K. W. Yoon. An All Silicon Feedhorn-Coupled Focal Plane for Cosmic Microwave Background Polarimetry. *Journal of Low Temperature Physics*, page 120, December 2011.

[28] R. Keisler, S. Hoover, N. Harrington, J. W. Henning, P. A. R. Ade, K. A. Aird, J. E. Austermann, J. A. Beall, A. N. Bender, B. A. Benson, L. E. Bleem, J. E. Carlstrom, C. L. Chang, H. C. Chiang, H. Cho, R. Citron, T. M. Crawford, A. T. Crites, T. de Haan, M. A. Dobbs, W. Everett, J. Gallicchio, J. Gao, E. M. George, A. Gilbert, N. W. Halverson, D. Hanson, G. C. Hilton, G. P. Holder, W. L. Holzapfel, Z. Hou, J. D. Hrubes, N. Huang, J. Hubmayr, K. D. Irwin, L. Knox, A. T. Lee, E. M. Leitch, D. Li, D. Luong-Van, D. P. Marrone, J. J. McMahon, J. Mehl, S. S. Meyer, L. Mocanu, T. Natoli, J. P. Nibarger, V. Novosad, S. Padin, C. Pryke, C. L. Reichardt, J. E. Ruhl, B. R. Saliwanchik, J. T. Sayre, K. K. Schaffer, E. Shirokoff, G. Smecher, A. A. Stark, K. T. Story, C. Tucker, K. Vanderlinde, J. D. Vieira, G. Wang, N. Whitehorn, V. Yefremenko, and O. Zahn. Measurements of Sub-degree B-mode Polarization in the Cosmic Microwave Background from 100 Square Degrees of SPTpol Data. *ArXiv e-prints*, March 2015.

[29] R. W. Klebesadel, I. B. Strong, and R. A. Olson. Observations of Gamma-Ray Bursts of Cosmic Origin. *ApJ Lett.*, 182:L85, June 1973.

[30] S. Lee, J. M. Gildemeister, W. Holmes, A. T. Lee, and P. L. Richards. Voltage-Biased Superconducting Transition-Edge Bolometer with Strong Electrothermal Feedback Operated at 370 mK. *App Optics*, 37:3391–3397, June 1998.

[31] J. C. Mather. Bolometer noise: nonequilibrium thoery. *App Optics*, 21:1125–1129, March 1982.

[32] Charles Meegan, Giselher Lichti, P. N. Bhat, Elisabetta Bissaldi, Michael S. Briggs, Valerie Connaughton, Roland Diehl, Gerald Fishman, Jochen Greiner, Andrew S. Hoover, Alexander J. van der Horst, Andreas von Kienlin, R. Marc Kippen, Chryssa Kouveliotou, Sheila McBreen, W. S. Paciesas, Robert Preece, Helmut Steinle, Mark S. Wallace, Robert B. Wilson, and Colleen Wilson-Hodge. The fermi gamma-ray burst monitor. *The Astrophysical Journal*, 702(1):791, 2009.

[33] B. D. Metzger, P. K. G. Williams, and E. Berger. Extragalactic Transients in the Era of Wide-Field Radio Surveys. I. Detection Rates and Light Curve Characteristics. *ArXiv e-prints*, February 2015.

[34] National Research Council. *New Worlds, New Horizons in Astronomy and Astrophysics*. The National Academies Press, Washington, DC, 2010.

[35] R. J. Nemiroff, J. P. Norris, C. Kouveliotou, G. J. Fishman, C. A. Meegan, and W. S. Paciesas. Gamma-ray bursts are time-asymmetric. *ApJ*, 423:432–435, March 1994.

[36] S. Padin, Z. Staniszewski, R. Keisler, M. Joy, A. A. Stark, P. A. R. Ade, K. A. Aird, B. A. Benson, L. E. Bleem, J. E. Carlstrom, C. L. Chang, T. M. Crawford, A. T. Crites, M. A. Dobbs, N. W. Halverson, S. Heimsath, R. E. Hills, W. L. Holzapfel, C. Lawrie, A. T. Lee, E. M. Leitch, J. Leong, W. Lu, M. Lueker, J. J. McMahon, S. S. Meyer, J. J. Mohr, T. E. Montroy, T. Plagge, C. Pryke, J. E. Ruhl, K. K. Schaffer, E. Shirokoff, H. G. Spieler, and J. D. Vieira. South pole telescope optics. *Appl. Opt.*, 47(24):4418–4428, 2008.

[37] M. De Pasquale, L. Piro, R. Perna, E. Costa, M. Feroci, G. Gandolfi, J. in t Zand, L. Nicastro, F. Frontera, L. A. Antonelli, F. Fiore, and G. Stratta. A comparative study of the x-ray afterglow properties of optically bright and dark gamma-ray bursts. *The Astrophysical Journal*, 592(2):1018, 2003.

[38] D. A. Perley, T. Krühler, S. Schulze, A. de Ugarte Postigo, J. Hjorth, E. Berger, S. B. Cenko, R. Chary, A. Cucchiara, R. Ellis, W. Fong, J. P. U. Fynbo, J. Gorosabel, J. Greiner, P. Jakobsson, S. Kim, T. Laskar, A. J. Levan, M. J. Michałowski, B. Milvang-Jensen, N. R. Tanvir, C. C. Thöne, and K. Wiersema. The Swift Gamma-Ray Burst Host Galaxy Legacy Survey - I. Sample Selection and Redshift Distribution. *ArXiv e-prints*, April 2015.

[39] T. Piran. The physics of gamma-ray bursts. *Reviews of Modern Physics*, 76:1143–1210, October 2004.

[40] C. Pryke, P. Ade, J. Bock, M. Bowden, M. L. Brown, G. Cahill, P. G. Castro, S. Church, T. Culverhouse, R. Friedman, K. Ganga, W. K. Gear, S. Gupta, J. Hinderks, J. Kovac, A. E. Lange, E. Leitch, S. J. Melhuish, Y. Memari, J. A. Murphy, A. Orlando, R. Schwarz, C. O'Sullivan, L. Piccirillo, N. Rajguru, B. Rusholme, A. N. Taylor, K. L. Thompson, A. H. Turner, E. Y. S. Wu, and M. Zemcov. Second and Third Season QUaD Cosmic Microwave Background Temperature and Polarization Power Spectra. *ApJ*, 692:1247–1270, February 2009.

[41] Daniel E. Reichart and Paul A. Price. Evidence for a molecular cloud origin of gamma-ray bursts: Implications for the nature of star formation in the universe. *The Astrophysical Journal*, 565(1):174, 2002.

[42] M. C. Runyan, P. A. R. Ade, R. S. Bhatia, J. J. Bock, M. D. Daub, J. H. Goldstein, C. V. Haynes, W. L. Holzapfel, C. L. Kuo, A. E. Lange, J. Leong, M. Lueker, M. Newcomb, J. B. Peterson, C. Reichardt, J. Ruhl, G. Sirbi, E. Torbet, C. Tucker, A. D. Turner, and D. Woolsey. ACBAR: The Arcminute Cosmology Bolometer Array Receiver. *ApJS*, 149:265–287, December 2003.

[43] J. T. Sayre, P. Ade, K. A. Aird, J. E. Austermann, J. A. Beall, D. Becker, B. A. Benson, L. E. Bleem, J. Britton, J. E. Carlstrom, C. L. Chang, H.-M. Cho, T. M. Crawford,

A. T. Crites, A. Datesman, T. de Haan, M. A. Dobbs, W. Everett, A. Ewall-Wice, E. M. George, N. W. Halverson, N. Harrington, J. W. Henning, G. C. Hilton, W. L. Holzapfel, J. Hubmayr, K. D. Irwin, M. Karfunkle, R. Keisler, J. Kennedy, A. T. Lee, E. Leitch, D. Li, M. Lueker, D. P. Marrone, J. J. McMahon, J. Mehl, S. S. Meyer, J. Montgomery, T. E. Montroy, J. Nagy, T. Natoli, J. P. Nibarger, M. D. Niemack, V. Novosad, S. Padin, C. Pryke, C. L. Reichardt, J. E. Ruhl, B. R. Saliwanchik, K. K. Schaffer, E. Shirokoff, K. Story, C. Tucker, K. Vanderlinde, J. D. Vieira, G. Wang, R. Williamson, V. Yefremenko, K. W. Yoon, and E. Young. Design and characterization of 90 GHz feedhorn-coupled TES polarimeter pixels in the SPTPol camera. In *Society of Photo-Optical Instrumentation Engineers (SPIE) Conference Series*, volume 8452, September 2012.

[44] K. K. Schaffer, T. M. Crawford, K. A. Aird, B. A. Benson, L. E. Bleem, J. E. Carlstrom, C. L. Chang, H. M. Cho, A. T. Crites, T. de Haan, M. A. Dobbs, E. M. George, N. W. Halverson, G. P. Holder, W. L. Holzapfel, S. Hoover, J. D. Hrubes, M. Joy, R. Keisler, L. Knox, A. T. Lee, E. M. Leitch, M. Lueker, D. Luong-Van, J. J. McMahon, J. Mehl, S. S. Meyer, J. J. Mohr, T. E. Montroy, S. Padin, T. Plagge, C. Pryke, C. L. Reichardt, J. E. Ruhl, E. Shirokoff, H. G. Spieler, B. Stalder, Z. Staniszewski, A. A. Stark, K. Story, K. Vanderlinde, J. D. Vieira, and R. Williamson. The First Public Release of South Pole Telescope Data: Maps of a 95 deg^2 Field from 2008 Observations. *ApJ*, 743:90, December 2011.

[45] K. Sheth, D. A. Frail, S. White, M. Das, F. Bertoldi, F. Walter, S. R. Kulkarni, and E. Berger. Millimeter Observations of GRB 030329: Continued Evidence for a Two-Component Jet. *ApJ Lett.*, 595:L33–L36, September 2003.

[46] Z. Staniszewski, P. A. R. Ade, K. A. Aird, B. A. Benson, L. E. Bleem, J. E. Carlstrom, C. L. Chang, H.-M. Cho, T. M. Crawford, A. T. Crites, T. de Haan, M. A. Dobbs, N. W. Halverson, G. P. Holder, W. L. Holzapfel, J. D. Hrubes, M. Joy, R. Keisler, T. M. Lanting, A. T. Lee, E. M. Leitch, A. Loehr, M. Lueker, J. J. McMahon, J. Mehl, S. S. Meyer, J. J. Mohr, T. E. Montroy, C.-C. Ngeow, S. Padin, T. Plagge, C. Pryke, C. L. Reichardt, J. E. Ruhl, K. K. Schaffer, L. Shaw, E. Shirokoff, H. G. Spieler, B. Stalder, A. A. Stark, K. Vanderlinde, J. D. Vieira, O. Zahn, and A. Zenteno. Galaxy Clusters Discovered with a Sunyaev-Zel'dovich Effect Survey. *ApJ*, 701:32–41, August 2009.

[47] N. R. Tanvir, D. B. Fox, A. J. Levan, E. Berger, K. Wiersema, J. P. U. Fynbo, A. Cucchiara, T. Krühler, N. Gehrels, J. S. Bloom, J. Greiner, P. A. Evans, E. Rol, F. Olivares, J. Hjorth, P. Jakobsson, J. Farihi, R. Willingale, R. L. C. Starling, S. B. Cenko, D. Perley, J. R. Maund, J. Duke, R. A. M. J. Wijers, A. J. Adamson, A. Allan, M. N. Bremer, D. N. Burrows, A. J. Castro-Tirado, B. Cavanagh, A. de Ugarte Postigo, M. A. Dopita, T. A. Fatkhullin, A. S. Fruchter, R. J. Foley, J. Gorosabel, J. Kennea, T. Kerr, S. Klose, H. A. Krimm, V. N. Komarova, S. R. Kulkarni, A. S. Moskvitin, C. G. Mundell, T. Naylor, K. Page, B. E. Penprase, M. Perri, P. Podsiadlowski, K. Roth, R. E. Rutledge, T. Sakamoto, P. Schady, B. P. Schmidt, A. M. Soderberg, J. Sollerman, A. W.

Stephens, G. Stratta, T. N. Ukwatta, D. Watson, E. Westra, T. Wold, and C. Wolf. A γ-ray burst at a redshift of z˜8.2. *Nature*, 461:1254–1257, October 2009.

[48] Y. Urata, K. Huang, K. Asada, H. Hirashita, M. Inoue, and P. T. P. Ho. A new era of sub-millimeter GRB afterglow follow-ups with the Greenland Telescope. *ArXiv e-prints*, March 2015.

[49] H. Weinstock. *SQUID Sensors: Fundamentals, Fabrication and Applications*. Nato Science Series E:. Springer Netherlands, 2012.

[50] Lingzhen Zeng, Charles L. Bennett, David T. Chuss, and Edward J. Wollack. A wide-band smooth-walled feedhorn with low cross polarization for millimeter astronomy, 2010.